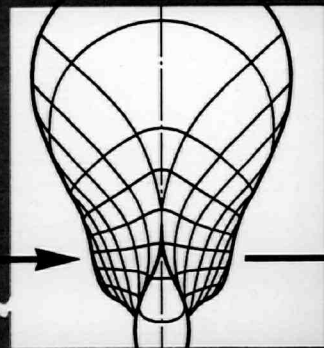


Technische Universität
Hamburg-Harburg
Arbeitsbereiche Schiffbau



Delft University of Technology
Ship Hydromechanics Laboratory
Library
Mekelweg 2, 2628 CD Delft
The Netherlands
Phone: +31 15 2786873 - Fax: +31 15 2781836

Numerical Simulations of the Primary Breakup of Liquid Jets

Frank-Olivier Albina

April 2005

Numerical Simulations of the Primary Breakup of Liquid Jets

Vom Promotionsausschuss
der TU Hamburg-Harburg
zur Erlangung des akademischen Grades
Doktor-Ingenieur
genehmigte Dissertation

von

Frank-Olivier Albina
aus Besançon (Frankreich)

2005

Numerical Simulations of the Primary Breakup of Liquid Jets

Frank-Olivier Albina, 1. Auflage, Hamburg: Arbeitsbereiche Schiffbau, 2005
ISBN 3-89220-631-7

Gutachter:

Prof. Dr.-Ing. E. von Lavante
Prof. Dr.-Ing. G. Jensen
Prof. Dr.-Ing. M. Perić

Tag der mündlichen Prüfung: 19.01.2005

©Arbeitsbereiche Schiffbau
Technische Universität Hamburg-Harburg
Lämmersieth 90
D-22305 Hamburg
Germany

Acknowledgements

In the first place, I would like to thank my family, friends and former colleagues from the University for their continuous support during the many years it took me to write down this thesis work. Without their encouragements, I would probably never have come to the point of writing down these few lines.

Also, I would like to thank my PhD advisor, Prof. Perić for his help and for the numerous corrections hours he spent on the first versions of this thesis. I am also very grateful to him for all the suggestions he made for improving the quality of the work summarized hereafter.

Many thanks are dedicated to Prof. Obermeier, Dr. Chaves and their coworkers from the IMFD (Institut für Mechanik und Fluidodynamik – Technische Universität Bergakademie Freiberg) who provided the nozzle geometries as well as the stroboscopic photographs used in this work. Special thanks go to Dr. Chaves for the numerous fruitful discussions we spent on the subject of the simulations related to the forced breakup of liquid jets.

I am also grateful to the help concerning the use of LMS-Sysnoise software provided by the coworkers of the Arbeitsbereich Meerestechnik II at the Technical University of Hamburg-Harburg under the lead of Prof. von Estorff without which it would have been very difficult to obtain the acoustical resonant modes presented in this work.

My sincere thanks go to Prof. von Lavante (University of Essen, Germany) and Prof. Walzel (University of Dortmund, Germany) for sharing with me their understanding of the flow physics related to spray breakup.

Finally, I am also indebted to the German Research Foundation (DFG) for sponsoring the work presented herein. And because, everything which comes to an end has also a beginning, many thanks go to the German Office of Foreign Exchange (DAAD) without which I would have never had the chance to start this PhD thesis.

Contents

Contents	i
List of Figures	iii
List of Tables	xi
Nomenclature	xiii
1 Introduction	1
1.1 Motivation	1
1.2 Previous and related work	2
1.3 Author's contribution	3
1.4 Outline of the thesis	4
2 Numerical Method	7
2.1 Outline of the Navier-Stokes solver	7
2.2 About the modeling of free-surface flows	9
2.2.1 Interface-tracking methods	9
2.2.2 Interface-capturing methods	9
2.3 About the free-surface method used	10
2.3.1 Boundedness of the void fraction	11
2.3.2 Setting up initial positions of the free-surface	13
2.4 Surface tension modeling	21
2.4.1 The diffuse interface theory	21
2.4.2 The Continuum Surface Force (CSF) approach	22
2.4.3 Parasitic currents	23
2.4.4 Limitations of the CSF model	28
2.5 Outlet boundary conditions	28
2.5.1 Standard boundary conditions	28
2.5.2 Convective boundary conditions	29
3 Simulations of the Primary Breakup of Laminar Jets	43
3.1 Rayleigh breakup	43
3.2 Medium-ranged actuation frequencies	47
3.3 High-frequency excitation	52
3.3.1 Methodology	52
3.3.2 Nozzle-flow simulations	53
3.3.3 Jet-breakup simulations	64

3.3.4	Comparison of the simulation results with experimental data	71
3.3.5	Discussion	82
3.3.6	Influence of liquid compressibility	86
3.4	Air-flow sustained breakup of a capillary jet	97
3.4.1	Simulation approach	97
3.4.2	Analysis of the air flow	98
3.4.3	Analysis of the jet breakup	100
4	Concluding remarks and further work	107
4.1	Concluding remarks	107
4.1.1	Discussion about numerical aspects	107
4.1.2	Discussion of the simulation results	108
4.2	Further work	109
	Bibliography	111
	Appendix A:	
	An equivalent formulation of the minimization problem	119

List of Figures

2.1	Example of a control volume with outwards oriented normals \mathbf{n} .	8
2.2	Normalized variable diagram (NVD) with various discretization schemes: upwind (UPWIND), downwind (DOWNWIND), linear upwind (LUD), central differences (CDS), quick (QUICK) [55], high-resolution interface-capturing (HRIC) [77]. The shaded area represents the zone where the values of $\tilde{\phi}_f$ are bounded.	12
2.3	Definition of the correction angle θ .	12
2.4	Example of a triangular face with its vertices numbered from P_1 to P_3 in counterclockwise order.	15
2.5	Example of a polygon. G denotes the centroid of the polygon.	15
2.6	Example of a truncated polygon. The area under the free surface (in gray) is the truncated area. The free surface cuts the polygon along a line passing through the points P_{34} and P_{45} . G' denotes the centroid of the truncated area.	17
2.7	Example of an edge cut by the free surface and passing through point F . Vertex U is under the free surface, vertex O is above the free surface.	17
2.8	Example of a truncated cell with eight nodes numbered from 1 to 8. Numeration corresponds to the right-hand rule used in <i>comet</i> . The volume represented in gray is the volume under the free surface plane, i.e. the truncated volume.	19
2.9	Application example of the initialization procedure for a rotated sine wave on a cartesian grid. The obtained free surface is the shaded area.	20
2.10	Boat with a keel at a roll angle of 30 degrees. Thick line: water plane position; thin lines: numerical grid; in color: volume fraction distribution. Application example used in [11].	20
2.11	Residual velocity intensity due to the surface-tension forcing at equilibrium (right). The difference between the calculated value of μ^0 and $\sigma\kappa$ is used for the contour level. The position of the free-surface is given by the depicted void-fraction distribution on the cylindrical grid (left). The velocity field shown results from the standard model (as implemented in <i>comet</i>).	27
2.12	Notations used for defining locations in a control volume next to the outlet boundary, on which point B is lying.	30
2.13	Geometry of benchmark cases 2D-2 and 2D-3 with boundary conditions.	37
2.14	Contours of the velocity component u 7.9 s after the start of the simulation for the case 2D-3. At the outlet on the right-hand side of the computational domain, zones of negative velocity are observed and indicate the presence of back flow at the boundary.	37

- 2.15 Superimposition of the time-averaged pressure levels for the case 2D-2 obtained with a convective boundary condition at the outlet for the shortened and full size computational domains. Full lines represent the reference solution obtained on the complete computational domain; dashed lines represent the pressure levels obtained with the implemented convective boundary condition on the shortened computational domain marked by the vertical line on the right-hand side of the figure. Note that appreciable differences are only present near boundary of the shortened domain – around the cylinder the solutions are almost coincident. . . . 38
- 2.16 Superimposition of the time-averaged pressure levels for the case 2D-2 obtained with the standard boundary condition at the outlet for the shortened and full size computational domains. Full lines represent the reference solution obtained on the complete computational domain; dashed lines represent the pressure levels obtained with the standard outlet boundary condition on the shortened computational domain marked by the vertical line on the right-hand side of the figure. Note that appreciable differences are present even in the front of the cylinder and all around it. 38
- 2.17 Pressure levels for the case 2D-2 on the shortened domain 8 s after the start of the simulation with convective outlet boundary condition. 39
- 2.18 Pressure levels for the case 2D-2 on the reference domain 8 s after the start of the simulation. 39
- 2.19 Pressure levels for the case 2D-2 on the shortened domain 8 s after the start of the simulation with standard outlet boundary condition. 39
- 2.20 Geometry and boundary conditions used for the simulation of the flow around a square cylinder. 40
- 2.21 Superimposition of the time-averaged pressure levels for the flow around a square cylinder with the Neumann boundary condition on pressure. Full lines represent the reference solution obtained on the complete computational domain; dashed lines represent the pressure levels obtained with the outlet boundary condition of Neumann type on the shortened computational domain marked by the vertical line on the right side of the figure. 40
- 2.22 Superimposition of the time-averaged pressure levels for the flow around a square cylinder with a convective boundary condition on pressure. Full lines represent the reference solution obtained on the complete computational domain; dashed lines represent the pressure levels obtained with the convective boundary condition on the shortened computational domain marked by the vertical line on the right side of the figure 41
- 2.23 Time-averaged values of the pressure versus the position along the centerline of the computational domain. The continuous line represents the reference solution obtained on the complete computational domain, while symbols represent the solutions obtained on the truncated computational domain for the Neumann (NBC) and convective (CBC) boundary conditions on pressure. 41
- 3.1 Computed free-surface deformation for the Rayleigh breakup mode for various values of the normalized wave number k^* ; from top to bottom: $k^*=0.250, 0.430, 0.533, 0.683$. Flow is from left to right. 46

3.2	Free-surface deformations as observed in the experiments for the normalized wave numbers $k^*=0.250$ (top) and $k^*=0.683$. The experimental photographs have been taken from [24].	46
3.3	Drop sizes in Rayleigh break-up: comparison between calculated values and experimental data; k^* is the normalized wave number, $D^* = D_{\text{drop}}/D_{\text{jet}}$ is the normalized droplet radius.	46
3.4	Dilational and sinuous modes as they occur during the breakup of a thin liquid sheet.	47
3.5	Geometry and boundary conditions used for the simulation of a sheet breakup with dilational mode forcing.	48
3.6	Comparison of the sheet free-surface deformations for the dilational mode. The dashed line represents the analytical solution from the linear wave theory; the continuous line represents the free-surface deformation obtained in the present simulation. The Weber number in this simulation was $We = 900$	49
3.7	Geometry and boundary conditions used for the simulation of a sheet breakup with sinuous mode forcing.	50
3.8	Comparison of the sheet free-surface deformation for the sinuous mode. The dashed line represents the analytical solution from the linear wave theory; the continuous line represents the free-surface deformation obtained in the simulation. The Weber number used for the simulation was $We = 1800$	51
3.9	Nozzle geometry and boundary conditions used for the numerical simulations of forced break-up of round laminar jets.	53
3.10	Geometrical dimensions of the computational domain. Dimensions are given in millimeters.	53
3.11	Coarsest numerical mesh used for the calculation of the nozzle inner flow with 17,579 control volumes.	54
3.12	Working line of the nozzle	55
3.13	Outlet velocity profiles for different grid resolutions at an inlet pressure of 500,000 Pa.	57
3.14	Profiles of axial (left) and radial (right) velocity profiles at the nozzle outlet for different inlet pressures. Results have been obtained on the coarse grid.	57
3.15	Normalized profiles of axial (left) and radial (right) velocity profiles at the nozzle outlet for different inlet pressures. Results have been obtained on the coarse grid. Normalization is performed with the maximum value of the velocity component.	57
3.16	Axial velocity profiles at nozzle outlet vs. time over one period. $\Delta Z = 175$ nm, $f_0=126$ kHz.	59
3.17	Radial velocity profiles at nozzle outlet vs. time over one period. $\Delta Z = 175$ nm, $f_0=126$ kHz.	59
3.18	Geometry (top) and numerical mesh (bottom) used for the 3D nozzle simulation. The same mesh density is used as in the two-dimensional case, Fig. 3.11. Periodic boundary conditions are depicted in gray and red on the figure.	61
3.19	Working line of the three-dimensional nozzle	62
3.20	Mean velocity at the nozzle exit over time. Time is made dimensionless by using the excitation period. Periodicity is achieved within a few excitation periods. $\Delta Z = 100$ nm.	62

- 3.21 Axial velocity profiles at nozzle outlet vs. time over one period. The velocity profile is obtained at one cross section of the nozzle outlet. $\Delta Z = 100$ nm, $f_0 = 126$ kHz. 63
- 3.22 Radial velocity profiles vs. time over one period of actuation. The velocity profile is obtained at one cross section of the nozzle outlet. $\Delta Z = 100$ nm, $f_0 = 126$ kHz. 63
- 3.23 Typical velocity profiles in radial and axial directions obtained at the nozzle outlet. 65
- 3.24 Layout of the computational domain with the boundary conditions employed. . 65
- 3.25 Detail of a numerical grid with 16,960 CVs used for the two-dimensional simulations of jet breakup. 66
- 3.26 Detail of the mesh used for the three-dimensional jet-breakup simulations. Cyclic boundary conditions are used on the regions colored in red and green on the figure. 66
- 3.27 Cuts along the jet axis obtained for various disturbance amplitudes at nearly constant Strouhal number and for distinct inlet boundary conditions: an inlet profile obtained from the unsteady nozzle-flow simulation (left), a block profile modulated by a sine wave (right). Fluid flow is from the right to the left. Numerical grids have the same refinement level for capturing the free-surface position. 72
- 3.28 Stroboscopic photographs of the free-surface deformations of a jet of ethanoic alcohol under forced, periodical excitation at a frequency of 126 kHz (courtesy of IMFD, TU Bergakademie Freiberg, Germany). The excitation level increases from left to right and from left to bottom and is given by the RMS value of the input voltage. u indicates the mean nozzle outflow velocity and the jet issues from the nozzle at the top of each photograph. 73
- 3.29 Jet free-surface deformation with pressure contours at different instants over an excitation period. Inlet velocity is obtained by the modulation of a block-profile. Excitation amplitude is $\epsilon_0 = 16\%$. Flow is from left to right. 74
- 3.30 Time averaged velocity profile for both gas and liquid flow in the case of the modulated block profile of eq. (3.23). $\langle U_r \rangle$, $\langle U_\theta \rangle$ and $\langle U_z \rangle$ denote respectively the velocity components in radial, azimuthal and axial (streamwise) directions. The black line represents the instantaneous free-surface position in the midplane of the computational domain. Flow is from left to right. 75
- 3.31 Time averaged profiles of the velocity fluctuations for both gas and liquid flow in the case of the modulated block profile of eq. (3.23). $\langle u'_r \rangle$, $\langle u'_\theta \rangle$ and $\langle u'_z \rangle$ denote respectively the root mean square (rms) values of the velocity components in radial, azimuthal and axial (streamwise) directions. The black line represents the instantaneous free-surface position in the midplane of the computational domain. Flow is from left to right. 75
- 3.32 Jet free-surface deformation with pressure contours at different instants over an excitation period. Inlet velocity is obtained by the simulation of the nozzle internal flow. Flow is from left to right. 76
- 3.33 Time averaged velocity profile for both gas and liquid flow with inflow conditions gained from the nozzle simulation. $\langle U_r \rangle$, $\langle U_\theta \rangle$ and $\langle U_z \rangle$ denote respectively the velocity components in radial, azimuthal and axial (streamwise) directions. The black line represents the instantaneous free-surface position in the midplane of the computational domain. Flow is from left to right. 77

- 3.34 Time averaged profiles of the velocity fluctuations for both gas and liquid flow with inflow conditions gained from the nozzle simulation. $\langle u'r \rangle$, $\langle u'\theta \rangle$ and $\langle u'z \rangle$ denote respectively the root mean square (rms) values of the velocity components in radial, azimuthal and axial (streamwise) directions. The black line represents the instantaneous free-surface position in the midplane of the computational domain. Flow is from left to right. 77
- 3.35 Jet free-surface deformation with pressure contours at different instants over an excitation period. Inlet velocity is obtained by a modulated block-profile with disturbances in azimuthal direction. Flow is from left to right. 78
- 3.36 Time averaged velocity profile for both gas and liquid flow in the case the modulated block-profile with disturbances in azimuthal direction. $\langle U_r \rangle$, $\langle U_\theta \rangle$ and $\langle U_z \rangle$ denote respectively the velocity components in radial, azimuthal and axial (streamwise) directions. The black line represents the instantaneous free-surface position in the midplane of the computational domain. Flow is from left to right. 79
- 3.37 Time averaged profiles of the velocity fluctuations for both gas and liquid flow in the case the modulated block-profile with disturbances in azimuthal direction. $\langle u'r \rangle$, $\langle u'\theta \rangle$ and $\langle u'z \rangle$ denote respectively the root mean square (rms) values of the velocity components in radial, azimuthal and axial (streamwise) directions. The black line represents the instantaneous free-surface position in the midplane of the computational domain. Flow is from left to right. 79
- 3.38 Jet free-surface deformation with pressure contours at different instants over an excitation period. Inlet velocity is obtained by the velocity profiles gained from the nozzle flow simulations with superposed disturbances in azimuthal direction. Flow is from left to right. 80
- 3.39 Time averaged velocity profile for both gas and liquid flow in the case of the nozzle flow with superimposed disturbances in azimuthal direction. $\langle U_r \rangle$, $\langle U_\theta \rangle$ and $\langle U_z \rangle$ denote respectively the velocity components in radial, azimuthal and axial (streamwise) directions. The black line represents the instantaneous free-surface position in the midplane of the computational domain. Flow is from left to right. 81
- 3.40 Time averaged profiles of the velocity fluctuations for both gas and liquid flow in the case of the nozzle flow with superimposed disturbances in azimuthal direction. $\langle u'r \rangle$, $\langle u'\theta \rangle$ and $\langle u'z \rangle$ denote respectively root mean square (rms) values of the velocity components in radial, azimuthal and axial (streamwise) direction. The black line represents the instantaneous free-surface position in the midplane of the computational domain. Flow is from left to right. 81
- 3.41 Comparison of the shape of the free-surface obtained with the two-dimensional simulation (contoured shape) and the one obtained with the three-dimensional simulation (black line). Both results use the simple actuation model from eq. (3.23). 83
- 3.42 Comparison of the shape of the free-surface obtained with the two-dimensional simulation (contoured shape) and the one obtained with the three-dimensional (black line) simulation. Both results use the velocity profile gained from the resp. two-dimensional and three-dimensional nozzle simulation. 83

3.43	Comparison of the shape of the free-surface obtained with the two-dimensional simulation (contoured shape) and the one obtained with the three-dimensional simulation (black line). The two-dimensional simulation uses the simple actuation model of eq. (3.23), the three-dimensional one uses the actuation with additional disturbances of eqs. (3.24) and (3.25).	83
3.44	Comparison of the shape of the free-surface obtained with the two-dimensional simulation (contoured shape) and the one obtained with the three-dimensional simulation (black line). The two-dimensional simulation uses the velocity profiles gained from the two-dimensional nozzle flow simulation, whereas the three-dimensional simulation uses the velocity profiles of the 3D nozzle simulation with additional disturbances of eqs. (3.24) and (3.25).	84
3.45	Time-averaged values of the gas pressure fluctuations $\langle p' \rangle$ for the four different types of jet actuations investigated. From top to bottom: simple actuation model from eq. (3.23), actuation with the velocity profile gained from the nozzle simulation, simple actuation model with additional azimuthal disturbances of eqs. (3.24) and (3.25), actuation with the nozzle velocity profiles and superimposed azimuthal disturbances of eqs. (3.24) and (3.25). The black line shows the instantaneous position of the jet free surface for the corresponding actuation level.	85
3.46	Estimated resonance mode for the investigated nozzle geometry. The dashed lines denote the modal lines of zero amplitude, the + signs the locations of crests and the - signs the locations of troughs.	89
3.47	Superposition of numerical mesh used for the analysis and resonance mode at the frequency $f=127.368$ kHz.	89
3.48	Resonance mode at frequency $f=126.670$ kHz: Superposition of numerical mesh used for the analysis and modal pressure (top), cut through the nozzle midplane showing the distribution of the modal pressures (bottom).	90
3.49	Numerical grid used for the compressible simulation of the nozzle internal flow. Only the half of the entire model is used and for recovering the complete model, a pair of periodic boundary conditions is used, depicted in blue and magenta on the figure.	91
3.50	Location of the probes within the computational domain, used for registering the time signals of pressure and velocity.	91
3.51	Fourier transform in frequency space of the pressure time signal registered at four different locations within the computational domain. The probe locations are given by Fig. 3.50	94
3.52	Fourier transform in frequency space of the time signal of the azimuthal velocity registered at four different locations within the computational domain. The probe locations are given by Fig. 3.50	94
3.53	Density variation within the nozzle at a frequency of 126,670 kHz obtained for a section passing through the nozzle midplane (top) and on the nozzle external surface (bottom).	95
3.54	Spatial variations of the azimuthal velocity within the computational domain at a frequency of 127,368 Hz.	96

3.55	Pneumatic extension nozzle flow: schematic principle. Due to the pressure difference across the orifice plate, an air flow develops and strains the capillary jet that breaks up into droplets due to the Rayleigh instability. The orifice plate is placed at a distance H from the nozzle exit. In the present analysis: $H=D$.	97
3.56	Computational domain used for the calculations. The distance between the nozzle outlet and the orifice plate corresponds to one nozzle diameter. The inflow velocity profile is the parabolic one of the Couette-Poiseuille laminar pipe flow.	99
3.57	Detail of a numerical grid used for the simulations using the advantage of local refinement for resolving accurately the free-surface deformations as well as the detachment of vortices at the orifice edge.	99
3.58	Instantaneous pressure distribution in the computational domain. Low pressure regions are marked in blue and indicate the presence of vortices ($\Delta p = 90\text{Pa}$). The pressure jump extending downward the nozzle exit (bottom left) corresponds to the actual position of the free-surface and is mainly due to surface tension effects. Flow is from left to right.	101
3.59	Instantaneous pressure distribution and free-surface deformation of the capillary jet (in red) within the computational domain on the coarse grid. Low pressure regions are marked in blue and indicate the presence of vortices. The vortices interact with the jet free-surface and detaching vortices because of the air flow over a droplet is observed as well (to be seen on the first droplet of the figure). Flow is from left to right.	101
3.60	Instantaneous velocity distribution and free-surface deformation of the capillary jet (in red) within the computational domain on the coarse grid. The air flow is accelerated towards the orifice edge and an unsteady airflow develops downstream of it. Eventually vortices are created which interact with the jet free-surface (in red). Flow is from left to right.	102
3.61	Free-surface shape obtained in the experiments of Schmelz <i>et al.</i> , reproduced from [92]. Although there are no indications about the distance between nozzle exit and orifice, it can be deduced from the experimental photographs that the ratio is $H/D \approx 0.5$.	102
3.62	Amplitudes of the Fourier modes of the recorded time signals vs. the Strouhal number. The measured frequencies correspond to the situation of Fig. 3.58, for which the vortices detaching from the orifice edge do not interact with the jet free-surface ("no-breakup condition"); the jet has not formed yet and the liquid starts to drop from the capillary nozzle. The frequency spectrum registered is then solely due to vortices detaching from the orifice edge.	103
3.63	Amplitudes of the Fourier modes of the recorded time signals vs. the Strouhal number. The measured frequencies correspond to the situation of Fig. 3.59, for which the vortices detaching from the orifice edge interact with the jet free-surface (jet breakup conditions).	103
3.64	Evolution in time of the free-surface of the capillary jet submitted to an external disturbance arising from the vortex shedding of the surrounding air flow. Continuation on figure 3.65.	105
3.65	Continuation of figure 3.64	106

List of Tables

2.1	Comparison of the Strouhal numbers obtained on various computational domains for case <i>2D-2</i> using two types of boundary conditions for velocities: convective and standard outlet. The end of the short domain is placed 6 diameter length behind the cylinder center.	35
2.2	Comparison of the Strouhal numbers obtained on various computational domains for the flow around a square cylinder using two types of boundary conditions for pressure: convective and of Neumann type. The end of the short domain is placed 10 square-edge length behind the cylinder center.	37
3.1	Physical properties used for the simulations of the Rayleigh breakup.	44
3.2	Liquid physical properties and reference dimensions used for the simulation of the sheet breakup with dilational mode forcing.	49
3.3	Liquid physical properties and reference dimensions used for the simulation of the sheet breakup with sinuous mode forcing.	51
3.4	High-frequency excitation: Physical properties of the fluids used for the simulations	53
3.5	Mechanisms of onset of jet breakup, [63]	84
3.6	Physical properties of ethanol to be used for compressibility analysis.	87
3.7	Air-flow assisted breakup: Physical properties of the fluids used for the simulations.	98

Nomenclature

Mathematical symbols

$\frac{d}{dt}$	Total time derivative	
$\frac{\partial}{\partial t}$	Time derivative	
$\frac{\partial}{\partial n}$	Normal derivative to a surface	$\frac{\partial}{\partial n} = \langle \nabla, \mathbf{n} \rangle$
$\phi_{,k}$	Derivative of variable ϕ wrt. the direction x_k	
ϕ	Vector variable	$\phi = (\phi_1; \phi_2; \phi_3)$
∇	Gradient operator	$\nabla = \left(\frac{\partial}{\partial x}; \frac{\partial}{\partial y}; \frac{\partial}{\partial z} \right)$
\mathbf{u}	Velocity field	$\mathbf{u} = (u; v; w)$
$\overline{\overline{\mathbf{M}}}$	Second-order tensor M	
$\overline{\overline{\mathbf{I}}}$	Identity tensor	$\overline{\overline{\mathbf{I}}}_{ij} = \delta_{ij}$
$\overline{\overline{\nabla}}$	Gradient tensor	$\overline{\overline{\nabla}}\phi_{ij} = \frac{\partial \phi_i}{\partial x_j}$
$\langle \cdot, \cdot \rangle$	Euclidian scalar product	
$\ \cdot \ $	Euclidian norm	$\ \phi \ = \sqrt{\langle \phi, \phi \rangle}$
T	Transposition operator	$\overline{\overline{\mathbf{M}}}_{ij}^T = \overline{\overline{\mathbf{M}}}_{ji}$
$\nabla \cdot (\mathbf{u} \otimes \mathbf{u})$	Convective tensor	$\nabla \cdot (\mathbf{u} \otimes \mathbf{u})_{ij} = u_j \frac{\partial u_i}{\partial x_j}$
\iiint_{Ω}	Volume integral over the volume Ω	
$\iint_{\partial\Omega}$	Surface integral of the surface enclosing Ω	
$\partial\Omega$	Surface enclosing the volume Ω	
dS	Surface element	[m ²]
dV	Volume element	[m ³]
dS	Surface element vector	dS = ndS
\mathbf{n}	Outwards oriented normal vector	
$\tilde{\phi}$	Normalised variable as defined in the NVD diagram	$\tilde{\phi} = \frac{\phi - \phi_U}{\phi_D - \phi_U}$
\times	Vectorial cross-product	
\Re	Real part of a complex number	
i	Imaginary number	$i^2 = -1$

Greek symbols

β	Interpolation factor	
Δ	Variation	
$\delta(t)$	Dirac function	
δ_{ij}	Kronecker symbol	$\begin{cases} \delta_{ij} = 1 & i = j \\ \delta_{ij} = 0 & i \neq j \end{cases}$
η	Free-energy density	
γ	Blending factor / Surface energy density	
θ	Correction angle of the free-surface algorithm	
ϵ	Non-linearity parameter	$\epsilon = \frac{1}{\sqrt{2W_e}}$
ϕ	Scalar variable	
ξ	Cahn-Hoffmann vector	
φ	Intensive variable	
λ	Wave length	[m]
μ	Dynamic viscosity	[kg/(m.s)]
ν	Kinematic viscosity	[m ² /s]
ρ	Density	[kg/m ³]
σ	surface tension coefficient	[N/m]
$\overline{\tau}$	Viscous stress tensor	[kg/(m ² .s ²)]
ω	Angular frequency	[rad/s]
ϵ_0	Disturbance amplitude	[-]
ρ_0	plane constant	

Latin symbols

A	Surface vector of a polygon	
<i>A</i>	Polygon area	[m ²]
b	Body forces field	[kg/(m ² .s ²)]
Co	Courant number	[-]
<i>c</i>	Void-fraction	[-]
<i>c_ℓ</i>	Sound celerity in a liquid	[m/s]
<i>D</i>	Diameter	[m]
<i>f</i>	Frequency	[s ⁻¹]
G	Centroid	
<i>g</i>	Bulk free-energy density	
\mathcal{G}	Free-energy	
<i>h</i>	Sheet thickness pertubation $h = h(x)$	[m]
<i>K</i>	Bulk modulus	[m.s ² /kg]
<i>k</i>	wave number	[m ⁻¹]
\mathcal{L}	Lagrangian energy density	
\overline{m}	Surface-tension tensor	
<i>N_V</i>	Number of vertices of polygon	[-]
Oh	Ohnesorge number	[-]
<i>p</i>	Pressure	[N/m ²]

Q	Liquid to gas ratio	[-]
Re	Reynolds number	[-]
R	Nozzle outlet radius	[m]
\mathbf{r}	Position vector	[m]
r	Radius $(0 \leq r \leq R)$	[m]
St	Strouhal number	[-]
T	Excitation period	[s]
t	Time	[s]
\bar{U}	Convective velocity	[m/s]
u	Cartesian velocity component in x-direction	[m/s]
V	Volume	[m ³]
v	Cartesian velocity component in y-direction	[m/s]
v	Specific volume	[m ³ /kg]
w	Cartesian velocity component in z-direction	[m/s]
$w(t)$	Time-window function	[-]
\mathbf{w}	Vector field	
\mathbf{w}_d	Divergence-free vector field	
We	Weber number	[-]
x	Abscissa coordinate	[m]
y	Sheet centerline position	[m]
Z	Displacement of the piezoelectric base	[m]
a_0	Undisturbed sheet thickness	[m]
f_0	Fundamental frequency	[s ⁻¹]
k^*	Normalised wavelength	[-]
k_θ	Azimuthal disturbance wavelength	[rad ⁻¹]
\bar{Q}	Outgoing mass flux satisfying mass conservation	[kg/s]
Q^*	Outgoing mass flux not satisfying mass conservation	[kg/s]
Q_+^*	Part of Q^* leaving the computational domain	[kg/s]
Q_-^*	Part of Q^* entering the computational domain	[kg/s]
r_0	Undisturbed jet radius	[m]
U_z	Velocity of the piezoelectric base	[m/s]
u_0	Undisturbed velocity	[m/s]
u_r	Cylindrical velocity component in radial direction	[m/s]
u_θ	Cylindrical velocity component in angular direction	[m/s]
u_z	Cylindrical velocity component in axial direction	[m/s]
\mathbf{u}_b	Velocity at the surface of a CV due to grid motion	[m/s]
\mathbf{u}_B	Outlet velocity satisfying mass conservation	[m/s]
\mathbf{u}_B^*	Predicted outlet velocity	[m/s]
x_P	Polygonal edge constant	
$\Delta\bar{Q}$	Outgoing mass flux correction	[kg/s]
ΔZ_{max}	Displacement amplitude of the piezoelectric base	[m]
ΔU_{zmax}	Velocity amplitude of the piezoelectric base	[m/s]

Subscripts

<i>B</i>	Boundary-face centered location
<i>C</i>	Cell centered location
<i>D</i>	Downwind location
<i>FS</i>	Lying on the free surface
<i>P</i>	Cell centered location
<i>ST</i>	Relative to surface-tension
<i>U</i>	Upwind location
<i>f</i>	Cell-face centered location
<i>g</i>	Relative to the gaseous phase
<i>l</i>	Relative to the liquide phase
<i>m</i>	Mean value
<i>r</i>	Radial component
<i>tr</i>	Truncated
<i>z</i>	Axial component
θ	Angular component

Superscripts

'	Fluctuation
---	-------------

Abbreviations

CSF	(C)ontinuum (S)urface (F)orce
CV	(C)ontrol (V)olume
DNS	(D)irect (N)umerical (S)imulation (of turbulence)
HRIC	(H)igh (R)esolution (I)nterface (C)apturing (differencing scheme)
NVD	(N)ormalised (V)ariable (D)iagram
rms	(r)oot (m)ean (s)quared
eq.	(eq)uation
fig.	(fig)ure
tab.	(tab)le

Chapter 1

Introduction

1.1 Motivation

Over the last decade, a lot of research effort has been put into the understanding of the physics of liquid sprays and atomization processes. This research field has been mainly driven and sponsored by the automotive industry since, especially in western Europe, the environmental regulations have imposed on the car industry over the years more and more restrictive requirements in terms of pollutants (NO_x, CO) and particle (soot) emission. One of the key points to achieve these requirements is to produce during injection a spray which is as homogeneous as possible and produces as small droplets as possible, in order to obtain the greatest possible reacting surface for the later combustion process taking place in the piston bowl of the car engine. For typical applications in the chemical industry, fluid atomization has to produce droplets of uniform size with high efficiency and low maintenance costs. The fulfillment of such criteria is most of the time achieved by designing or choosing an appropriate atomization nozzle. But this process still requires substantial experimental work to find out the best nozzle adapted to a particular purpose. Some of the effort spent on such process could be spared if one could understand the nozzle internal flow pattern and its subsequent influence on the jet breakup behavior. Unfortunately, even though the physics of jet breakup are in principle well understood, the nozzle internal flow is not and it is very often simply assumed that the flow leaving the nozzle outlet is fully turbulent. This assumption may be justified in some cases, but it demonstrates how little is known about the flow history before the fluid exits from nozzles to form a jet. This is often related to the tiny dimensions of the nozzle – typically in the range of 200 to 500 micrometers – used in practice for which a non-intrusive and detailed measurement of the flow features is very difficult if not impossible.

On the other hand, numerical methods capable of dealing with the flow simulation involving gas-liquid interfaces subjected to surface tension effects have also made their appearance over the last decade. With the gradual increase of the computational power, these methods are slowly proving that they are becoming a worthy tool for the analysis and understanding of free-surface flows, as Finite-Element methods for structural analysis have. With the help of the numerical methods, it is nowadays possible to accurately simulate in a reasonable amount of time, depending on the size of the computational grid, all the flow details that are currently not accessible to measurement procedures. This does not mean that numerical simulations can replace experiments, since they have to provide data to validate or invalidate the computational models. But, the purpose of this work is to show that numerical methods based on the Navier-Stokes

equations for fluid motion are able to complement experiments and provide better insight into the physics of jet breakup and into the related nozzle internal flow.

1.2 Previous and related work

The understanding and control of spraying processes has always been considered to be a key technology and a lot of effort has been put into research and development of new methods to produce sprays with desired atomization and/or breakup properties. Among these, there has always been a particular interest in the breakup behavior of liquid jets. Applications are numerous: ink-jet printing, coating, precise dosage of liquids, to cite but a few. The first investigations on such kind of flows and their related instability date back to the work of Weber [107] and Lord Rayleigh [84], who showed that a round laminar jet undergoes breakup if submitted to a disturbance whose wavelength is greater than the jet circumference. His theory has been complemented by various authors by adding further complexity in the equations describing the instability mechanism leading to the primary jet breakup [16, 33, 51, 89, 101] and also, complemented and validated by experimental observations [16, 23, 29, 51, 90]. A complete and unified theory allowing to understand and predict the jet breakup behavior on the base of the simplified Navier-Stokes equations appears with the work of Keller *et al.* [44] in which the liquid was considered to be inviscid and the surrounding air neglected. The work was extended by Leib & Goldstein [54] to include dependence on the velocity profile of the liquid flow. In the same period, Reitz & Braco [85] and Lin *et al.* [64] proposed a unified theory based on the linearized Navier-Stokes equations, thus including viscosity influence and possible effects due to the surrounding gas, complemented by the publications of Lin *et al.* [60, 61, 65]. However, there is still a lack of theoretical developments for strongly non-linear deformations of the liquid-gas interface, although results have been achieved for planar liquid sheets [46, 70, 82, 83] and for thin, annular liquid films [71, 72, 97].

At the present time theoretical constructs were established to account for the break-up behavior of round jets which were quite successful in accurately predicting the breakup for the Rayleigh regime, other authors also developed computational methods for tracking and predicting the deformations of the jet free surface. Chaudhary & Redekopp [16] used a boundary integral method for developing procedures to control jet breakup and droplet formation for ink-jet printing applications; a similar method was used also by Mansour & Chigier [67] and Zinchenko *et al.* [112]. For the latter, the three-dimensional algorithm demonstrated to be able to resolve accurately the spatial interaction of droplets colliding with each other. Nonetheless, all these methods fail to capture droplet separation from the jet and possible droplet merging. Fromm [26] and Mayashek & Ashgriz [69] developed a finite-element based code for the simulation of the temporal behavior of jets undergoing a breakup of Rayleigh type. Both codes used the free surface as one of the boundary conditions of the calculation and subsequently neglected the effects of the surrounding gas. In this case also, the method cannot capture the behavior of the jet after it breaks up into droplets.

With the advent of the so-called *interface-capturing* methods for the simulation of flows involving a free-surface, it was then possible to handle any kind of free-surface deformation and consider in the mean time the effects of the surrounding gas. Interface-capturing methods advect within the computational domain an indicator function to set the position of the free surface.

The basic principle of such methods is to consider the flow being of one single fluid with variable properties which are set according to the value of the indicator function. There exist two major classes of interface-capturing methods: the so called *level-set methods* [79, 102, 103] and the *Volume-of-Fluid (VOF) methods* [10, 37]. The most popular is the VOF method mainly because they use the void-fraction as indicator function rather than a weighted distance function. The void-fraction of one phase appears in the definition of convective fluxes in all conservation equations and makes the method fully conservative; on the other hand, the level-set function has no physical meaning for the conservation equations, thus requiring special measures to ensure mass conservation. Although the VOF type methods were not designed originally to deal with free-surface flows with surface tension effects, Brackbill *et al.* and, later, Lafaurie *et al.* [13, 50] introduced the concept of *Continuum Surface Force (CSF)* for representing surface tension forces at a gas-liquid interface, which is, when using a VOF-type method, typically smeared over two or three cell-layers. However, the application range of the simulations undertaken has long remained limited to two-dimensional investigations of spatially developing instabilities [43, 49, 58, 111] on the jet free surface. A review of the variations on the numerical methods used for this purpose can be found in a recent review article [91]. With the increase of computer speed and the possibility of running simulations on massively parallel computers, it became possible to undertake the fully three-dimensional computation of the primary breakup of liquid jets [6, 53].

1.3 Author's contribution

The author's contribution can be divided into two parts: The first part is devoted to the analysis of the numerical method used for the simulation of the breakup of jets (software package *Comet*, [15]) and to its improvement for this purpose. The second part is devoted to the validation of the numerical method concerning the capture of the flow phenomena involved in the primary breakup of jets. For this purpose, numerous simulations of nozzle and jet flows have been performed and the results compared with experimental data, published work relating to the theory of the breakup of liquid jets and, when at hand, with other analysis software. The result is an extended knowledge about the predictability of primary jet break-up and its dependence on the nozzle internal flow.

The present work started in 1998 within the framework of a German Priority Program on atomization and spray processes sponsored by the German Research Foundation (DFG). The goal of this interdisciplinary work involving researchers and scientists all over Germany was to understand and gain knowledge in the key technology of sprays and spraying systems. From the simulation work undertaken in collaboration with various groups within the project period 1998–2004, only the part concerning the numerical simulation of jet breakup will be presented herein. Since the major interest was to accurately capture jet breakup, droplet formation, and interactions between droplets (such as possible merging), the numerical method has been validated by the simulation of the Rayleigh breakup [3] and it was found that the VOF method outperforms the moving grid methodology regarding the prediction of the deformations of the gas-liquid interface. Based upon the gained knowledge, especially concerning the building of numerical grids in order to obtain the best accuracy, the simulation of the flow found in pneumatic extension nozzles has been undertaken [4]. The principle of pneumatic nozzles is to make use of a surrounding air flow to stretch a capillary jet before it undergoes Rayleigh breakup and

finally produces droplets whose diameter is much smaller than that of the capillary tube the jet issued from. Also, a similar methodology was used for the study of the breakup behavior of sinusoidally forced jet with a simple actuation model [2, 95]. Because of the difficulty to estimate the impact of the boundary conditions on the flow, the internal nozzle flow was considered as well and the resulting jet breakup compared to the simple actuation [3, 5]. Because of the cylindrical symmetry of the investigated flow domain, the flow simulations have been so far undertaken with the simplifying assumption of axisymmetric two-dimensionality. With regard to droplet formation due to three-dimensional disturbances, the assumptions made so far were not valid any more and, for the first time on this kind of applications, the three-dimensional simulation of the sinusoidally forced breakup of a jet was undertaken [6]. These simulations demonstrate the complementary features of numerical analysis relative to experiments, since in simulations uncertainty in boundary conditions and the influence of various parameters can be easily investigated.

Since the present work deals with the simulation of free-surface flows, it has been necessary to develop a method for the solver *Comet* in order to setup properly the initial position of the free-surface on a numerical grid of arbitrary topology. This method has also been successfully applied to other type of flows involving the presence of a free-surface [11]. Also, in order to cope with possible vortical structures passing through boundaries, a convective outlet boundary condition for arbitrary meshes has been developed and tested on reference test cases. This new procedure can also be applied to the outlet boundary of flows involving a free-surface.

1.4 Outline of the thesis

Chapter 2 deals first with a brief description of the numerical method as implemented into the Navier-Stokes solver *Comet*. One of the interesting features of this solver is its free-surface modeling capability with both interface-tracking and interface-capturing method. Since the preferred method for free-surface treatment in the simulations presented hereafter is of the interface-capturing type, special emphasis is laid on its description and how the initial position of the free surface can be set within the computational domain. Since the flow phenomena investigated in Chapter 3 are influenced by surface-tension effects, some issues about the numerical modeling of surface-tension are presented and discussed. Finally, a new type of convective outlet boundary condition is introduced, details of its implementation and application examples are presented.

Chapter 3 deals with the simulation of flows subjected to surface tension effects. It is first demonstrated that the numerical method described in Chapter 2 is not only able to capture accurately jet breakup and droplet formation as it occurs for the Rayleigh breakup but also correlates well with expected behavior when the imposed actuation frequency increases. For high excitation frequencies, the obtained deformations of the jet free surface is extensively compared with experimental data and theoretical work as found in the literature. Also, the nozzle flow is analyzed and in this respect the influence of the fluid compressibility is taken into account. Finally, a simulation of the air-flow sustained breakup of a capillary jet is presented. In this particular kind of application, contrary to the other simulations, the disturbances arise solely from the surrounding gas flow and are not imposed.

Finally, the last chapter gives a summary of the achieved results and conclusions that can be drawn. Also, the necessary future work is discussed.

Chapter 2

Numerical Method

This chapter deals with the numerical method employed for the simulations presented in this work and some aspects specific to the numerics for simulating spray breakup are outlined. First, the underlying mathematical model – the Navier-Stokes equation for fluid motion – is introduced and details of the numerical method implemented in the commercial solver-package *comet*, that has been used as starting point for the simulations, are presented. Since the numerical computations of this work involve the deformations of a free-surface, the different existing methods for modeling free-surface flows are reviewed and a special emphasis is made on how to set the initial position of the free-surface on arbitrary polyhedral grids as well as on modeling surface-tension forces within the general framework of the diffuse-interface theory. Finally, because standard Neumann boundary conditions at outlet may influence the solution within the computational domain, it has been judged necessary for the present simulations to implement a convective boundary condition, for which it is shown that some improvement is achieved in reducing the influence zone of the outlet boundary.

2.1 Outline of the Navier-Stokes solver

The mathematical model on which the numerical simulations presented in this work are based are the Navier-Stokes equations for incompressible media. These equations sum up in a set of two conservation equations: one conservation equation for the mass, eq. (2.1), and one vectorial equation for the conservation of momentum, eq. (2.2):

$$\langle \nabla, \mathbf{u} \rangle = 0 \quad (2.1)$$

$$\rho \frac{\partial \mathbf{u}}{\partial t} + \rho \nabla \cdot (\mathbf{u} \otimes \mathbf{u}) = -\nabla p + \nabla \cdot \bar{\bar{\tau}} + \mathbf{b}, \quad (2.2)$$

where \mathbf{u} and p represent respectively the velocity and pressure fields, $\bar{\bar{\tau}}$ the viscous stress tensor and \mathbf{b} the sum of body forces. Under the assumption that the fluid is Newtonian, has constant physical properties and is incompressible, the viscous stress tensor $\bar{\bar{\tau}}$ reduces to:

$$\bar{\bar{\tau}} = \mu \left(\bar{\nabla} \mathbf{u} + \bar{\nabla} \mathbf{u}^T \right) \quad (2.3)$$

The conservation equations (2.1) and (2.2) can be rewritten in integral form:

$$\iint_{\partial V} \langle \mathbf{u}, d\mathbf{S} \rangle = 0 \quad (2.4)$$

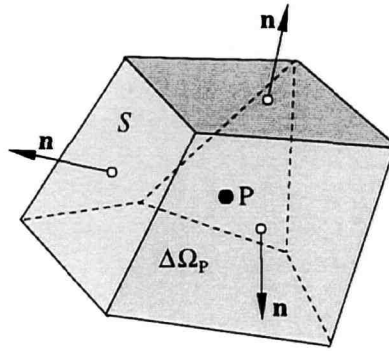


Figure 2.1: Example of a control volume with outwards oriented normals \mathbf{n} .

$$\frac{\partial}{\partial t} \iiint_V \rho \mathbf{u} dV + \iint_{\partial V} \rho \mathbf{u} \cdot \mathbf{n} dS = - \iint_{\partial V} p dS + \iint_{\partial V} \bar{\tau} \cdot \mathbf{n} dS + \iiint_V \mathbf{b} dV \quad (2.5)$$

In equations (2.4) and (2.5), V and ∂V denote respectively the volume of a control volume and its bounding surface with the outwards-oriented surface vector $d\mathbf{S}$, where $d\mathbf{S} = \mathbf{n}dS$, \mathbf{n} being the unit vector normal to the surface and directed outwards, and dS is the surface element, see Fig. 2.1. These equations are discretized with a finite-volume technique using a colocated arrangement of variables. The method has been designed to handle control volumes of arbitrary polyhedral shape (for an example, see Fig. 2.1) and allows the use of local grid-refinement. Discretization of volume and surface integrals is second-order in space: midpoint rule, linear interpolation and central differences are applied [25]. On coarse grids, especially in order to prevent oscillatory solutions, the central differencing scheme may be blended with a certain amount of upwind differences. Time integration is fully implicit and it can be chosen between a two-time (1st order) or a three-time-level method (2nd order), as described in [96]. Pressure-velocity coupling is solved with a SIMPLE algorithm [14]. The solution method is of sequential type: the equations are first linearized and the resulting algebraic equation system is solved in turn for all variables. This is repeated within each time step (*outer iterations*) until the coupled, non-linear set of equations is satisfied. Linear equation systems are solved by iterative solvers of the conjugate-gradient family – CGS for symmetric and CGSTAB for non-symmetric matrices [25, 30].

For the purpose of achieving sufficient accuracy, the computational domain is often subdivided by a numerical grid into several millions of control volumes. Efficient solution of the resulting systems of linear equations involving themselves millions of unknowns can only be fulfilled on high-performance, parallel computers. The numerical method used here has been parallelized by domain decomposition in both space and time: the spatial domain is subdivided into subdomains which are assigned to individual processors, and several time steps can be processed in parallel (by different processors on the *same* subdomain). The efficiency of the method has been tested in single-fluid flows [93, 94, 96]. The communication between processors during the solving process is warranted by the standard message-passing libraries PVM or MPI.

2.2 About the modeling of free-surface flows

Regarding the simulation of free-surface flow, there exist two classes of methods denoted in the literature respectively by *interface-capturing* and *interface-tracking* methods.

2.2.1 Interface-tracking methods

Interface-tracking methods consist in deforming one or more boundaries of a given numerical mesh according to a given boundary condition. The boundary condition is chosen so that it can model a free surface. Typically, the pressure at the boundary is set to be the surrounding atmospheric pressure - *dynamic boundary condition* - and the relative velocity component normal to the free-surface is set to zero - *kinematic boundary condition* - since no flow is allowed to escape through this boundary. In order to match both boundary conditions, the Navier-Stokes equations are first solved on a given mesh using the dynamic boundary condition. The solution thus obtained violates in general the kinematic condition - non-zero mass fluxes are obtained at the free-surface. In the second step, the free surface is displaced in order to avoid fluid crossing through it. An example of such a method (also implemented in *Comet*) has been published by Muzafferija & Perić [76], where several other related methods are described. The procedure described above implies for the computation of steady as well as for unsteady flows a regridding of the computational domain after each outer iteration during the solving process. When regridding takes place, each control-volume deforms and an additional equation, the so-called *space conservation equation* is solved in order to maintain overall volume conservation:

$$\frac{d}{dt} \int_V dV - \int_{\partial V} \langle \mathbf{u}_b, \mathbf{n} \rangle dS = 0, \quad (2.6)$$

where \mathbf{u}_b denotes the velocity at the surface of the control volume due to grid motion.

Interface-tracking methods are well-suited for flows for which the free-surface deformations are not too severe. They have been successfully applied e.g. in the simulation of flow around ship bodies of simple shape [59] or, more recently, in the simulation of thin liquid film flows [22]. Nevertheless, they are not usually able to model flows for which a breaking or a separation of the free surface takes place. Unless a special regridding technique is devised, the mesh deformations become so severe that the grid becomes locally highly skewed. As a consequence, the numerical method fails to deliver a converged solution. Although one could apply regridding techniques to avoid deterioration of mesh quality, such a method is even conceptually complicated and - to the best of the author's knowledge - has not yet been used for flows involving free-surface break-up. Since the present work is involved in the simulation of flows for which the breakup and the merging of the free surface under the influence of surface tension is essential, this kind of method, although available, has not been applied due to the reasons cited herebefore.

2.2.2 Interface-capturing methods

Interface-capturing methods on the other hand use a fixed grid and solve an additional equation in order to set the position of the free surface. According to the nature of the variable solved for, interface-capturing methods can be subdivided into two groups. The first group corresponds to the classical Volume-Of-Fluid (in short VOF) methods introduced by Harlow & Welsh [35]

and later by Hirt & Nichols [37]. For this kind of interface-capturing methods, the free-surface separates two regions and only the Navier-Stokes equations for the fluid beneath the free surface are solved. On the opposite, the other group solves the equations for *both* fluids situated on both sides of the free-surface. The free surface is not considered any more as a surface of discontinuity but as a smeared interface separating the different phases of the flow. This group can be further subdivided into two major classes:

- *level-set methods*: Level-set methods are based on the work of Osher & Stanley [79]. They use a distribution function which can be regarded as a measure of the distance from the free surface. The free surface itself is defined as the surface for which the value of the level-set function is equal to zero. Both fluids, above and beneath the free-surface, are taken into account in the level-set model and their physical properties are set according to the value of the level-set function. Like in all models for representing a free surface, the level-set model approximates a Heaviside function so that free-surface position as well as physical properties are well localized in space. For approximating the Heaviside function as closely as possible, the fluid properties are only allowed to vary rapidly over two or three control volumes layers around the zero-level of the function. In order to satisfy that the mass of each phase is conserved, the level-set function has to be submitted to a *renormalization* procedure [79, 102].
- *volume-fraction methods*: The volume-fraction methods advect a void-fraction, denoted generally by c , to set both position of the free-surface and physical properties of the fluid phases involved in the free-surface flow. Unlike in the level-set method, for which the level-set function can take any real value, the void-fraction is only allowed to take values between 0 and 1. As a matter of consequence, the physical properties result from a combination (not necessarily linear) of the physical properties of each phase and of the void fraction. The free-surface is then set to the iso-surface for which $c = 0.5$. Since the fluid mixture is considered as a single effective fluid with variable properties – which are obtained as a combination of the respective properties of the fluids involved in the free-surface flow and the void fraction –, it is important that the values of c remain bounded between 0 and 1. For this purpose, a special interpolation practice is required. The interpolation practice allows to have a smooth transition of the values of c across the free surface but, contrary to the level-set methods, it is not warranted that the smearing of the interface remains limited to only few layers of cells, so special measures are needed to ensure sharpness of the interface. However, these methods are inherently conservative.

In this work, the latter method has been employed and its specifics will be described in the next section.

2.3 About the free-surface method used

In the following, the method used in this work for representing the free surface is presented and its major properties are briefly outlined. It would be beyond the scope of this work to go into all details of the model. The interested reader can refer to a very similar work of Ubbink [105] and to the work of Muzaferiya *et al.* [77].

The free-surface method used is of Volume-Of-Fluid (VOF) type and uses a void-fraction for setting the physical properties of each phase within the flow. The void fraction c is advected with the following convection equation:

$$\frac{\partial}{\partial t} \int_V c dV + \int_{\partial V} c \langle \mathbf{u}, \mathbf{n} \rangle dS = 0 \quad (2.7)$$

It is assumed that the phases do not mix, interact or react with each other. The physical properties are then determined by a linear combination of the physical properties of each phase. Suppose there exist only two phases, a gaseous and a liquid one, and if $c = 1$ denotes the liquid phase ℓ and $c = 0$ the gaseous phase g , one obtains for the physical properties of the resulting effective fluid:

$$\mu = (1 - c)\mu_g + c\mu_\ell \quad (2.8)$$

$$\rho = (1 - c)\rho_g + c\rho_\ell \quad (2.9)$$

The velocities and the pressure are assumed to be continuous over the free surface.

2.3.1 Boundedness of the void fraction

With this kind of advection model, it is then necessary to have meaningful values of the physical properties for the effective fluid (it is not allowable to have negative densities or viscosities). This can only be achieved if the values taken by the void-fraction field remain bounded between 0 and 1. For this purpose, special interpolation practice has to be used. The complete interpolation algorithm relies basically on the *normalized variable diagram* (NVD) introduced first by Leonard [56] and Gaskell & Lau [27]. Both references make the use of a diagram introducing the normalized variable formulation based on a one-dimensional composite flux limiter concept to enforce boundedness of the solution [21]. The normalized variable $\tilde{\phi}$ is defined as:

$$\tilde{\phi} = \frac{\phi - \phi_U}{\phi_D - \phi_U}, \quad (2.10)$$

where D and U denote respectively downwind and upwind locations¹. The normalized variable value becomes very helpful to calculate variable values at a cell-face center according to the values in cells sharing the face. With the only knowledge of ϕ_P at the cell center, it is possible to set the value $\tilde{\phi}_f$ with the help of the NVD so that the solution of the discretized equations describing the evolution of the variable ϕ remains bounded. For this purpose, it has been shown in [27] that the value $\tilde{\phi}_f$ must remain in a bounded region of the NVD. The bounded region is represented by the shaded area of Fig. 2.2.

As shown by Ubbink [105], the area may change its shape according to the local value of the Courant-number Co if the time integration procedure for estimating the time variations of the variable ϕ is explicit. In the numerical procedure used in this work, the variable ϕ corresponds to the void-fraction and time integration of the advection equation (2.7) is implicit. The HRIC discretization scheme [77] is used for evaluating the values of the void fraction at the cell-face center. This scheme has the advantage to be bounded and helps the interface remaining sharp. This scheme can be blended partly with the upwind differencing scheme². From the consideration that within one time step, no more fluid can be transported out of the cell than is

¹Note that with this formulation, one has $\tilde{\phi}_D = 1$ and $\tilde{\phi}_U = 0$.

²Note that the upwind differencing scheme is always bounded according to the NVD.

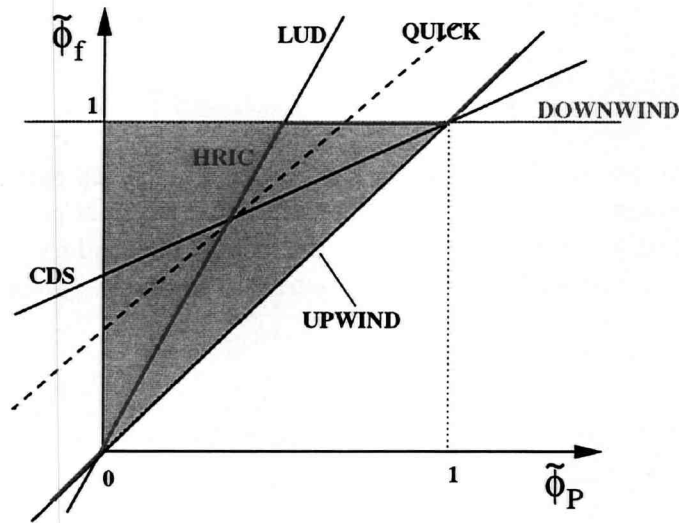


Figure 2.2: Normalized variable diagram (NVD) with various discretization schemes: upwind (UPWIND), downwind (DOWNWIND), linear upwind (LUD), central differences (CDS), quick (QUICK) [55], high-resolution interface-capturing (HRIC) [77]. The shaded area represents the zone where the values of $\tilde{\phi}_f$ are bounded.

available within the cell, the value previously calculated has to be corrected with the Courant number Co defined locally at the cell face by:

$$Co = \frac{\langle \mathbf{u}, \mathbf{n} \rangle_f ||S_f|| \Delta t}{\Delta \Omega_P} \tag{2.11}$$

Because of the high amount of the downwind scheme used when $\tilde{c}_P > 0.5$, the authors of [77] have found that the interface tends to align with the grid so that a correction is undertaken according to the angle θ between the interface and the grid (Fig. 2.3).

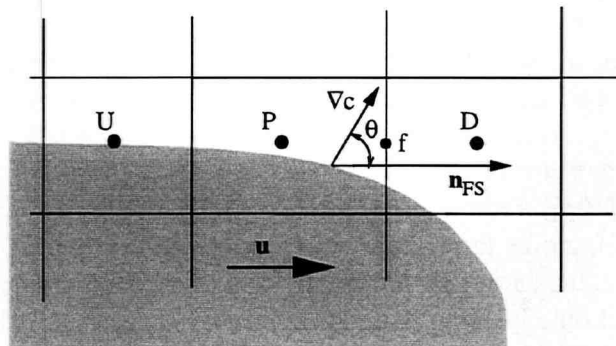


Figure 2.3: Definition of the correction angle θ

This leads to the following algorithm for the calculation of the void fraction at the cell-face center:

$$\tilde{c}_f = \begin{cases} \tilde{c}_P & \tilde{c}_P \leq 0 \\ 2\tilde{c}_P & 0 < \tilde{c}_P \leq 0.5 \\ 1 & 0.5 < \tilde{c}_P \leq 1 \\ \tilde{c}_P & 1 < \tilde{c}_P \end{cases} \quad (2.12)$$

HRIC differencing scheme

$$\tilde{c}_f^* = \begin{cases} \tilde{c}_f & Co < 0.3 \\ \tilde{c}_P + (\tilde{c}_f - \tilde{c}_P) \frac{0.7 - Co}{0.7 - 0.3} & 0.3 \leq Co < 0.7 \\ \tilde{c}_P & 0.7 \leq Co \end{cases} \quad (2.13)$$

Correction according to the Courant-number Co

$$\tilde{c}_f^{**} = \tilde{c}_f^* \sqrt{\cos \theta} + \tilde{c}_P (1 - \sqrt{\cos \theta}) \quad (2.14)$$

Correction according to the angle θ of Fig. 2.3

Finally, the cell-face value of c is obtained by evaluating:

$$c_f = \gamma c_P + (1 - \gamma) c_D, \quad (2.15)$$

where γ is a blending factor defined by:

$$\gamma = \frac{(1 - \tilde{c}_f^{**}) c_D - c_U}{c_D - c_P} \quad (2.16)$$

Limitations of the HRIC-scheme

The HRIC differencing scheme has two major limitations:

- The HRIC scheme is diffusive. It is much less diffusive than an upwind differencing scheme since the HRIC scheme is of higher-order than one. This result could be demonstrated on the convection of a square diagonally to a cartesian mesh [48].
- As pointed out in [27], because of the high amount of the downwind scheme used, for various values of $\tilde{\phi}_P$ in the NVD, the same value of $\tilde{\phi}_f$ can be obtained at the cell-face center, so that the solution is not unique. This behavior has been observed in calculations and explains the tendency observed by the authors of [77] that the interface aligns with the grid lines and a special correction is then necessary to avoid this phenomenon. Nevertheless, for very small slopes of the free surface, alignment of the interface with the grid lines has been also observed.

2.3.2 Setting up initial positions of the free-surface

For most practical calculations involving interface-capturing methods like the one employed in the Navier-Stokes solver *Comet*, it is necessary to initialize the volume fraction field in the

discretized computational domain at the beginning of the numerical simulation. If the grid lines are all aligned with the desired position of the free surface, the initialization becomes then trivial. For instance, above the free-surface, the volume fraction value is set to zero, underneath to one. However, initialization becomes much more complicated when the initial position of the free surface cuts control volumes (whose shape can be arbitrary). Following the work of Kothe *et al.* [47], a solution procedure is proposed here to set properly the volume fraction of a control volume according to its shape and its position relative to the free-surface. This procedure relies on the calculation of volumes which is itself linked to the calculation of polygon areas. As we will see, calculation of volumes can be derived from the calculation of polygon areas. Therefore area calculation is first introduced and followed by volume calculation. Then, it is explained how to calculate areas and volumes truncated by the free surface. Finally, it is described how to set volume fractions and some examples obtained with the method are shown.

Calculation of areas

There are many possibilities to evaluate the area A of a polygon. For a triangle, one can use the well known relation corresponding to the notations of Fig. (2.4):

$$A = \|\mathbf{A}\| = \frac{1}{2} \|(\mathbf{r}_{P_2} - \mathbf{r}_{P_1}) \times (\mathbf{r}_{P_3} - \mathbf{r}_{P_1})\|, \quad (2.17)$$

where \mathbf{A} is the so-called surface vector of the triangle.

For a polygon, it becomes more complicated if its edges do not lie in the same plane. For a quadrangle, as proposed in [47], a possibility is to make a parabolic hyperboloid go through the edges of the oriented surface. This is unfortunately not valid any more for a figure which has more than four edges. A solution is to decompose the polygon into triangles, which is a convenient and simple method to implement. A description of it can be found in [25] as well. Nevertheless, the decomposition is not always unique, depending on the vertex chosen for building the surface vectors. The method proposed hereafter gives a unique decomposition. In the first step, one has to find out the centroid G of the polygonal figure. An estimate of its position is given by³ (see also Fig. 2.5):

$$\mathbf{r}_G \stackrel{def.}{=} \frac{1}{N_V} \sum_{i=1}^{N_V} \mathbf{r}_{P_i}, \quad (2.18)$$

where N_V denotes the number of vertices of the polygon.

The polygon area is then the sum of the triangles built with the centroid and two neighboring vertices. The area vector of the polygon is then considered to be the sum of all the triangle area vectors with the notations of Fig. 2.5:

$$\mathbf{A} = \frac{1}{2} \sum_{i=1}^{N_V} (\mathbf{r}_{P_{i+1}} - \mathbf{r}_G) \times (\mathbf{r}_{P_i} - \mathbf{r}_G) \quad (2.19)$$

³This formulation does give the true centroid position of the polygon only if all its edges are of the same length. In the opposite case, the centroid can be obtained by weighting the products of centroids of the triangulated area and triangle area with the total calculated area. Nevertheless, eq. (2.18) gives a practical approximation of the centroid position.

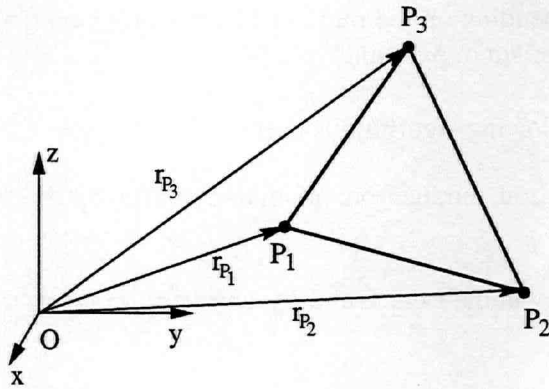


Figure 2.4: Example of a triangular face with its vertices numbered from P_1 to P_3 in counterclockwise order.

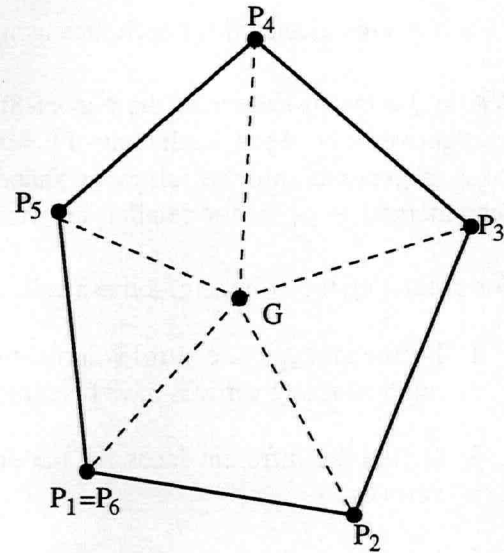


Figure 2.5: Example of a polygon. G denotes the centroid of the polygon.

Finally the area A of the polygon is obtained by taking the Euclidian norm of \mathbf{A} , i.e. $A = \|\mathbf{A}\| = \sqrt{\langle \mathbf{A}, \mathbf{A} \rangle}$. For a planar polygonal face, the calculated value is then exact.

Calculation of volumes

The volume V of the control volume Ω is obtained with the trivial identity:

$$V = \iiint_{\Omega} dV \tag{2.20}$$

As we have the identity $\langle \nabla, \mathbf{r} \rangle = 3$, one can rewrite using Gauss' theorem:

$$V = \iiint_{\Omega} dV = \frac{1}{3} \iiint_{\Omega} \langle \nabla, \mathbf{r} \rangle dV = \frac{1}{3} \iint_{\partial\Omega} \langle \mathbf{r}, d\mathbf{S} \rangle \tag{2.21}$$

Discretizing eq. (2.21) on a control volume of arbitrary shape, one obtains the following approximation for the volume V :

$$V \approx \frac{1}{3} \sum_f \langle \mathbf{r}, \mathbf{S} \rangle_f, \tag{2.22}$$

where the index f denotes faces of the control volume. Using mid-point rule, \mathbf{r} corresponds to the position in space of the face centroid; \mathbf{S} corresponds to the face surface vector pointing *outwards*. The surface must be then correctly *oriented*. If all surface vectors are correctly oriented, it can be then written:

$$V \approx \frac{1}{3} \sum_f \langle \mathbf{r}_G, \mathbf{A} \rangle_f. \tag{2.23}$$

\mathbf{r}_G and \mathbf{A} are calculated for each face using the method introduced in the preceding section.

Within the pre-processor of the Navier-Stokes solver *comet*, each control volume is defined by eight vertices. Thus, each control volume has basically a hexahedral form but can, in some cases, degenerate into the following shapes, depending on the number of vertices which have been merged (see [15] for details): tetrahedron, prism or pyramid⁴.

For evaluating the volume of a mesh cell, the following algorithm is used:

1. Define the type of control volume (hexahedron, tetrahedron, prism or pyramid) by checking how many vertices have been merged.
2. Define the different faces for the control volume type found by correctly ordering the vertices.
3. Loop over all faces and calculate surface vector and position of the face center of gravity by using respectively eqs. (2.19) and (2.18).
4. Calculate the cell volume using eq. (2.23).

Calculation of truncated areas

When the free surface is passing through a control volume or a boundary face, it is assumed that the form of the free surface can be approximated by a plane. Thus, the faces which cross the free surface are cut by a line, since the faces are assumed to be almost planar. The area under the free surface is called *truncated area*. It is represented in Figs. 2.6 and 2.7 by the shaded area.

A plane in three dimensions is given by the following relation:

$$\langle \mathbf{r}, \mathbf{n}_{FS} \rangle = \rho_0, \quad (2.24)$$

where \mathbf{n}_{FS} is the vector normal to the plane and ρ_0 is the plane constant. With these two quantities, it is then easy to find out if vertices of a face are above, under or on the free surface. Let's take a vertex of the face and call it P. Then P is above the free surface if $\langle \mathbf{r}_P, \mathbf{n}_{FS} \rangle - \rho_0 > 0$, under the free surface if $\langle \mathbf{r}_P, \mathbf{n}_{FS} \rangle - \rho_0 < 0$ and lies on the free surface if eq. (2.24) is satisfied. To find out at which locations the free surface cuts the face edges, one has to loop over all vertices of the face (practically from P_1 to P_6 in Fig. 2.6). If for two consecutive vertices the value of $\langle \mathbf{r}_P, \mathbf{n}_{FS} \rangle - \rho_0$ changes its sign – for example, on Fig (2.6), $\langle \mathbf{r}_P, \mathbf{n}_{FS} \rangle - \rho_0$ is negative at vertex P_3 and becomes positive at vertex P_4 –, the free surface cuts the edge joining the two vertices.

Let's denote by U the vertex lying under the free surface, by O the vertex above the free surface and F the position of the point at the intersection between the edge built by the line (UO) and the free surface (see Fig. 2.7). The position of F is defined by:

$$\mathbf{r}_F = \beta \mathbf{r}_U + (1 - \beta) \mathbf{r}_O, \quad (2.25)$$

⁴Note that the flow solver can handle cells of arbitrary polyhedral shape, but the pre-processor cannot generate cells other than those defined by eight vertices. The procedure presented herein is designed to work with arbitrary polyhedral cells.

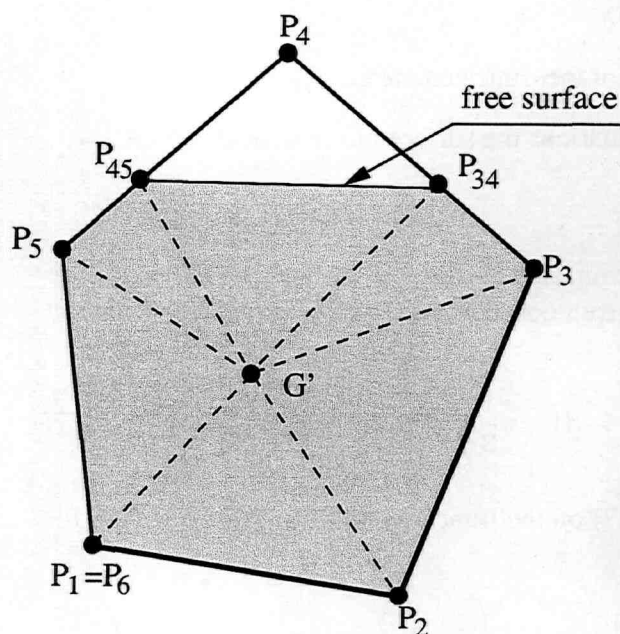


Figure 2.6: Example of a truncated polygon. The area under the free surface (in gray) is the truncated area. The free surface cuts the polygon along a line passing through the points P_{34} and P_{45} . G' denotes the centroid of the truncated area.

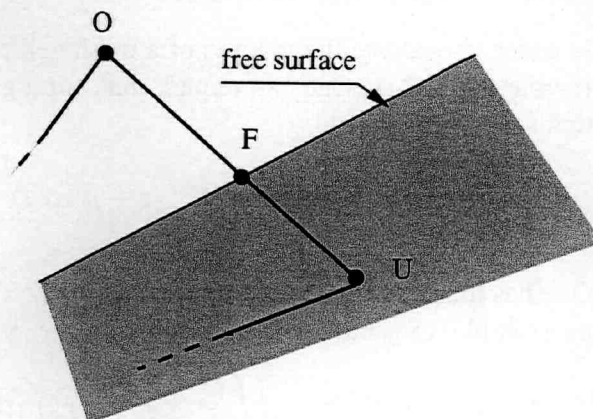


Figure 2.7: Example of an edge cut by the free surface and passing through point F . Vertex U is under the free surface, vertex O is above the free surface.

where β is evaluated with:

$$\beta = \frac{\langle \mathbf{r}_O, \mathbf{n}_{FS} \rangle - \rho_0}{\langle \mathbf{r}_O - \mathbf{r}_U, \mathbf{n}_{FS} \rangle} \quad (2.26)$$

For evaluating the truncated area, the following algorithm is then applied:

1. Set the values of ρ_0 and of the free-surface normal vector \mathbf{n}_{FS} for the face.
2. Collect all vertices P_i of the polygon and set i to 0.
3. Increment i .
4. If $i = N_V + 1$ then goto 11.
5. Define $x_{P_i} = \langle \mathbf{r}_{P_i}, \mathbf{n}_{FS} \rangle - \rho_0$.
6. If $x_{P_i} < 0$, then P_i lies under the free surface and is one vertex of the truncated area. Add P_i to the vertex list of the truncated area. If $x_{P_i} x_{P_{i+1}} < 0$ then goto 9.
7. If $x_{P_i} > 0$, then the vertex P_i lies above the free surface. If $x_{P_i} x_{P_{i+1}} < 0$ then goto 9.
8. Goto 3.
9. Calculate the position of the vertex at the intersection between the line joining P_i to P_{i+1} and the free surface with the help of eq. (2.25). Add the new vertex to the vertex list of the truncated area.

10. Goto 3.
11. Define a new polygon from the vertex list of the truncated area.
12. Calculate with the algorithm for area calculations the surface of the truncated area.

Calculation of truncated volumes

In order to evaluate the volume of a mesh cell truncated by the free surface, it is necessary to rewrite eq. (2.21). One can remark that, for a given constant vector \mathbf{n}_{FS} and a given constant real value ρ_0 that:

$$V = \iiint_{\Omega} dV = \frac{1}{3} \iiint_{\Omega} \langle \nabla, (\mathbf{r} - \rho_0 \mathbf{n}_{FS}) \rangle dV = \frac{1}{3} \iint_{\partial\Omega} \langle (\mathbf{r} - \rho_0 \mathbf{n}_{FS}), d\mathbf{S} \rangle \quad (2.27)$$

One has then to evaluate the integral of eq. (2.27) on the truncated mesh cell (see Fig. 2.8 for an example) to get the desired volume V_{tr} , i.e. :

$$V_{tr} = \iiint_{\Omega_{tr}} dV = \frac{1}{3} \iint_{f_{tr}} \langle (\mathbf{r} - \rho_0 \mathbf{n}_{FS}), d\mathbf{S} \rangle + \iint_{f_{FS}} \langle (\mathbf{r} - \rho_0 \mathbf{n}_{FS}), d\mathbf{S} \rangle, \quad (2.28)$$

where f_{tr} denotes all truncated faces and f_{FS} the truncating plane representing the free surface. If the vector \mathbf{n}_{FS} is set to the truncating plane normal vector and ρ_0 to the corresponding plane constant, eq. (2.24) is then satisfied for the free surface plane and the surface integral relative to f_{FS} vanishes. One obtains then:

$$V_{tr} = \iiint_{\Omega_{tr}} dV = \frac{1}{3} \iint_{f_{tr}} \langle (\mathbf{r} - \rho_0 \mathbf{n}_{FS}), d\mathbf{S} \rangle \approx \frac{1}{3} \sum_{f_{tr}} [\langle (\mathbf{r}_{G'} - \rho_0 \mathbf{n}_{FS}), \mathbf{S} \rangle]_{f_{tr}} \quad (2.29)$$

The following algorithm can then be used for calculating the truncated volume:

1. Define the type of control volume (hexahedron, tetrahedron, prism or pyramid) by checking how many vertices have been merged.
2. Define the different faces for the control volume type by correctly ordering the vertices.
3. Set the value of ρ_0 and \mathbf{n}_{FS} for the control volume.
4. Collect all faces truncated by the free surface.
5. Calculate with the algorithm for the calculation of truncated areas the surface vector and the position of the center of gravity G' of the truncated faces.
6. Evaluate with eq. (2.29) the truncated volume.

Calculation of volumes fractions

Volume fractions can be set for boundary faces of the numerical mesh as well as for the control volumes. For boundary faces, the volume fraction is defined to be the truncated area of the boundary face divided by the face area. The volume fraction for a control volume is defined as the truncated volume divided by the cell volume, i.e. the volume fraction is equal to V_{tr}/V .

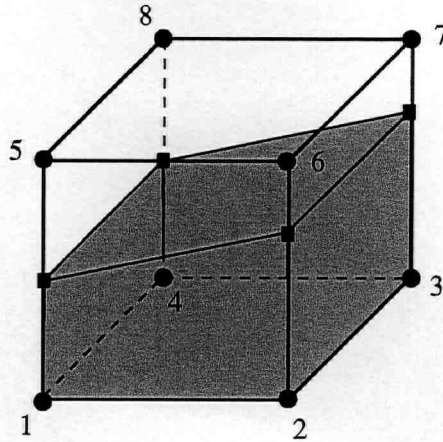


Figure 2.8: Example of a truncated cell with eight nodes numbered from 1 to 8. Numeration corresponds to the right-hand rule used in *comet*. The volume represented in gray is the volume under the free surface plane, i.e. the truncated volume.

Application examples

An application example is shown in Fig. 2.9. A sine wave has been initialized on a cartesian grid of $100 \times 40 \times 20$ control volumes. The wave has 45 degrees inclination to the largest dimension of the numerical grid. The wave has also been rotated by 5 degrees in both other directions. This is achieved by an appropriate rotation of the grid with respect to the direction of the wave propagation. The spatial variations of the wave can be represented as a cylindrical surface which is generated with a sinusoidal function of the form:

$$h(x) = h_0 \sin\left(\frac{2\pi x}{\lambda}\right), \quad (2.30)$$

where h_0 is the wave amplitude, λ the wavelength and x the position along the wave axis of propagation. The surface generated by $h(x)$ is used for representing the free-surface and approximated locally by a plane going through the point defined by the triplet $(x, h(x), 0)$ in the local coordinate system for which the x -axis is aligned with the wave direction of propagation and the y -axis defined by the direction normal to this axis and pointing upwards. With this definition, the normal vector \mathbf{n}_{FS} to the free-surface is obtained with:

$$\mathbf{n}_{FS} = \frac{1}{\sqrt{1 + \left(\frac{dh(x)}{dx}\right)^2}} \begin{cases} -\frac{dh(x)}{dx} = -\frac{2\pi h_0}{\lambda} \cos\left(\frac{2\pi x}{\lambda}\right) \\ 1 \\ 0 \end{cases} \quad (2.31)$$

Since the plane defining the free surface has to go through the point defined by $\mathbf{r} = (x, h(x), 0)$, then the plane constant ρ_0 can be easily calculated, by imposing that ρ_0 has to satisfy eq. (2.24), i.e.:

$$\rho_0 = \frac{-x \frac{dh(x)}{dx} + h(x)}{\sqrt{1 + \left(\frac{dh(x)}{dx}\right)^2}} \quad (2.32)$$

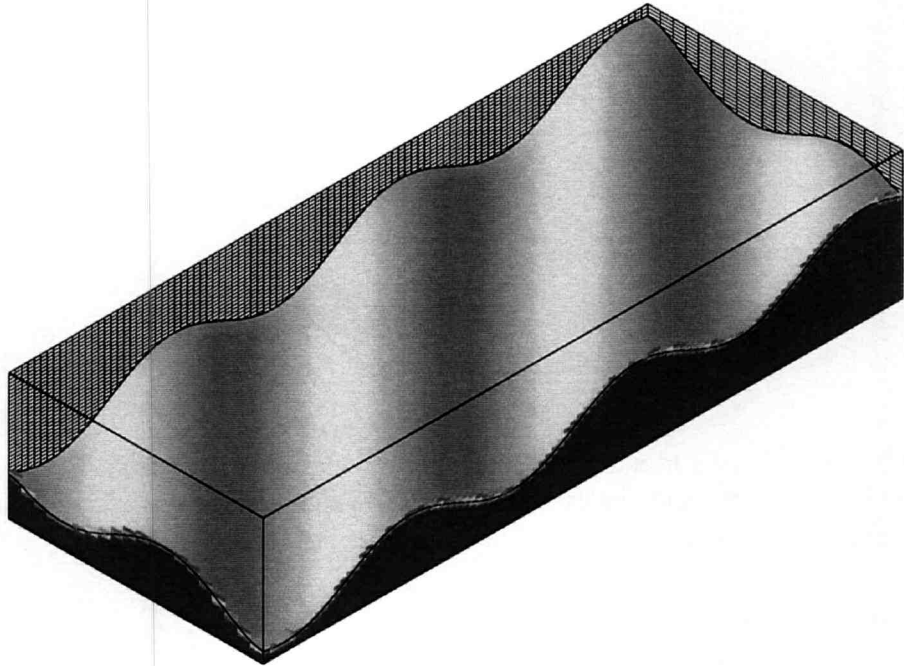


Figure 2.9: Application example of the initialization procedure for a rotated sine wave on a cartesian grid. The obtained free surface is the shaded area.

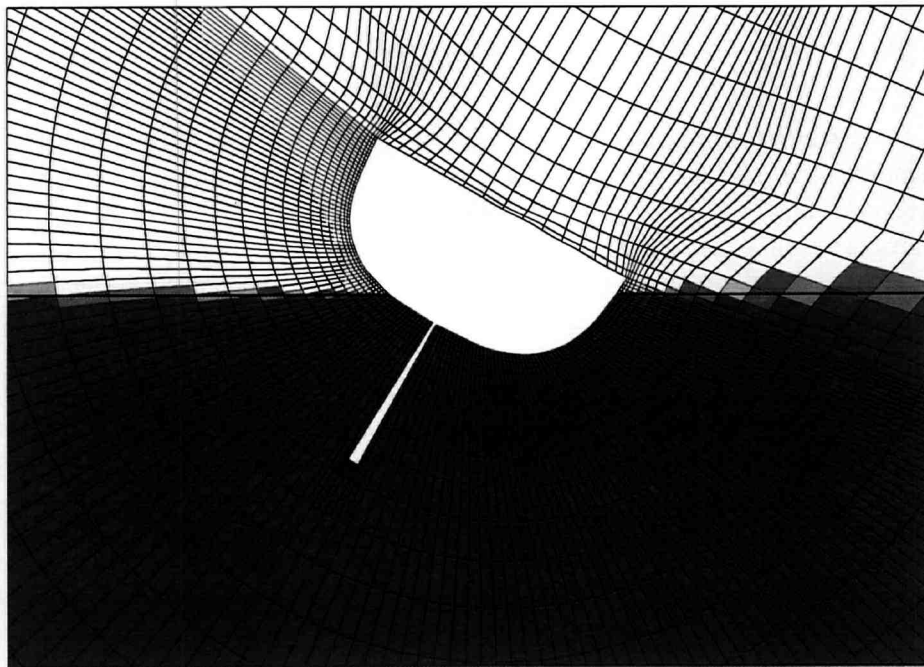


Figure 2.10: Boat with a keel at a roll angle of 30 degrees. Thick line: water plane position; thin lines: numerical grid; in color: volume fraction distribution. Application example used in [11].

Using the above expression, one obtains after initialization the free surface depicted by the shaded area of Fig. 2.9. In this figure, the left and right rear sides also show details of the numerical grid employed, whereas the left and right front sides display the distribution of the volume fraction at the corresponding boundaries. Note that the approximated free surface appears almost perfectly smooth. This verifies that the approximations employed in the initialization method are appropriate.

Another application example is shown in Fig. 2.10. The figure represents a boat with a keel at a roll angle of 30 degrees. In this case, the initial free surface is the plane $z = 0$ and the plane normal vector and constant are even easier to define, i.e. $\mathbf{n}_{FS} = \mathbf{k}$ and $\rho_0 = 0$. However, the grid is generated so that it fits the boat and is therefore not aligned with the free surface. The volume fraction must be initialized so that the iso-surface $c = 0.5$ coincides with the free surface location. The result obtained with the above procedure is shown in Fig. 2.10. The white zone corresponds to the region where the value of the volume fraction is under 0.1%. The water plane so obtained is represented in Fig. 2.10 by the thick line.

2.4 Surface tension modeling

2.4.1 The diffuse interface theory

The diffuse interface theory is based on a free-energy model as proposed in [7–9, 39, 40, 108]. Following this theory, it is possible to develop a model consistent with the physics of surface tension and it allows to explain why surface tension effects can be represented by the continuum surface force (CSF) model [13, 50].

The diffuse interface theory assumes that the interface between two phases has a finite thickness in which physical properties of the fluid vary rapidly but smoothly. Thus, the interface between two fluids is not treated as a surface of discontinuity and physical properties are smeared over a layer of defined thickness. Variations of physical properties are linked to those of an intensive variable φ , which can be the density, as in [8], or the void-fraction c . We will now consider the case when $\varphi = c$. According to the diffuse interface theory, a force, derived from a free-energy functional, acts in the vicinity of the interface⁵. The free energy \mathcal{G} is defined as a functional over the whole integration volume as the integral of a free-energy density η :

$$\mathcal{G} = \iiint_{\Omega} \eta \, dV \quad (2.33)$$

The free-energy density can be modeled by various formulations which can be found in references [7, 40, 108]. It is considered in [108] in a very general sense as a Lagrangian energy density \mathcal{L} depending on the intensive variable c representing the void fraction of a phase in a two-fluid flow. One can then write:

$$\mathcal{G} = \iiint_{\Omega} \mathcal{L}(\nabla c, c, \mathbf{r}) \, dV \quad (2.34)$$

For an isothermal free-energy density field, the energy functional \mathcal{G} is independent of the space location vector \mathbf{r} and from equilibrium state considerations, a force acting on an arbitrary control

⁵With vanishing interface thickness (i.e. in the limit of a sharp interface considered as a surface of discontinuity), one recovers from the force definition the jump conditions over the interface for pressure and velocities [8].

volume can be written as the divergence of a tensor $\bar{\Xi}$ with components [108]:

$$\bar{\Xi}_{jk} = c_{,j} \frac{\partial \mathcal{L}}{\partial c_{,k}} - \delta_{jk} \mathcal{L} \quad (2.35)$$

Considering the general expression proposed in [108] which fits the definitions of the Lagrangian energy densities found in [7, 8, 40], one has:

$$\mathcal{L} = \frac{1}{2} [\gamma(\nabla c^2) + g(c)] , \quad (2.36)$$

where γ represents a surface energy density and g a bulk free energy per unit volume. The tensor $\bar{\Xi}$ then becomes:

$$\bar{\Xi} = \gamma \nabla c \otimes \boldsymbol{\xi} + \mathcal{L} \bar{I} , \quad (2.37)$$

where $\boldsymbol{\xi}$ is the Cahn-Hoffman vector [108] and its components are defined with the following relation for an arbitrary vector \mathbf{q} :

$$\xi_i = \frac{\partial \gamma(\mathbf{q})}{\partial q_i} \quad (2.38)$$

2.4.2 The Continuum Surface Force (CSF) approach

In the CSF approach, the model for the free energy density has a very simple expression, since $\gamma(\nabla c^2) = \sigma \|\nabla c\|$ and $g(c) = 0$, where σ denotes the surface-tension coefficient [40]. According to the diffuse interface theory, the surface tension force is then represented as the divergence of a tensor \bar{m} (see Eq. (2.37)):

$$\bar{m} = \sigma \|\nabla c\| \bar{I} - \sigma \frac{\nabla c \otimes \nabla c}{\|\nabla c\|} \quad (2.39)$$

Taking the divergence of this \bar{m} , one obtains:

$$\nabla \cdot \bar{m} = \sigma \left[\nabla(\|\nabla c\|) - \nabla \cdot \left(\frac{\nabla c \otimes \nabla c}{\|\nabla c\|} \right) \right] \quad (2.40)$$

Considering that $\|\nabla c\| \stackrel{def.}{=} \sqrt{\langle \nabla c, \nabla c \rangle}$ and that

$$\left[\frac{\nabla(\langle \nabla c, \nabla c \rangle)}{2} - \nabla \cdot (\nabla c \otimes \nabla c) \right]_j = \frac{1}{2} \frac{\partial}{\partial x_j} \left[\frac{\partial c}{\partial x_i} \frac{\partial c}{\partial x_i} \right] - \frac{\partial}{\partial x_k} \left[\frac{\partial c}{\partial x_j} \frac{\partial c}{\partial x_k} \right] \quad (2.41)$$

$$= \frac{\partial^2 c}{\partial x_j \partial x_i} \frac{\partial c}{\partial x_i} - \frac{\partial^2 c}{\partial x_k \partial x_k} \frac{\partial c}{\partial x_j} - \frac{\partial c}{\partial x_k} \frac{\partial^2 c}{\partial x_k \partial x_j} \quad (2.42)$$

$$= - \frac{\partial^2 c}{\partial x_k \partial x_k} \frac{\partial c}{\partial x_j} \quad (2.43)$$

$$= [- \langle \nabla, \nabla c \rangle \nabla c]_j , \quad (2.44)$$

one finally obtains:

$$\frac{1}{\sigma} \nabla \cdot \bar{\bar{m}} = \frac{\nabla(\langle \nabla c, \nabla c \rangle)}{2\|\nabla c\|} - \nabla \cdot \left(\frac{\nabla c \otimes \nabla c}{\|\nabla c\|} \right) \quad (2.45)$$

$$\begin{aligned} &= \frac{\nabla(\langle \nabla c, \nabla c \rangle)}{2\|\nabla c\|} - \frac{1}{\|\nabla c\|} \nabla \cdot (\nabla c \otimes \nabla c) \\ &\quad - \nabla \left(\frac{1}{\|\nabla c\|} \right) \cdot (\nabla c \otimes \nabla c) \end{aligned} \quad (2.46)$$

$$= -\frac{\langle \nabla, \nabla c \rangle \nabla c}{\|\nabla c\|} - \nabla \left(\frac{1}{\|\nabla c\|} \right) \cdot (\nabla c \otimes \nabla c) \quad (2.47)$$

$$= -\left(\frac{\langle \nabla, \nabla c \rangle}{\|\nabla c\|} + \left\langle \nabla \left(\frac{1}{\|\nabla c\|} \right), \nabla c \right\rangle \right) \nabla c \quad (2.48)$$

$$= -\left\langle \nabla, \frac{\nabla c}{\|\nabla c\|} \right\rangle \nabla c \quad (2.49)$$

Finally, the surface-tension force can be expressed as:

$$\nabla \cdot \bar{\bar{m}} = \sigma \kappa \nabla c \quad (2.50)$$

$$\kappa = -\left\langle \nabla, \frac{\nabla c}{\|\nabla c\|} \right\rangle \quad (2.51)$$

This is currently the expression found in the CSF-model of [13, 50] and the formulation used for the surface tension in *comet*. It is represented as a body force \mathbf{b}_{ST} and is evaluated using a volume integral over an arbitrary control volume:

$$\mathbf{b}_{ST} \stackrel{def.}{=} - \iiint_{\Omega_P} \sigma \kappa \nabla c dV, \quad (2.52)$$

where κ is obtained from expression (2.51). The surface-tension force is then discretized in a non-conservative way on a control volume centered on P , assuming a constant surface-tension coefficient:

$$\mathbf{b}_{ST} \approx -\sigma \kappa_P \iiint_{\Omega_P} \nabla c dV. \quad (2.53)$$

Using Gauss' theorem, the volume integral can be transformed into a surface integral and the final expression for the surface tension force is:

$$(\mathbf{b}_{ST})_P \approx -\sigma \kappa_P \iint_{\partial\Omega_P} c \mathbf{n} dS \approx -\sigma \kappa_P \sum_f c_f \mathbf{n}_f S_f. \quad (2.54)$$

2.4.3 Parasitic currents

When convective fluxes as well as curvature radii of the interface tend to vanish, an unphysical velocity field develops when the procedure described above is used to represent surface-tension effects in a VOF scheme. This velocity field is known in the literature as *parasitic currents* (see also [91] for a review of the problem). The reason of their existence is explained in the following.

Observing, as described in [20], that the Hodge decomposition of a vector field \mathbf{w} on a bounded domain Ω satisfies:

$$\iint_{\partial\Omega} \langle \mathbf{w}, \mathbf{n} \rangle dS = 0, \quad (2.55)$$

and can be written as the sum of a divergence-free vector field \mathbf{w}_d and a pure gradient of a scalar field ϕ [19]:

$$\mathbf{w} = \mathbf{w}_d + \nabla\phi \quad \text{with } \langle \nabla, \mathbf{w}_d \rangle = 0 \text{ on } \Omega \quad (2.56)$$

This implies that following relations are satisfied:

$$\langle \mathbf{w}_d, \mathbf{n} \rangle = 0 \text{ on } \partial\Omega \quad (2.57)$$

$$\langle \nabla\phi, \mathbf{n} \rangle = \langle \mathbf{w}, \mathbf{n} \rangle \text{ on } \partial\Omega \quad (2.58)$$

Taking the divergence of eq. (2.56), one gets a system of differential equations that can be summed up to:

$$\mathbf{w}_d = \mathbf{w} - \nabla\phi \quad (2.59)$$

$$\frac{\partial\phi}{\partial n} = \langle \mathbf{w}, \mathbf{n} \rangle \text{ on } \partial\Omega \quad (2.60)$$

$$\nabla\phi = \langle \nabla, \mathbf{w} \rangle \quad (2.61)$$

Considering the Navier-Stokes equations, one can associate unequivocally the different terms of the above system of differential equations to different terms of the Navier-Stokes equations (eqs. (2.1) and (2.2)) in the following way:

$$\mathbf{w}_d = \rho \frac{\partial \mathbf{u}}{\partial t} \quad (2.62)$$

$$\mathbf{w} = -\rho \nabla \cdot (\mathbf{u} \otimes \mathbf{u}) + \nabla \cdot \bar{\bar{\tau}} + \mathbf{b} \quad (2.63)$$

$$\phi = p \quad (2.64)$$

This implies from the theoretical considerations introduced here that the condition of eq. (2.55) has to be satisfied, i.e. if \mathbf{b} represents the body forces, they have to be modeled in such a way that they sum up with the other terms to zero on the boundary. This can be enforced automatically by adopting a conservative formulation for the body forces. In particular, this can be the case for the CSF-model if the formulation for representing the surface-tension force corresponds to eq. (2.40). In this way, we must have:

$$\mathbf{w} = -\rho \nabla \cdot (\mathbf{u} \otimes \mathbf{u}) + \nabla \cdot \bar{\bar{\tau}} + \nabla \cdot \bar{\bar{m}} \quad (2.65)$$

In the case of equilibrium, the velocity vector \mathbf{u} vanishes and eq. (2.56) degenerates in:

$$\nabla \cdot \bar{\bar{m}} - \nabla p = 0 \quad (2.66)$$

This equation corresponds exactly to the equilibrium condition found in [108], where an energetic approach is used. Unfortunately, the discretization of eq. (2.66) with $\bar{\bar{m}}$ defined by eq. (2.50) does not lead to perfect balance of the pressure gradient and the surface tension stresses. As a matter of consequence, an imbalance due to numerical inconsistency appears and since the equilibrium equation is no longer satisfied, the error acts as a source term to the momentum equations and a flow field develops. The so created flow field is called *parasitic currents*, because their existence is unphysical and only due to the numerical scheme used for representing

the surface-tension forces.

Since the design of the numerical scheme influences the range of applicability of the solver for flows with high surface-tension effects, a lot of effort has been spent by various authors to reduce the intensity of parasitic currents. Since their first description 1992 in [13], various cures have been proposed, which can be summarized into three main categories:

- Approaches in which a smoothing kernel is used to smooth the evaluated curvature of the free-surface. This approach is adopted in [13,50,88,106] and is equivalent to a thickening of the interface [7,91].
- Approaches in which the surface tension force is discretized using a special interpolation technique [28,40,73,78,81,104] but they all rely on the knowledge of the grid topology and the assumption that the free surface is a sharp interface so that its position must be evaluated with the help of an interface-reconstructing method [10,57,87,109]. Two ansatz can be distinguished between:
 - a special interpolation is done for the pressure gradient relatively to the estimated position of the free-surface obtained with an interface-reconstruction algorithm so that the pressure jump across the normal direction to the interface is better evaluated [73,78,81,104].
 - a procedure for which the interface is considered as sharp and is approximated in two dimensions by continuous spline curves. The coefficients of the splines are determined by a least-square method so that the volume enclosed by the free-surface equals the volume predicted by the advection of the void-fraction. It is argued that better results are achieved because of the better evaluation of the interface curvature [28]. However, this approach remains limited to two-dimensional applications.

However, the problem described by eq. (2.66) stills holds and it is necessary to find an appropriate, general discretization method that satisfies (2.66) at least at equilibrium.

The author spent a lot of effort in trying to find out a discretized formulation of expression (2.40) that would allow to represent the surface tension force as the gradient of a scalar field \tilde{p} , i.e. $\nabla \cdot \overline{\overline{\mathbf{n}}} \approx \nabla \tilde{p}$. This implies either to use a poor approximation of eq. (2.40) like in [9] or, alternatively, to solve the minimization problem:

$$\iiint_{\Omega} \|\nabla \cdot \overline{\overline{\mathbf{n}}} - \nabla \tilde{p}\| dV = \min_{\tilde{p}}! \quad (2.67)$$

Solving this problem is equivalent to satisfying the condition (see also appendix A):

$$\langle \nabla, \nabla \tilde{p} - \nabla \cdot \overline{\overline{\mathbf{n}}} \rangle = 0 \quad (2.68)$$

This implies for the above condition to hold the condition of eq. (2.69) at the boundaries of the computational domain, if a solution for eq. (2.68) has to be found:

$$\langle \nabla \cdot \overline{\overline{\mathbf{n}}}, \mathbf{n} \rangle = 0 \quad (2.69)$$

The equivalent formulation of eq. (2.68) was found to lead to no satisfactory results. In particular, the error between the gradient approximation of eq. (2.68) and the discretized values

of $\nabla \cdot \bar{m}$ did not reduce with mesh refinement, so that the gradient approximation can not be considered as a real alternate formulation of the surface tension force.

However, an interesting approach was developed by Jamet *et al.* in [41] which, based on an energy approach (see also [39, 40]), considers that the pressure gradient should be evaluated in a non-conservative manner. He proposes to replace ∇p with $\rho \nabla \mu^0$, where μ^0 can be seen as a chemical potential. This approach is equivalent to the one developed in [40], where the pressure gradient was replaced by a discretized forcing in the form $c \nabla \phi$; c representing the void fraction and ϕ the variable to solve for instead of p .

Similar ideas can be used here to solve the problem of parasitic currents. If one uses the formulation of the surface tension as the one used in *comet*, one can write for the body force term used for representing the surface-tension force:

$$\mathbf{b}_{ST} = \sigma \kappa \nabla c = \sigma \nabla(\kappa c) - \sigma c \nabla \kappa \quad (2.70)$$

Setting $p^0 = p - \sigma \kappa c$, one obtains for the equilibrium condition the new identity to hold:

$$\nabla p^0 + c \nabla(\sigma \kappa) = 0 \quad (2.71)$$

Following the idea of [41], one can seek for the pressure a solution of the form:

$$p^0 = c \mu^0 - e_f^0 \quad (2.72)$$

where:

$$\mu^0 = \frac{\partial e_f^0}{\partial c} \quad (2.73)$$

and, for the sake of generality, e_f^0 is an arbitrary function of c .

From the preceding equation, it can be deduced very easily that:

$$\frac{\partial p^0}{\partial c} = c \frac{\partial \mu^0}{\partial c} \Rightarrow \nabla p^0 = c \nabla \mu^0 \quad (2.74)$$

By replacing now ∇p^0 by its non-conservative form $c \nabla \mu^0$, the equilibrium condition is replaced by:

$$c(\nabla \mu^0 + \nabla(\sigma \kappa)) = 0 \quad (2.75)$$

The equilibrium condition implies then that the form of e_f^0 can not be chosen arbitrarily, as previously assumed, but has to satisfy the condition:

$$\frac{\partial e_f^0}{\partial c} = -\sigma \kappa \quad (2.76)$$

According to the work of Jacqmin [40], a good candidate is the function $e_f^0 = -\sigma \|\nabla c\|$.

This formulation ensures automatically that the equilibrium condition is satisfied. In the case of non-equilibrium, the pressure gradient has to be replaced in the Navier-Stokes equations by the term $c \nabla \mu^0$ and the potential form of the capillary forcing has to be used, i.e. $-\sigma c \nabla \kappa$. Unfortunately, this has some difficult numerical issues for obtaining the numerical values of

μ^0 , especially in the case when the value of the void fraction c vanishes. This problem can be overcome by setting $p^0 = p - \sigma\kappa(1 - c)$ instead of $p^0 = p - \sigma\kappa c$.

One has then to seek for μ^0 linked to p^0 by:

$$p^0 = (1 + c)\mu^0 - e_f^0 \quad (2.77)$$

with $\mu^0 = \partial e_f^0 / \partial c$.

One obtains then after derivation with respect to c :

$$\frac{\partial p^0}{\partial c} = (1 + c) \frac{\partial \mu^0}{\partial c} \Rightarrow \nabla p^0 = (1 + c) \nabla \mu^0, \quad (2.78)$$

and the modified equilibrium condition:

$$\nabla p^0 + (1 + c) \nabla(\sigma\kappa) = 0 \quad (2.79)$$

is rewritten by using $(1 + c) \nabla \mu^0$ instead of ∇p^0 as:

$$(1 + c)(\nabla \mu^0 + \nabla(\sigma\kappa)) = 0 \quad (2.80)$$

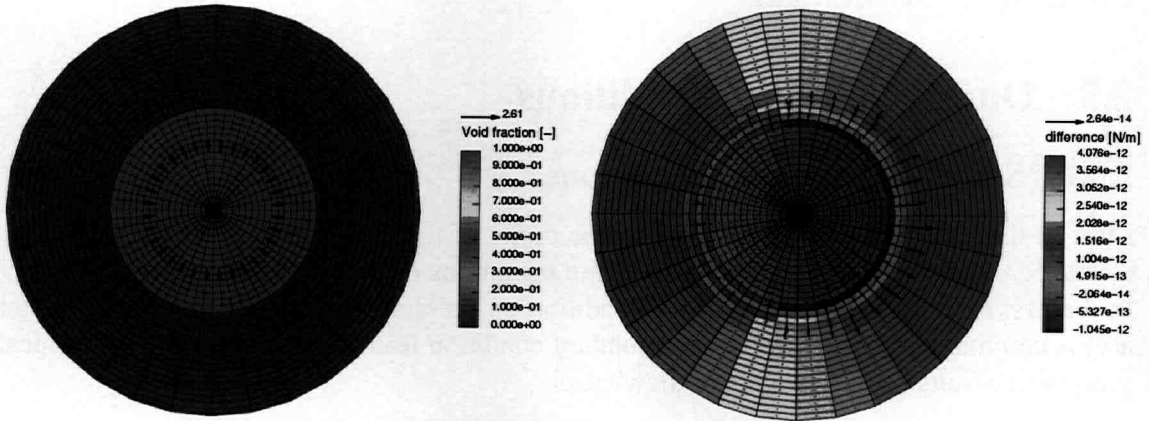


Figure 2.11: Residual velocity intensity due to the surface-tension forcing at equilibrium (right). The difference between the calculated value of μ^0 and $\sigma\kappa$ is used for the contour level. The position of the free-surface is given by the depicted void-fraction distribution on the cylindrical grid (left). The velocity field shown results from the standard model (as implemented in *comet*).

The formulation of eq. (2.80) has been implemented in a two-dimensional Navier-Stokes solver in order to demonstrate that the non-conservative approach leads to the fulfillment of the equilibrium condition, which in turn ensures that no parasitic currents can appear due to the imbalance between pressure gradient and surface-tension model. Figure 2.11 shows the results obtained on a cylindrical grid on which a droplet is modeled by setting the value of the void-fraction to 1 in all control volumes whose radius is less than 1mm. This initialization and the type of grid used ensures that the starting solution corresponds to the position of the free-surface at equilibrium. The field for μ^0 is initialized to 0 and after convergence, the difference between μ^0 and $\sigma\kappa$ is displayed, Fig. 2.11. The maximum level of the difference can be reduced to any value desired, provided that the residual tolerance of the non-linear system of equations solved

for is low enough. Here the results are shown for a residual tolerance of 10^{-14} . For comparison, Fig. 2.11 shows also the velocity field obtained when the standard model corresponding to eq. (2.54) is used. The parasitic velocity field remains located in the vicinity of the free surface and is due only to the imbalance between the pressure gradient and the discretized surface-tension force in the CSF-model approach.

2.4.4 Limitations of the CSF model

The CSF model for describing the surface tension as implemented in *comet* cannot enforce the balance of the discretized pressure gradient and the surface-tension force for the reasons explained in the preceding section. Therefore, in flows using this model of the surface-tension force, parasitic currents have to be taken into account. This limits eventually the applicability range of the solver. In practice, the parasitic current intensity U can be estimated using the expression of [13]:

$$U \sim 0.01 \frac{\sigma}{\mu} \quad [\text{m/s}] \quad (2.81)$$

For a given value of the liquid viscosity and the surface-tension coefficient, this value gives the lower bound of the flow velocity for which a simulation can be undertaken. Flows with a convective velocity of at least one order of magnitude higher than the value predicted by eq. (2.81) will not be influenced by the presence of parasitic currents. This is the case for all the simulations presented hereafter.

2.5 Outlet boundary conditions

2.5.1 Standard boundary conditions

Most of the time, boundary conditions at the outlet of the computational domain have to be estimated. The most meaningful estimates are conditions on pressure and on outlet velocities. In the first case, a Neumann boundary condition on pressure (i.e. $\partial p / \partial n = 0$ at the boundary) is commonly used. This kind of boundary condition leads most of the time to physically acceptable results but has two major drawbacks:

- the pressure at the boundary may begin to oscillate which is essentially the case when the grid is coarse at the boundary and the time step size small. The correction used to suppress oscillations on colocated grids – the so-called Rhie&Chow correction, [86] – does not damp efficiently pressure oscillations appearing under these conditions. If the pressure decreases too fast near the boundary, a back flow appears and the pressure continues to decrease. As a consequence, after a while, high velocities (both incoming and outgoing) result in cells near the outlet boundary; the solution process is then unstable and may diverge.
- the convergence rate is slow because only the derivative of the pressure at the boundary is known and not the pressure value itself. It means that there exists more than one solution for the pressure equation leading to the same value of the normal derivative at the boundary.

In the other case, setting the outlet velocities to match mass conservation allows to obtain better convergence rates. Generally, the normal derivatives of the velocity components are set to

zero and mass conservation is enforced by correcting the estimated velocities so that the mass flux leaving the computational domain matches the mass flux entering it. Vanishing normal derivatives supposes that the velocity gradients in the vicinity of the outlet boundary are small, which is hardly the case when strong vortices leave the computational domain at that boundary. Moreover, back flow from the boundary is not allowed.

A good alternative to these standard boundary conditions is the so-called *convective boundary condition*, which is presented in the following section, and for which the implementations details are given.

2.5.2 Convective boundary conditions

Convective boundary conditions are a common class of boundary conditions that are systematically employed in the simulation of turbulence, especially when vortices created by the flow are to escape the outlet boundary. The convergence rates are comparable to the standard outlet conditions and if special attention is paid to how velocities are corrected in order to ensure mass conservation, back flow can also be obtained. For the present work, it has been necessary to implement this type of boundary condition because the flows considered here often involve vortices leaving through the outlet boundary. It has been found that better convergence rate could thus be obtained during the solution procedure, saving thus a great amount of computational time compared to the pressure boundary condition used previously. Moreover, undesirable side effects resulting from pressure oscillations taking place near the outlet boundary can be avoided [42].

The velocity at the boundary is set according to the following equation [12, 25, 45, 99]:

$$\frac{\partial \mathbf{u}}{\partial t} + \bar{U} \frac{\partial \mathbf{u}}{\partial n} = 0 \quad (2.82)$$

When viscous forces are assumed to be relevant, especially in the case of a direct numerical simulation (DNS) of turbulence, the boundary condition on the velocity (eq. (2.82)) has to include a supplementary term according to eq. (2.83), [42, 75]:

$$\frac{\partial \mathbf{u}}{\partial t} + \bar{U} \frac{\partial \mathbf{u}}{\partial n} - \nu \nabla \cdot \bar{\nabla} \mathbf{u} = 0 \quad (2.83)$$

For the transport of a scalar quantity ϕ , an equivalent formulation to eq. (2.82) can be deduced:

$$\frac{\partial \phi}{\partial t} + \bar{U} \frac{\partial \phi}{\partial n} = 0 \quad (2.84)$$

The above boundary condition is consistent with the advection equation of the void fraction c , since the flow is assumed to be incompressible.

\bar{U} denotes a linearized convection velocity. There exist many choices for the convection velocity. Some authors [1, 80] set the velocity to be equal to the mean velocity over the outlet boundary:

$$\bar{U} = \frac{1}{S} \iint_S \langle \mathbf{u}, \mathbf{n} \rangle dS \quad (2.85)$$

This choice is meaningful, when there exists a mean flow direction, as can be encountered in jet or channel simulations but not when vortical structures of high intensity have to escape through

the boundary. In this case, the convection velocity is set to the velocity at the boundary cell [42]. From the author's point of view, in the case of a predominant flow direction, a good compromise between both choices for \bar{U} would consist in setting \bar{U} equal to the local time-averaged velocity at the boundary. In the case of a jet flow, it has the advantage to convect more rapidly vortices that are situated on the jet axis and less rapidly vortices at the jet edge.

Space discretization

In the following, a two-dimensional control volume of quadrilateral shape will be considered and the notations of Fig. 2.12 will be used. The locations P, B and f denote respectively the control-volume center, the middle of the boundary face and the middle of the CV-face situated opposite to the boundary face.

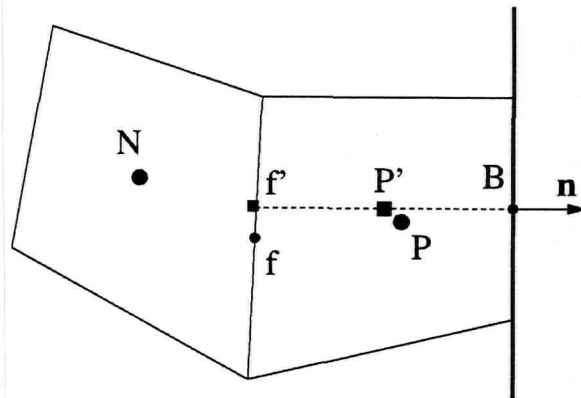


Figure 2.12: Notations used for defining locations in a control volume next to the outlet boundary, on which point B is lying.

Considering the variable ϕ , one can write up to the second order at the boundary:

$$(\nabla\phi)_B \approx (\nabla\phi)_P + (\bar{\bar{\nabla}}\nabla\phi)_P \cdot (\mathbf{r}_B - \mathbf{r}_P), \quad (2.86)$$

$$\phi_B \approx \phi_P + \langle (\nabla\phi)_P, \mathbf{r}_B - \mathbf{r}_P \rangle + \frac{1}{2!} \langle (\bar{\bar{\nabla}}\nabla\phi)_P \cdot (\mathbf{r}_B - \mathbf{r}_P), \mathbf{r}_B - \mathbf{r}_P \rangle. \quad (2.87)$$

The desired value of $\langle (\nabla\phi), \mathbf{n} \rangle_B$ is easily obtained from the two previous relations, provided that the direction given by the vector $\mathbf{r}_B - \mathbf{r}_P$ is aligned with the normal to the boundary. This is unfortunately only the case when the grid is orthogonal to the boundary. Following the idea described in [25] when the grid is non-orthogonal and assuming that the grid non-orthogonality at the boundary is not too severe, it is suitable to use the values and the gradients of ϕ at the location f' obtained by projecting the vector $\mathbf{r}_B - \mathbf{r}_f$ onto the normal vector to the boundary face (see also Fig. 2.12) as well as the location P' as the point lying midway between B and f' . Previous equations then become:

$$(\nabla\phi)_B \approx (\nabla\phi)_{P'} + (\bar{\bar{\nabla}}\nabla\phi)_{P'} \cdot (\mathbf{r}_B - \mathbf{r}_{P'}), \quad (2.88)$$

$$\phi_B \approx \phi_{P'} + \langle (\nabla\phi)_{P'}, \mathbf{r}_B - \mathbf{r}_{P'} \rangle + \frac{1}{2!} \langle (\bar{\bar{\nabla}}\nabla\phi)_{P'} \cdot (\mathbf{r}_B - \mathbf{r}_{P'}), \mathbf{r}_B - \mathbf{r}_{P'} \rangle. \quad (2.89)$$

Replacing from eq. (2.88) the term $(\overline{\nabla \nabla \phi})_{P'} \cdot (\mathbf{r}_B - \mathbf{r}_{P'})$ into eq. (2.89) and arguing that the vector $\mathbf{r}_B - \mathbf{r}_{P'}$ is directed normal to the boundary face, it can be deduced after some rewriting:

$$\langle (\nabla \phi), \mathbf{n} \rangle_B \|\mathbf{r}_B - \mathbf{r}_{P'}\| \approx 2(\phi_{P'} - \phi_B) + \langle (\nabla \phi)_{P'}, \mathbf{r}_B - \mathbf{r}_{P'} \rangle \quad (2.90)$$

Dividing above equation by $\|\mathbf{r}_B - \mathbf{r}_{P'}\| = \frac{1}{2}\|\mathbf{r}_B - \mathbf{r}_{f'}\|$, one obtains:

$$\langle (\nabla \phi), \mathbf{n} \rangle_B \approx \frac{4(\phi_{P'} - \phi_B)}{\|\mathbf{r}_B - \mathbf{r}_{f'}\|} + \langle (\nabla \phi), \mathbf{n} \rangle_{P'} \quad (2.91)$$

Using central differences, the gradient of ϕ at the location P' can be deduced with second-order accuracy from the following equation:

$$\langle (\nabla \phi), \mathbf{n} \rangle_{P'} \approx \frac{\phi_B - \phi_{f'}}{\|\mathbf{r}_B - \mathbf{r}_{f'}\|} \quad (2.92)$$

One can then write⁶ for $\partial\phi/\partial n$:

$$\left(\frac{\partial\phi}{\partial n}\right)_B \stackrel{def.}{=} \langle \nabla \phi, \mathbf{n} \rangle_B \approx \frac{3\phi_B - 4\phi_{P'} + \phi_{f'}}{\|\mathbf{r}_B - \mathbf{r}_{f'}\|} \quad (2.93)$$

The values of ϕ at the locations P' and f' can be evaluated easily with second-order accuracy with:

$$\phi_{P'} \approx \phi_P + \langle (\nabla \phi)_P, \mathbf{r}_{P'} - \mathbf{r}_P \rangle, \quad (2.94)$$

$$\phi_{f'} \approx \phi_f + \langle (\nabla \phi)_f, \mathbf{r}_{f'} - \mathbf{r}_f \rangle. \quad (2.95)$$

The gradient of ϕ at the location f can be obtained with usual linear interpolation practice between cell center locations P and N . Finally, one obtains:

$$\left(\frac{\partial\phi}{\partial n}\right)_B \approx \frac{3\phi_B - 4\phi_P + \phi_f}{\langle \mathbf{r}_B - \mathbf{r}_f, \mathbf{n} \rangle} + \frac{-4 \langle (\nabla \phi)_P, \mathbf{r}_{P'} - \mathbf{r}_P \rangle + \langle (\nabla \phi)_f, \mathbf{r}_{f'} - \mathbf{r}_f \rangle}{\langle \mathbf{r}_B - \mathbf{r}_f, \mathbf{n} \rangle} \quad (2.96)$$

Time discretization

Concerning the time discretization, it has been chosen to use a three-time level fully-implicit differencing scheme [25, 96]. Although the discretization error for this scheme is higher than for the Crank-Nicholson scheme, this scheme is also of second-order and has been found to be consistent with the numerical model of the employed Navier-Stokes solver *comet*. Using a fixed time step Δt , one obtains easily the following expression for the discrete time derivative:

$$\left(\frac{\partial\phi}{\partial t}\right)_{t=t_n} \approx \frac{3\phi^n - 4\phi^{n-1} + \phi^{n-2}}{2\Delta t}, \quad (2.97)$$

where the superscripts n , $n - 1$ and $n - 2$ denote respectively the present, the previous and the second previous time-level.

⁶Expression (2.93) is equivalent to the well-known linear upwind differencing scheme [25] used in finite-difference methods.

Discretized boundary condition

Combining eqs. (2.96) and (2.97) into (2.82), one obtains the general expression for setting the value of ϕ at the boundary with a second order discretization error in time and space:

$$\phi_B^n \approx \left[\frac{4\phi_P^n - \phi_f^n + 4 \langle (\nabla \phi)_P^n, \mathbf{r}_{P'} - \mathbf{r}_P \rangle - \langle (\nabla \phi)_f^n, \mathbf{r}_{f'} - \mathbf{r}_f \rangle}{\langle \mathbf{r}_B - \mathbf{r}_f, \mathbf{n} \rangle} + \frac{2\phi_B^{n-1} - \phi_B^{n-2}}{\Delta t} \right] \frac{1}{\frac{3}{2\Delta t} + \frac{3\bar{U}}{\langle \mathbf{r}_B - \mathbf{r}_f, \mathbf{n} \rangle}} \quad (2.98)$$

In the case that the variable ϕ corresponds to the void fraction c , it is important to ensure that the boundary value for c at the location B remains bounded, hence $0 \leq c_B \leq 1$. This is achieved by limiting the predicted value of c from the previous equation between 0 and 1:

$$c_B = \min(1, \max(0, c_B)) \quad (2.99)$$

If the variable ϕ corresponds to one of the velocity components, an additional term has to be included in order to take viscous effects into account according to the work of [42, 75]. By denoting u_i one of the Cartesian velocity components, the boundary condition of eq. (2.83) can be written:

$$\frac{\partial u_i}{\partial t} + \bar{U} \frac{\partial u_i}{\partial n} - \nu \langle \nabla, \nabla u_i \rangle = 0 \quad (2.100)$$

The diffusion term $\nu \langle \nabla, \nabla u_i \rangle$ is discretized explicetly in the manner described in [25] and extrapolated from the interior domain to the boundary; it is corrected after each outer iteration during the solving process. By denoting u_i^m the predicted value of u_i at the m -th outer iteration, the discretized boundary condition for the velocity component becomes:

$$(u_i^m)_B \approx \left[\frac{4(u_i^m)_P - (u_i^m)_f + 4 \langle (\nabla u_i)_P^{m-1}, \mathbf{r}_{P'} - \mathbf{r}_P \rangle - \langle (\nabla u_i)_f^{m-1}, \mathbf{r}_{f'} - \mathbf{r}_f \rangle}{\langle \mathbf{r}_B - \mathbf{r}_f, \mathbf{n} \rangle} + \frac{2(u_i^{m-1})_B - (u_i^{m-2})_B}{\Delta t} + \nu \langle (\nabla, \nabla u_i)_B^{m-1} \rangle \right] \frac{1}{\frac{3}{2\Delta t} + \frac{3\bar{U}}{\langle \mathbf{r}_B - \mathbf{r}_f, \mathbf{n} \rangle}} \quad (2.101)$$

This expression has been used in the present work and implemented via the user defined sub-routines for boundary conditions into the *comet* solver.

Mass conservation

Unfortunately, the velocity profile predicted for the boundary by the convective boundary condition may not ensure mass conservation. As described in [99], the predicted velocity has to be corrected in order to match mass fluxes between inflow and outflow. We denote by \mathbf{u}_B^* the velocity vector at the boundary obtained after evaluating eq. (2.101), which may not satisfy mass conservation. The corresponding mass flux delivered by this velocity profile at the boundary is denoted by Q^* , whereas the correct mass flux is denoted by \bar{Q} . We define then the mass flux defect by $\Delta \bar{Q} = \bar{Q} - Q^*$. Then, it is straightforward to show that the following correction gives a velocity profile at the boundary warranties mass conservation:

$$\mathbf{u}_B = \mathbf{u}_B^* + \frac{\Delta \bar{Q}}{Q^*} \frac{\langle \mathbf{u}_B^*, \mathbf{S}_B \rangle}{\langle \mathbf{S}_B, \mathbf{S}_B \rangle} \mathbf{S}_B, \quad (2.102)$$

where \mathbf{S}_B is the surface vector associated to the boundary face at location B . This type of correction algorithm allows back-flow to occur at the boundary (see also Fig. 2.14). Nevertheless, if the mass flow entering the computational domain vanishes (i.e. $\bar{Q} = 0$), the velocity component normal to the boundary after correction vanishes also. This may not be desired, especially when back-flow is expected. The problem may be tackled by defining Q_+^* the mass flow leaving the outlet boundary and Q_-^* the mass flow entering the boundary. In the case of incompressible media, we can then define:

$$Q_+^* = \sum_{f_B} \rho_B \langle \mathbf{u}_B^*, \mathbf{S}_B \rangle; \quad \langle \mathbf{u}_B^*, \mathbf{S}_B \rangle \geq 0 \quad (2.103)$$

$$Q_-^* = \sum_{f_B} \rho_B \langle \mathbf{u}_B^*, \mathbf{S}_B \rangle; \quad \langle \mathbf{u}_B^*, \mathbf{S}_B \rangle < 0 \quad (2.104)$$

f_B corresponds to every boundary face belonging to the outlet boundary, on which the convective boundary condition has been set. Then the modified correction algorithm allows to ensure mass conservation as well as to avoid obtaining vanishing velocity component normal to the boundary in case of vanishing mass flux into the computational domain:

$$\mathbf{u}_B = \mathbf{u}_B^* + \frac{\Delta \bar{Q}}{Q_+^* - Q_-^*} \frac{\langle \mathbf{u}_B^*, \mathbf{S}_B \rangle}{\langle \mathbf{S}_B, \mathbf{S}_B \rangle} \mathbf{S}_B; \quad \langle \mathbf{u}_B^*, \mathbf{S}_B \rangle \geq 0, \quad (2.105)$$

$$\mathbf{u}_B = \mathbf{u}_B^* - \frac{\Delta \bar{Q}}{Q_+^* - Q_-^*} \frac{\langle \mathbf{u}_B^*, \mathbf{S}_B \rangle}{\langle \mathbf{S}_B, \mathbf{S}_B \rangle} \mathbf{S}_B; \quad \langle \mathbf{u}_B^*, \mathbf{S}_B \rangle < 0. \quad (2.106)$$

This correction has been implemented into the solver *comet* and shown to lead to improved results compared to the standard boundary condition at outlet. Note that the convective boundary condition developed here is applicable to an arbitrary polyhedral, three-dimensional grid.

Application examples

In practical applications, one usually has to use long solution domains in order to avoid effects of errors introduced at the outlet boundary on flow regions of interest. However, in many cases, this is not practical besides the fact that larger solution domains require larger computing effort. It was therefore of interest to see whether one can use shorter solution domains by employing the convective boundary condition at outlet in flows that contain vortices leaving through the outlet boundary.

Among all test calculations performed for validating the convective boundary condition according to the theoretical developments of the preceding sections, interesting benchmarks are the cases 2D-2 and 2D-3 of [36]. They correspond to the unsteady flow developing around a circular cylinder in a channel (corresponding to Fig. 2.13). The velocity profile at inlet is given by eq. (2.107) in the case 2D-2 and is modulated according to eq. (2.108) in the case 2D-3. In the case 2D-2, the Reynolds number based on the cylinder diameter and the mean inlet velocity is set to 100. The resulting value for U_m is then set to the same value in both cases 2D-2 and 2D-3, i.e. 1.5 m/s, and the velocity profiles are:

$$U(y, t) = 4U_m \frac{y(H-y)}{H^2}, \quad (2.107)$$

$$U(y, t) = 4U_m \frac{y(H-y)}{H^2} \sin(\pi t/8) \quad 0 \leq t \leq 8s. \quad (2.108)$$

Note that the inlet velocity is steady in the case 2D-2, but the flow is unsteady in the cylinder wake due to vortex shedding.

In the case 2D-3, the inlet velocity varies within the given time interval of 8 s according to a half-sinus wave. This implies that the inlet velocity vanishes towards the end of the time-dependent simulation. If the standard outlet boundary condition is used for which the inlet mass flux is used to scale the velocity normal to the boundary – so that the mass flow leaving the computational domain through this boundary matches the incoming mass flow –, the velocity normal to the boundary will also vanish. With the corrective procedure on the mass flux proposed previously, it is still possible to obtain vortices leaving the boundary, even if the mass flow entering the computational domain is almost zero, Fig. 2.14. In this case, the convective velocity \bar{U} was set to the velocity of the cell next to the boundary face, since the velocity \bar{U} obtained with eq.(2.85) would have vanished too and hence would have hindered any vortex from leaving the domain at the outlet boundary.

For the case 2D-2, the contours of the time-averaged pressure obtained with the standard outlet boundary condition – corresponding to a Neumann boundary condition i.e. for a variable ϕ , $\partial\phi/\partial n = 0$ – and with the implemented boundary condition described above have been calculated on a shortened computational domain for which the outlet boundary has been put 6 cylinder diameters behind the center of the cylinder. The results are presented for the convective boundary condition and for the standard outlet boundary condition in Fig. 2.15 and 2.16, respectively. The results are compared with the reference solution obtained on the complete computational domain represented in Fig. 2.13. The grid is identical in the overlapping region for both sizes of the computational domain. For all the simulations, time-averaged values have been obtained after the L_2 -norm of the deviation from the average value had reached the threshold value of 1%. It can be deduced from the comparison of Fig. 2.15 and 2.16 that the convective outlet boundary condition has less influence on the mean pressure distribution within the computational domain than the standard outlet boundary condition. Significant differences are observed in the vicinity of the outlet boundary only whereas for the standard outlet condition, the boundary condition influences the mean pressure distribution in the whole computational domain. From the comparison of the instantaneous pressure contours obtained for the case 2D-2 on the shortened with the convective boundary condition (Fig. 2.17) and the complete (Fig. 2.18) computational domains 8s after the start of the computation, it can be observed that the low-level pressure region near the boundary corresponds to the same low pressure region on the complete computational domain. This indicates that the vortices created by the flow are correctly convected outside the computational domain with the convective boundary condition. The pressure levels of Fig. 2.19 show the superiority of the convective boundary condition (Fig. 2.17) compared to the standard outlet boundary condition. In the case of the outlet boundary, pressure levels are different from those of the reference solution of Fig. 2.18, the region of the solution domain near to the outlet boundary is strongly influenced by it, the vortex detachment takes place for the same time at a different locations, which suggests that the vortex shedding frequency is not predicted correctly. This assumption is confirmed by the Strouhal numbers obtained with the methods on the shortened computational domain (see Tab. 2.1). For the convective boundary condition, the Strouhal number obtained ($St = \frac{fD}{U}$) is identical

	2D-2 reference domain	2D-2 short domain convective BC	2D-2 short domain outlet BC
St	0.30037	0.30037	0.29876
Δ St	-	0.00%	-0.536%

Table 2.1: Comparison of the Strouhal numbers obtained on various computational domains for case 2D-2 using two types of boundary conditions for velocities: convective and standard outlet. The end of the short domain is placed 6 diameter length behind the cylinder center.

to the one obtained on the complete computational domain, while using the standard boundary condition, an appreciable discrepancy is noticeable.

A convective boundary condition for the pressure can also be derived from eq. (2.84) and implemented to replace the standard pressure boundary condition used in *comet*. This boundary condition is identical to the convective boundary condition used in [75], excepted that the viscous term is neglected, hence:

$$\frac{\partial p}{\partial t} + \bar{U} \frac{\partial p}{\partial n} = 0 \quad (2.109)$$

The above boundary condition has been implemented and applied to the flow around a square cylinder. Geometry as well as boundary conditions applied are to be taken from Fig. 2.20. For the inlet boundary condition, the block profile with a constant velocity U_∞ sets the reference velocity used for the convective boundary condition of eq. (2.109). As for the preceding benchmark cases, the time-averaged values of the pressure were calculated on the complete computational domain for a Reynolds number of 200, defined by the inlet velocity and the square edge A as a reference length. Again, the calculation of the time-averaged values was assumed to be converged when the L_2 -norm of the deviation had reached the threshold value of 1%. The reference data so collected could then be used to compare the time-averaged values of the pressure obtained on a truncated mesh extending $10A$ behind the cylinder for two types of boundary conditions: the standard outlet boundary condition – a boundary condition of Neumann type – and the here implemented convective boundary condition on pressure.

Figures 2.21 and 2.22 show the distribution of the time-averaged pressure for the shortened computational domain for the Neumann and for the convective boundary condition. The convective boundary condition shows better agreement with the reference solution in the vicinity of the cylinder. This is confirmed by Fig. 2.23 in which the values of the time-averaged pressure along the centerline obtained with the convective boundary condition are closer to the reference solution than when the standard boundary condition is used. These conclusions are very similar to the ones in [99], where the effects of Neumann boundary conditions and convective boundary condition were studied on the flow around a square at incidence at a low Reynolds number between 100 and 200.

For the chosen Reynolds number, a vortex street develops downstream of the cylinder. The vortex shedding frequency obtained on the reference computational domain is compared to the values obtained for the convective and standard outlet boundary conditions on a shorter domain in Tab. 2.2. The Strouhal number, $St = \frac{fA}{U_\infty}$, obtained using the convective boundary condition

shows a better agreement with the reference value than for the outlet boundary condition. The results of these two test-simulations show clearly that the convective boundary condition has less influence on the flow field in the upstream region than the conventional outlet boundary condition. It was therefore used in all simulations of unsteady vortical flow.

<i>two-dimensional flow around a square cylinder</i>				
	reference [99, 100]	reference domain	short domain convective BC	short domain Neumann BC
St	0.150~0.160	0.1515	0.1504	0.1569
ΔSt	-	-	-0.726%	+3.56%

Table 2.2: Comparison of the Strouhal numbers obtained on various computational domains for the flow around a square cylinder using two types of boundary conditions for pressure: convective and of Neumann type. The end of the short domain is placed 10 square-edge length behind the cylinder center.

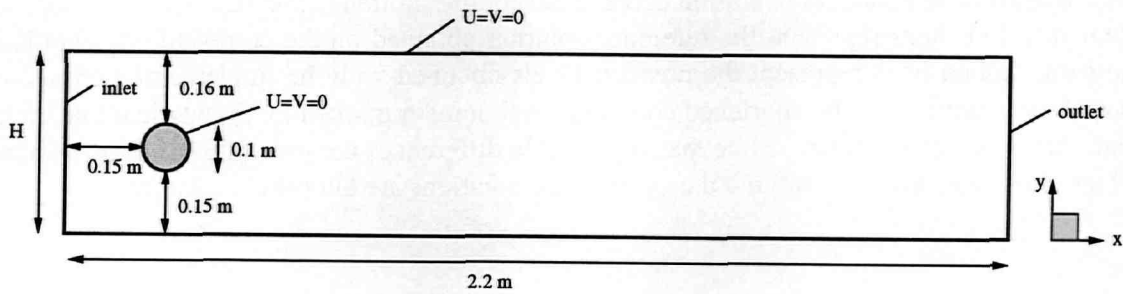


Figure 2.13: Geometry of benchmark cases 2D-2 and 2D-3 with boundary conditions.

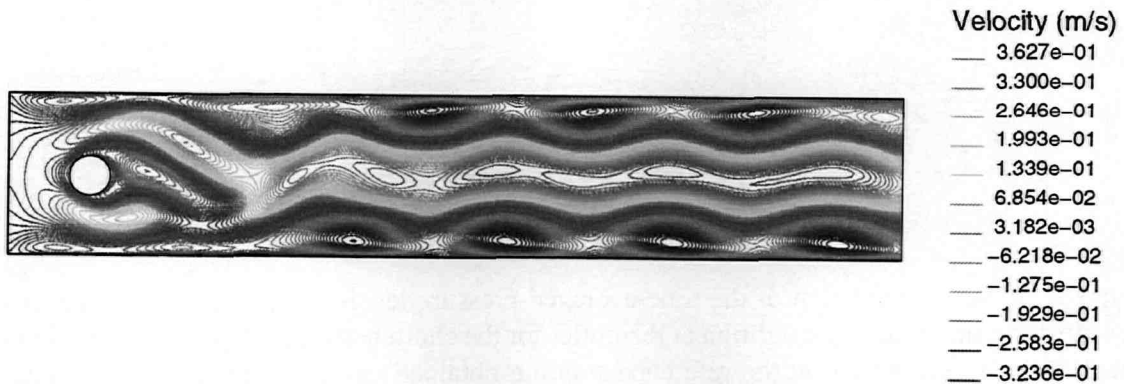


Figure 2.14: Contours of the velocity component u 7.9 s after the start of the simulation for the case 2D-3. At the outlet on the right-hand side of the computational domain, zones of negative velocity are observed and indicate the presence of back flow at the boundary.

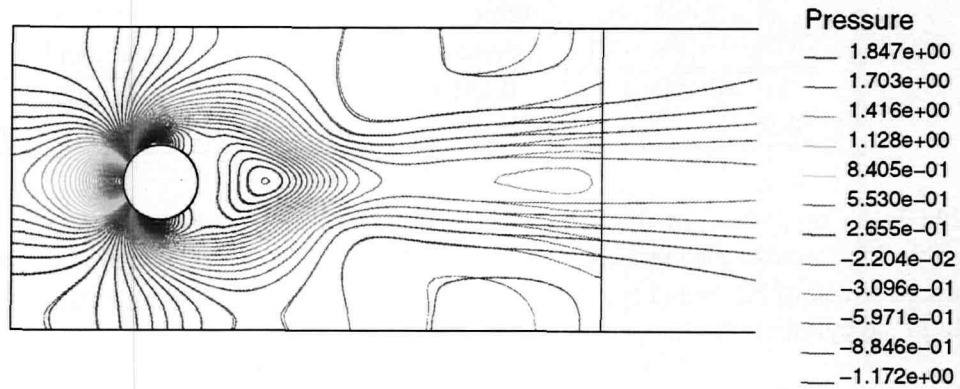


Figure 2.15: Superimposition of the time-averaged pressure levels for the case 2D-2 obtained with a convective boundary condition at the outlet for the shortened and full size computational domains. Full lines represent the reference solution obtained on the complete computational domain; dashed lines represent the pressure levels obtained with the implemented convective boundary condition on the shortened computational domain marked by the vertical line on the right-hand side of the figure. Note that appreciable differences are only present near boundary of the shortened domain – around the cylinder the solutions are almost coincident.

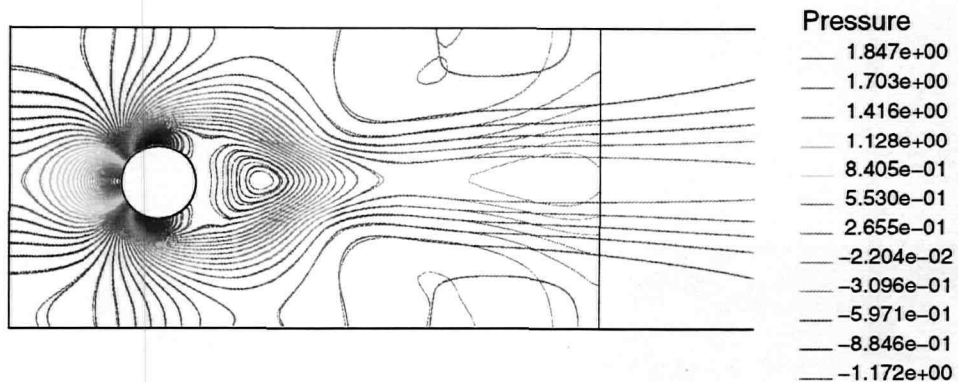


Figure 2.16: Superimposition of the time-averaged pressure levels for the case 2D-2 obtained with the standard boundary condition at the outlet for the shortened and full size computational domains. Full lines represent the reference solution obtained on the complete computational domain; dashed lines represent the pressure levels obtained with the standard outlet boundary condition on the shortened computational domain marked by the vertical line on the right-hand side of the figure. Note that appreciable differences are present even in the front of the cylinder and all around it.

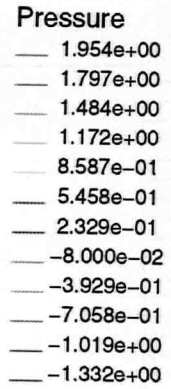
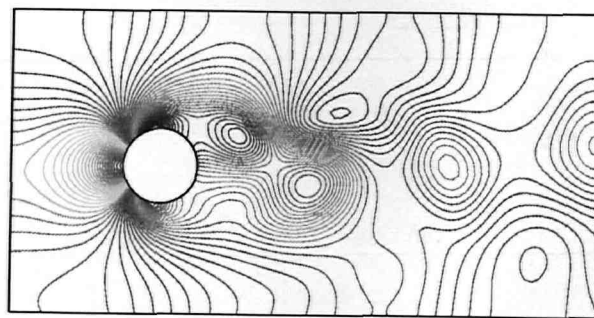


Figure 2.17: Pressure levels for the case 2D-2 on the shortened domain 8 s after the start of the simulation with convective outlet boundary condition.

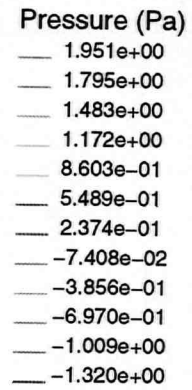
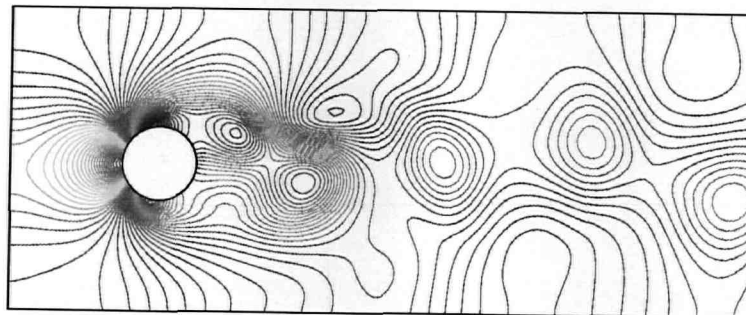


Figure 2.18: Pressure levels for the case 2D-2 on the reference domain 8 s after the start of the simulation.

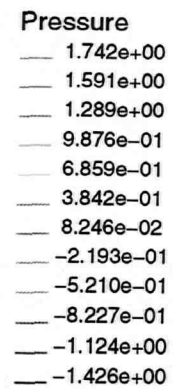
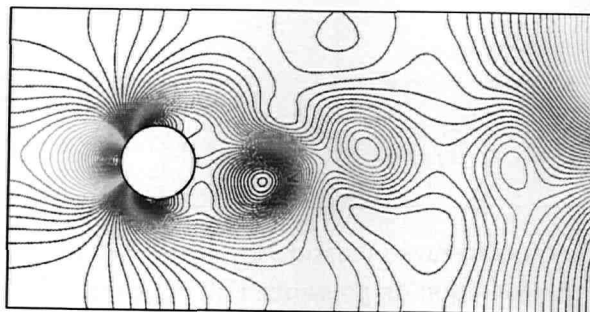


Figure 2.19: Pressure levels for the case 2D-2 on the shortened domain 8 s after the start of the simulation with standard outlet boundary condition.

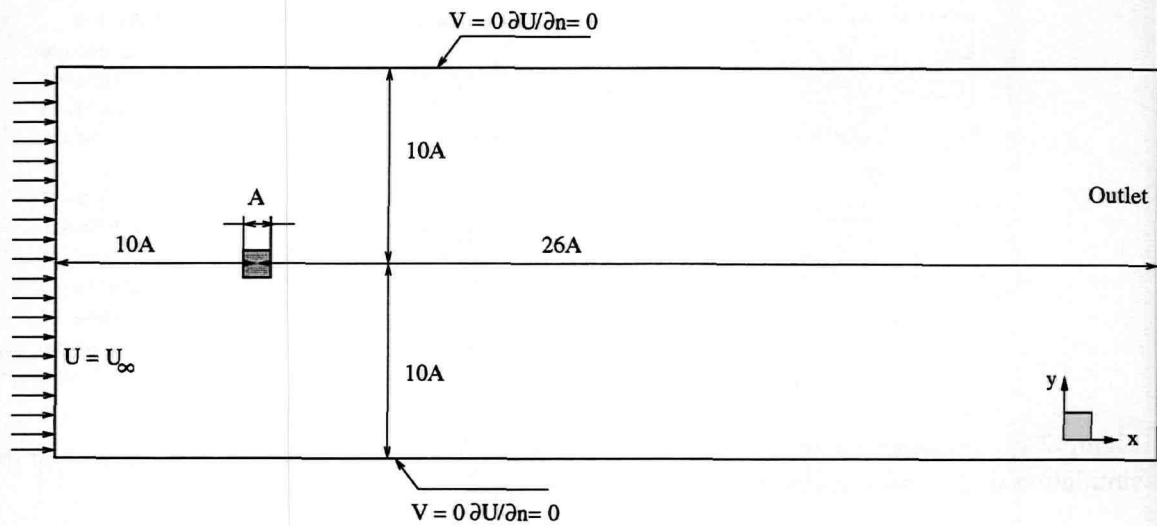


Figure 2.20: Geometry and boundary conditions used for the simulation of the flow around a square cylinder.

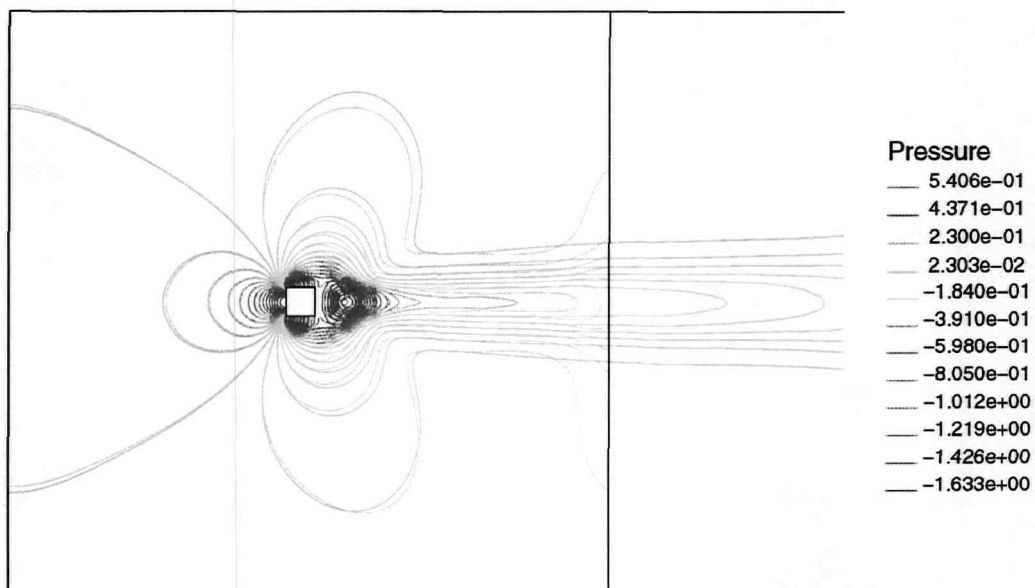


Figure 2.21: Superimposition of the time-averaged pressure levels for the flow around a square cylinder with the Neumann boundary condition on pressure. Full lines represent the reference solution obtained on the complete computational domain; dashed lines represent the pressure levels obtained with the outlet boundary condition of Neumann type on the shortened computational domain marked by the vertical line on the right side of the figure.

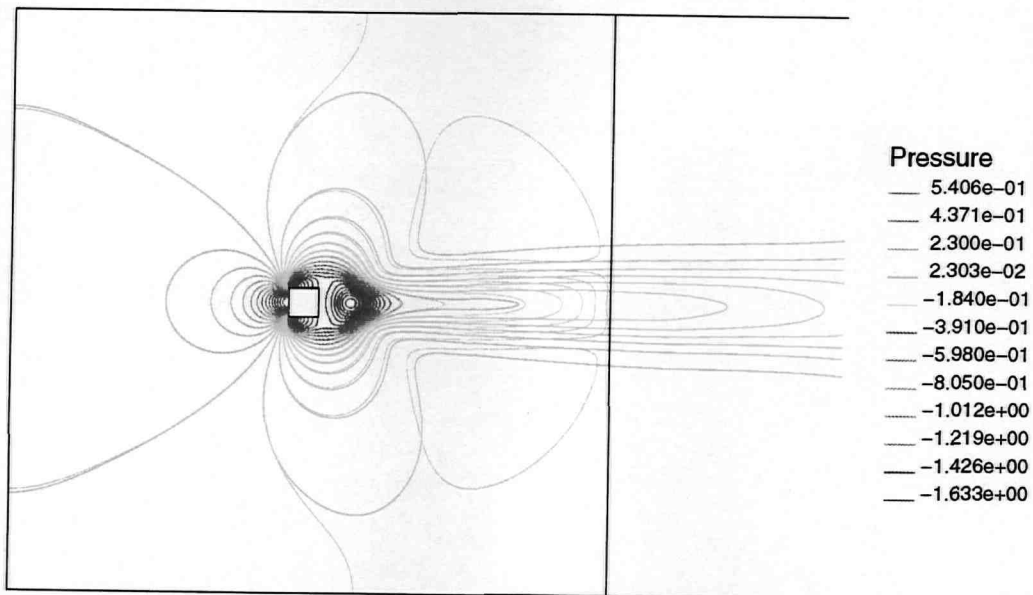


Figure 2.22: Superimposition of the time-averaged pressure levels for the flow around a square cylinder with a convective boundary condition on pressure. Full lines represent the reference solution obtained on the complete computational domain; dashed lines represent the pressure levels obtained with the convective boundary condition on the shortened computational domain marked by the vertical line on the right side of the figure

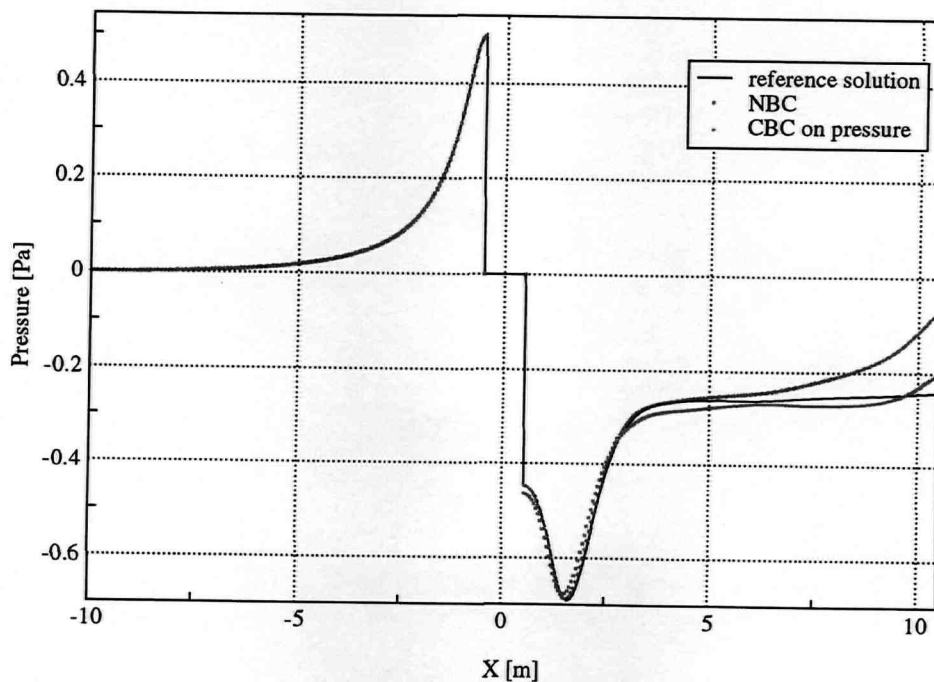


Figure 2.23: Time-averaged values of the pressure versus the position along the centerline of the computational domain. The continuous line represents the reference solution obtained on the complete computational domain, while symbols represent the solutions obtained on the truncated computational domain for the Neumann (NBC) and convective (CBC) boundary conditions on pressure.

Chapter 3

Simulations of the Primary Breakup of Laminar Jets

This chapter deals with the simulation of the primary breakup of liquids jets and its purpose is to show that the numerical method described in the preceding section of this thesis is able to reproduce correctly the breakup behavior of laminar liquid jets for which surface-tension is responsible for the generation of instabilities at the jet free-surface. Here, selected classes of problems at different frequency ranges are presented to validate the numerical model with experimental – when available – and theoretical data: Rayleigh breakup, medium-ranged actuation of a liquid sheet, sinusoidally forced breakup of a liquid jet at high excitation frequency. Finally, an example is shown for which the actuation arises from a naturally unsteady flow pattern in the gaseous phase.

3.1 Rayleigh breakup

Lord Rayleigh was the first to discover by using stability analysis that round laminar jets are unstable if the wavelength of the disturbance applied to the jet free surface exceeds a threshold value [84]. He showed that, due to the surface tension, the waves at the free-surface of the jet, provided that their wavelength λ is greater than the jet circumference, undergo an exponential growth in time and space. The growth rate is related to the disturbance wavelength and reaches a maximum in the vicinity of the normalized wavenumber $k^* = \frac{\pi D}{\lambda} = 0.697$, where D denotes the initial diameter of the undisturbed jet [16]. This phenomenon is very well defined and is observed when the jet flow is laminar at low Weber-numbers ($We < 3.15$ according to [54]). Because surface tension tends to change the shape of the jet free surface in order to achieve a surface with minimal energy, the jet breaks up after a given length, depending on both initial amplitude of the disturbance and the growth rate; eventually, droplets are formed. The droplets obtained are separated into two categories: the *main* droplets, whose diameter can be larger than the jet diameter, and smaller ones, the so called *satellite* droplets (because they are found between two consecutive main droplets), which have a diameter smaller than the jet diameter.

The Rayleigh breakup of a round laminar jet constitutes a challenge for a numerical method to reproduce accurately the droplets formation under the action of surface tension. There has been numerous experimental work on this topic since Lord Rayleigh's discovery in order to study parameters (like fluid viscosity) which may influence jet-breakup characteristics like breakup

length and droplet sizes [23, 29, 33, 38, 74, 90, 101]. This has been complemented by theoretical investigations on the base of non-linear stability analysis [16, 44, 51, 54, 62, 63, 85, 89]. The Rayleigh breakup of a round laminar jet is thus a very well documented flow regime for which surface tension plays a dominant role. This is the reason why this particular kind of flow regime was chosen to study the capability of the numerical method to reproduce correctly the jet breakup and the generation of droplets. To the best knowledge of the author, only few numerical simulations dealing with jet breakup in the Rayleigh flow regime have been reported so far [16, 26, 68, 69]; the results presented here are among the first simulations of this flow with a numerical method based on the Navier-Stokes equations.

For the simulations presented hereafter, the jet diameter has been set to 2.59 mm and a small velocity disturbance of $\epsilon_0=1\%$ of the mean velocity $U_m=2.126 \text{ ms}^{-1}$ of sinusoidal shape at a forcing frequency f_0 has been applied at the inlet of the computational domain according to the following relation (in a cylindrical coordinate system aligned with the jet axis):

$$U_r(z = 0, r, t) = U_m\{1 + \epsilon_0 \sin(2\pi f_0 t)\} \quad (3.1)$$

In all simulations, a two-dimensional axisymmetric numerical grid corresponding to a slice of one degree angle and the *interface-capturing* method based on the HRIC discretization scheme have been used. Depending on the the wavelength of the disturbance, the jet breakup may occur at a longer or shorter distance from the inlet of the computational domain. Also, the size of the droplets created during breakup may exceed by twice or more the jet diameter. Accordingly, the grid used for the simulations has to be adapted using local refinement, so that both jet breakup and the formed droplets can be captured accurately. The grid extends $20D$ – where D is the diameter of the undisturbed jet – in radial direction and from $100D$ to $200D$ in streamwise direction, depending on the wavelength of the imposed disturbance. Thus, the number of control volumes employed for the simulations varies from approx. 105,000 CVs (for the disturbance wavelength corresponding to $k^*=0.683$) to approx. 200,000 (for the disturbance wavelength corresponding to $k^*=0.250$). The time step was set to a fraction of the excitation period; typically 200 hundred time steps per period have been used. The excitation period can be deduced from the following relation, given the wavelength λ and the velocity of the undisturbed jet U_m :

$$\lambda = \frac{U_m}{f_0} \quad (3.2)$$

Given the normalized wavenumber k^{*1} , it is possible to provide the excitation frequency which has been varied between 65 Hz (corresponding to $k^*=0.250$) and 180 Hz (corresponding to $k^*=0.683$). The physical properties used in the simulations are summarized in table 3.1 and correspond to the fluid properties used in the experiments of [89].

σ [Nm^{-1}]	ρ [kg m^{-3}]	μ [$\text{kg m}^{-1}\text{s}^{-1}$]
0.056	1120	0.004

Table 3.1: Physical properties used for the simulations of the Rayleigh breakup.

¹Using eq. (3.2), k^* rewrites to $k^* = \frac{\pi D f_0}{U_m}$. Thus, k^* is equivalent to the Strouhal number of the imposed excitation.

Following Rutland & Jameson [89], it is possible to define a dimensionless number $J = \frac{\sigma D}{2\rho\nu^2}$ related to the Ohnesorge number, which is a measure of the surface tension effects relative to the viscous forces. Thus, for $J \gg 1$, the effects of viscosity are negligible compared to surface-tension effects. In our case and in order to compare the obtained drop sizes from the computations with the experimental data from the literature, the number J has – with the physical properties of table 3.1 – a value of 4,600. This has the advantage to keep the jet-breakup length small, resulting in a smaller computational domain and hence less computational effort; smaller values of J would have resulted in a longer breakup length. since viscosity stabilizes the jet deformations by damping oscillations at the jet free-surface [63].

Figure 3.1 shows predicted shapes of the jet free-surface for four k^* values. This figure shows a remarkable similarity with photographs obtained in experiments [16], as shown in Fig. 3.2. As k^* is increased, the break-up length reduces, but the number of wavelengths until breakup increases. Also, the sizes of the satellite and main droplets correlate very well with the theoretical and experimental values, Fig. 3.3. For convenience, it is useful to normalize the droplet diameter with the undisturbed jet diameter. Thus, it can be seen from Fig. 3.3 that the droplet size so obtained can be larger than the initial jet diameter. Furthermore, as pointed out in [29], the detached droplets in both experiments and calculations do not at once retain a spherical form and execute series of oscillations, being alternatively compressed and elongated in the direction of the jet axis. This can be clearly seen from Figs.3.2 and 3.1. Besides, the phenomenon described in [16], in which the forward merging of the satellite drop with the main drop following it takes place, could be successfully reproduced in the numerical simulations.

The results obtained for this test case demonstrate that the numerical method presented in the preceding chapter is capable of correctly predicting jet-breakup phenomena; this includes the deformations of the jet free-surface as well as droplet creation and merging as they occur in the Rayleigh breakup. This numerical method has been then applied to a range of more complex problems where numerical simulations can serve as a supplement to experiments in trying to better understand the physics behind jet breakup phenomena.

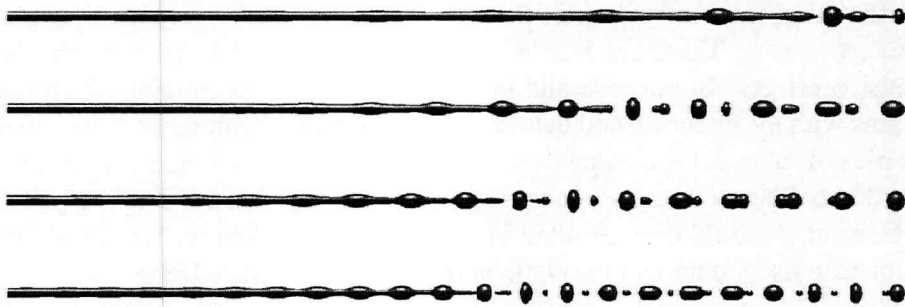


Figure 3.1: Computed free-surface deformation for the Rayleigh breakup mode for various values of the normalized wave number k^* ; from top to bottom: $k^*=0.250, 0.430, 0.533, 0.683$. Flow is from left to right.

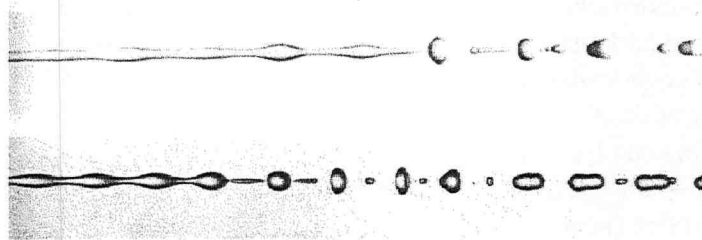


Figure 3.2: Free-surface deformations as observed in the experiments for the normalized wave numbers $k^*=0.250$ (top) and $k^*=0.683$. The experimental photographs have been taken from [24].

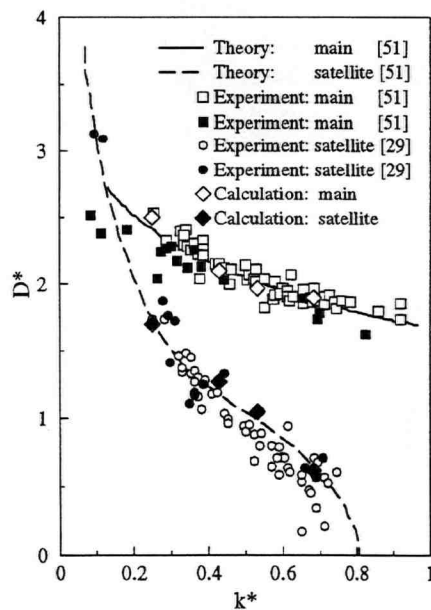


Figure 3.3: Drop sizes in Rayleigh break-up: comparison between calculated values and experimental data; k^* is the normalized wave number, $D^* = D_{\text{drop}}/D_{\text{jet}}$ is the normalized droplet radius.

3.2 Medium-ranged actuation frequencies

The purpose of the simulation undertaken in this section is to demonstrate that the computational method is also able to reproduce free-surface deformations, not only for low values of the excitation frequency (case of the Rayleigh breakup, see also the preceding section), but also for higher excitation-frequency values, say in the range of several kHz.

The present investigation is based on references [46, 70], in which a simplified model for the three-dimensional breakup analysis of a thin liquid sheet is presented. The model assumes that the liquid sheet is injected from a nozzle into a gas of negligible density with the undisturbed velocity u_0 and the thickness a_0 . Moreover, in this model, the liquid is assumed to be inviscid, incompressible and free of gravity forces. Two forms of free-surface deformation may then exist and are called respectively sinuous and dilational mode. In the sinuous mode, the lower and upper free-surfaces of the liquid sheet are in phase and antisymmetric relative to the plane of symmetry of the undisturbed liquid sheet. In the dilational mode, the free-surface deformations are symmetric and out of phase (see also Fig. 3.4).

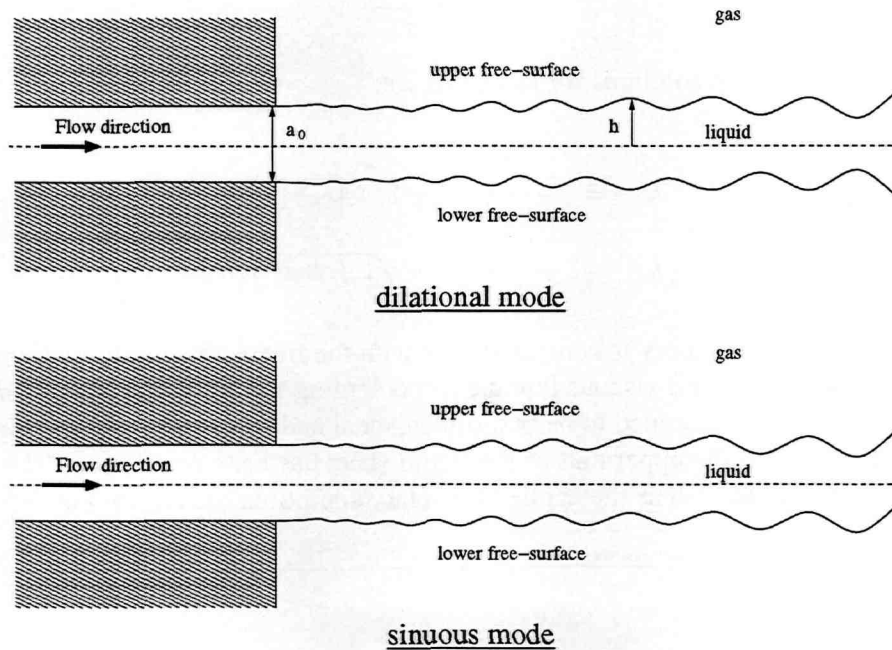


Figure 3.4: Dilational and sinuous modes as they occur during the breakup of a thin liquid sheet.

Dilational mode

The linear wave theory of [46, 70] developed under the assumption that the liquid sheet is inviscid, incompressible and is ejected into a gas of negligible density, states that the free-surface deformations obey the following equation:

$$h/a_0 = 1 + \frac{k_2 k_3 u'}{(k_3 - k_2)\omega} [\sin(k_3 x - \omega t) - \sin(k_2 x - \omega t)]. \quad (3.3)$$

Here, a_0 is the undisturbed sheet thickness, h represents the sheet thickness relative to the plane of symmetry of the undisturbed liquid sheet and u' is the amplitude of the disturbance applied to the left boundary of the liquid sheet with the actuation frequency ω . The wave numbers k_2 and k_3 are solutions of the dispersion equation [46, 70]:

$$-\omega^{*2} + 2\omega^*k^* - k^{*2} + \epsilon^2k^{*4} = 0, \quad (3.4)$$

where:

$$\omega^* = \frac{\omega a_0}{u_0} \quad (3.5)$$

$$k^* = k a_0 \quad (3.6)$$

$$\epsilon = \frac{1}{\sqrt{2We}} \quad (3.7)$$

We is the Weber number calculated with the liquid sheet physical properties. The Weber number definition to be used is the one of [46], i.e.:

$$We = \frac{\rho u_0^2 a_0}{\sigma} \quad (3.8)$$

For a given value of ω , the solutions for k_2 and k_3 are:

$$k_2 = \frac{1}{2\epsilon a_0} (1 - \sqrt{1 - 4\epsilon\omega^*}) \quad (3.9)$$

$$k_3 = \frac{1}{2\epsilon a_0} (-1 + \sqrt{1 + 4\epsilon\omega^*}) \quad (3.10)$$

The solution of the linear theory is compared here with the free-surface deformations obtained in a numerical simulation of a viscous liquid sheet emerging from a square shaped nozzle into quiescent air. The flow is assumed to be two-dimensional and because of the developing instabilities (dilatational), only the upper half of the liquid sheet has been considered. The geometry of the solution domain as well as the applied boundary conditions are shown Fig. 3.5.

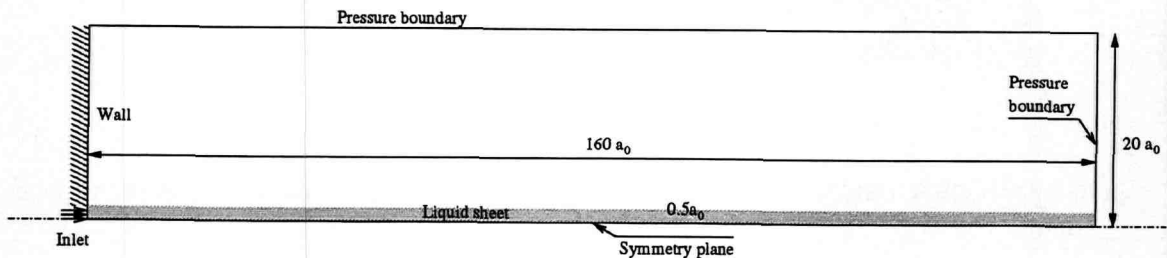


Figure 3.5: Geometry and boundary conditions used for the simulation of a sheet breakup with dilatational mode forcing.

The liquid sheet is forced to undergo free-surface deformations of dilatational type by imposing at the inlet boundary a fluctuating velocity of the type:

$$U(x = 0, t) = u_0(1 - \epsilon_0 \sin(\omega t)) \quad (3.11)$$

a_0 [m]	u_0 [m s ⁻¹]	ρ [kg m ⁻³]	σ [N m ⁻¹]	ω [rad s ⁻¹]	We [-]
0.002	10	1000	0.1111	6283.185307	900

Table 3.2: Liquid physical properties and reference dimensions used for the simulation of the sheet breakup with dilational mode forcing.

with ϵ_0 being the disturbance amplitude, given as a fraction of the undisturbed sheet-velocity. Here a value of $\epsilon_0=0.015$ has been chosen. The actuation frequency ω , the sheet thickness, the value of the surface tension coefficient and the undisturbed sheet velocities are listed in Table 3.2.

The corresponding predicted deformation of the free-surface shown Fig. 3.6 was obtained at the end of the calculation after 20,000 time steps with a non-dimensional time-step size of 0.01, using a_0 as a reference length and u_0 as a reference velocity. One period of actuation is then resolved within 1000 time steps (where 200 times steps should be sufficient), but the limitation on the Courant number ($Co < 0.5$) for the free-surface simulation with the interface-capturing method does not allow to increase the time step any further if a sharp interface between liquid and solid has to be obtained. From Fig. 3.6, it can be seen that the obtained free-surface deformation shows very good agreement with the linear theory up to a distance of $75 a_0$ downstream from the location at which the disturbance is produced: Wavelength and wave-crest amplitudes show very little differences, though wave troughs are less pronounced. This is due to the linear model becoming invalid when the wave amplitude compared to the wavelength exceeds the value of 1%, which is already the case at a distance of $20 a_0$ downstream the inlet. Further downstream (from $75 a_0$ up to the outlet of the computational domain), non-linear effects make the sheet free-surface flatten, whereas the wavelength remains the same: the wave crests flatten out and wave troughs become more peaked.

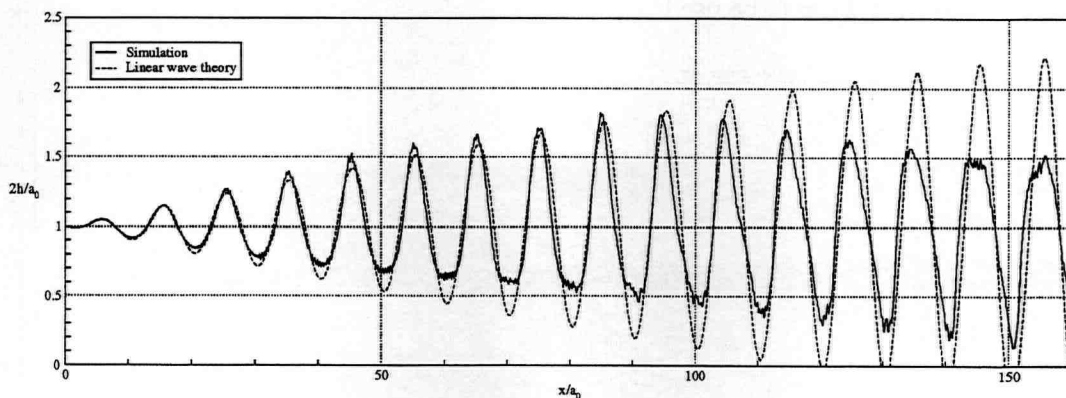


Figure 3.6: Comparison of the sheet free-surface deformations for the dilational mode. The dashed line represents the analytical solution from the linear wave theory; the continuous line represents the free-surface deformation obtained in the present simulation. The Weber number in this simulation was $We = 900$.

Sinuuous mode

In references [46, 70], the equations which model the free-surface deformation of an inviscid and incompressible liquid sheet emanating into a gas with negligible density, are linearized assuming that the sheet free-surface deformations remain small compared to the undisturbed sheet thickness. The sheet free-surface variations are then defined by the position of the sheet centerline y only; the position of the upper and lower sheet free-surfaces are given by an offset of $+0.5 a_0$ and $-0.5 a_0$ respectively, whereby the sheet thickness is considered to remain unchanged. The variation of y in space and time is then given by:

$$y = \frac{1}{u_0} \frac{v}{k_5 - k_6} [\sin(k_6 x - \omega t) - \sin(k_5 x - \omega t)] . \quad (3.12)$$

Here u_0 is the undisturbed sheet velocity and v is the amplitude of the disturbance applied at the inlet in the direction normal to the liquid sheet plane, the actuation frequency being ω . The wave numbers k_5 and k_6 are solutions of the dispersion equation [46, 70]:

$$-\omega^{*2} + 2\omega^* k^* - (1 - 4\epsilon^2)k^{*2} = 0 , \quad (3.13)$$

where the definitions of ω^* , k^* , and ϵ of eqs. (3.5), (3.6) and (3.7) resp. still hold.

For a given value of ω , the solutions of eq. (3.13), k_5 and k_6 , are:

$$k_5 = \frac{\omega}{(1 + 2\epsilon)u_0} \quad (3.14)$$

$$k_6 = \frac{\omega}{(1 - 2\epsilon)u_0} \quad (3.15)$$

The solution of the linear theory is here compared with the free-surface deformations obtained in a numerical simulation of a viscous liquid sheet emerging from a square shaped nozzle into quiescent air. The flow is considered to be two-dimensional, but contrary to the dilational mode, both upper and lower half of the sheet have to be taken into account. Thus, the following model setup shown in Fig. 3.7 has to be used.

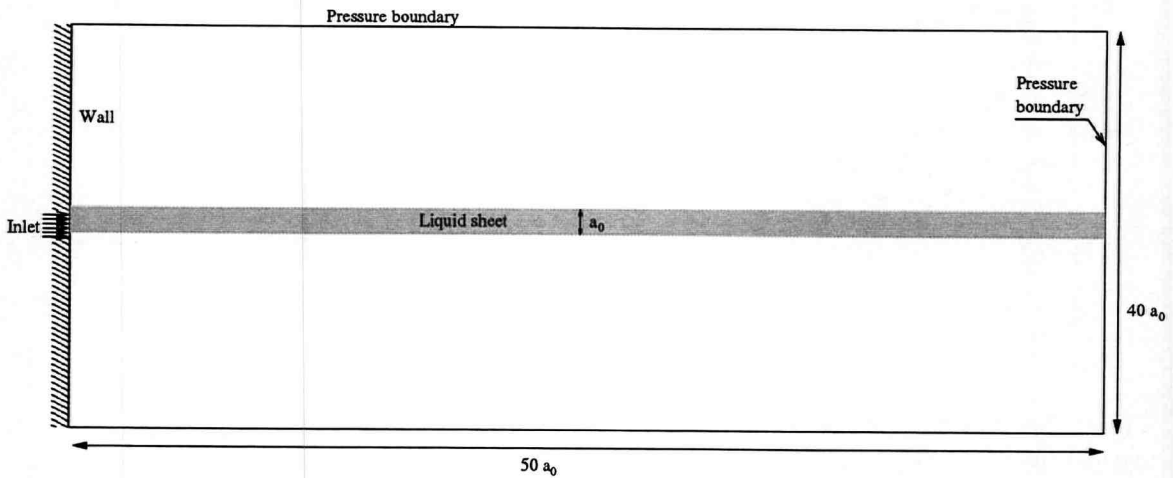


Figure 3.7: Geometry and boundary conditions used for the simulation of a sheet breakup with sinuous mode forcing.

The liquid sheet is forced to undergo free-surface deformations of dilational type by imposing at the inlet boundary a fluctuating velocity of the type:

$$v(x = 0, t) = u_0(1 + \epsilon_0 \sin(\omega t)) \quad (3.16)$$

with ϵ_0 being the disturbance amplitude, given as a fraction of the undisturbed sheet-velocity. Here a value of $\epsilon_0=0.03$ has been chosen. The actuation frequency ω , the sheet thickness, the value of the surface tension and the undisturbed sheet velocities are listed in Table 3.3. The dimensionless time step was 0.005.

a_0 [m]	u_0 [m s ⁻¹]	ρ [kg m ⁻³]	σ [N m ⁻¹]	ω [rad s ⁻¹]	We [-]
0.001	10	1000	0.1111	6283.185307	1800

Table 3.3: Liquid physical properties and reference dimensions used for the simulation of the sheet breakup with sinuous mode forcing.

Figure 3.8 shows the deformation of the free-surface obtained in the simulation. The position of the free-surface is compared to the one predicted by linear wave theory of [46, 70]. As in the dilational case, similar tendencies are observed for this simulation. Up to a distance of $15 a_0$ downstream from the inlet, simulation and theory show excellent agreement in both wavelength and amplitude. Discrepancies between the analytical solution and the calculation become important for a distance greater than $25 a_0$. Then, nonlinear effects change the shape of the free-surface which becomes more peaked at the crests and flatter at the troughs, and the sheet thickness begins to reduce (which would further downstream lead to breakup).

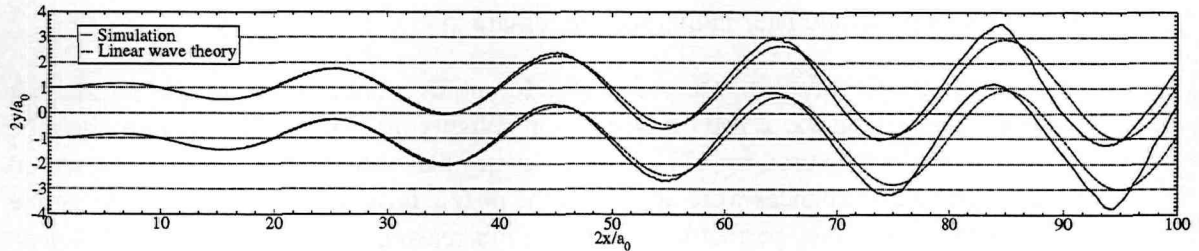


Figure 3.8: Comparison of the sheet free-surface deformation for the sinuous mode. The dashed line represents the analytical solution from the linear wave theory; the continuous line represents the free-surface deformation obtained in the simulation. The Weber number used for the simulation was $We = 1800$.

The numerical method employed here allows to capture accurately the free-surface deformations of a planar liquid sheet at medium-ranged excitation frequencies. The solution shows good agreement with theoretical results where the latter are valid, so that the method can be assumed to be validated for this kind of flows and for this range of actuation frequencies.

3.3 High-frequency excitation

The physical mechanisms leading to jet breakup and finally atomization of liquid jets are unfortunately not well defined and a lot of effort in the last decades has been put into experimental and theoretical investigations in order to understand which factors influence and ameliorate spray characteristics. A key point in these investigations plays surely the nozzle internal flow. Since each disturbance within the nozzle may have an influence on the breakup, it has been decided in the pioneering work of [17, 95] to impose on a given nozzle geometry well-defined disturbances at given frequencies in order to study their influence on the deformation of a round laminar jet. In the present work, the author tried to reproduce the free-surface deformations of the jet from the experiments of [17, 95].

3.3.1 Methodology

For the undertaken numerical simulations, it was found necessary to make initially some simplifying assumptions:

- The boundary layer at the nozzle internal walls may be neglected, so that the simulations can be performed with a plug velocity profile at the nozzle exit.
- Because of the form of the deformed free-surface reported in experimental studies in [95], it can reasonably be assumed that the flow is nearly axisymmetric.
- There is no back influence of the jet flow on the flow within the nozzle. This assumption has been verified in the experiments of [17]. All waves on the jet free-surface, except in a very few, well-defined marginal cases, travel in the direction of the jet mean flow. All the computations presented later in this section remain in this flow category.
- The internal nozzle flow is not turbulent (the Reynolds number based on the nozzle exit diameter range is approx. 2,700 for an ejection velocity of 20 m/s). This feature could be verified for the nozzle used in [17] whose geometry has been used in the work presented here. When no disturbances were applied to the nozzle flow, it could be observed that the jet free-surface remained perfectly smooth. For this reason, no turbulence model has been used in the numerical simulations. In the case of appearing fluctuations of velocity and pressure, it has been assumed that the grid resolution was small enough to resolve them accurately. In other words, the computations are to be considered as direct numerical simulations (DNS).

In order to verify the first two assumptions, the simulation of the nozzle internal flow has been performed. Based on the assumption that there exists no back influence of the jet flow on the nozzle flow, the latter flow could be computed separately using constant pressure at nozzle outlet as a boundary condition. The velocity profiles at the nozzle outlet gained from the unsteady simulations of the nozzle flow have been stored after each time step and reused as the inlet velocity profile for the jet breakup simulations. The resulting free-surface deformations of the jet have been then compared to the ones obtained with the modulated plug profile at the same frequency and amplitude. If the differences are small, then the two first assumptions are valid. For all the performed simulations, the physical properties of liquid and air have been set to those listed in Table 3.4.

fluid	ρ [kg m ⁻³]	ν [m ² s ⁻¹]	σ [kg s ⁻²]
ethanoic alcohol	789	$1.52 \cdot 10^{-6}$	0.0225
air	1.188	$1.55 \cdot 10^{-5}$	-

Table 3.4: High-frequency excitation: Physical properties of the fluids used for the simulations

3.3.2 Nozzle-flow simulations

Two-dimensional nozzle model

The nozzle geometry used for the numerical calculations corresponds to the description of Fig. 3.9. Ethanoic alcohol is injected from the top of the nozzle through an annular slot. It is then accelerated in a conical nozzle before emanating into quiescent air. The distance between the piezoelectric base, where the jet excitation is produced, and the beginning of the conical nozzle could be shifted in experiments and has been set for all the computations to 10 mm. The other geometrical dimensions defining the computational domain have been set to the values shown in Fig. 3.10.

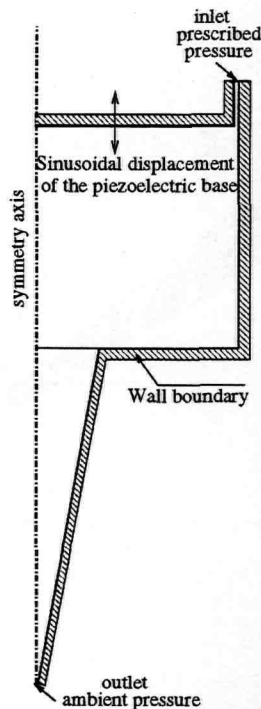


Figure 3.9: Nozzle geometry and boundary conditions used for the numerical simulations of forced break-up of round laminar jets.

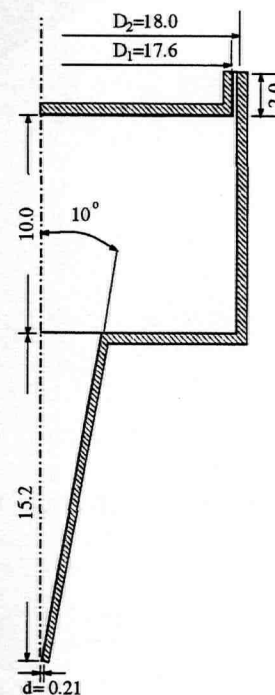


Figure 3.10: Geometrical dimensions of the computational domain. Dimensions are given in millimeters.

For the numerical simulations, three grids with different refinement levels have been used. The coarsest grid is shown in Fig. 3.11. The other grids have been systematically refined in all directions, so that the coarsest grid had 17,579 control volumes (CVs), the next finer one 70,316 CVs and the finest one 281,264 CVs. As the nozzle geometry is axi-symmetric, all the grids are

generated as a slice of one degree angle. The use of local refinement allows to achieve a better calculation accuracy at lower computational costs. Moreover, the grid has been stretched to the walls to resolve accurately enough the boundary layer.

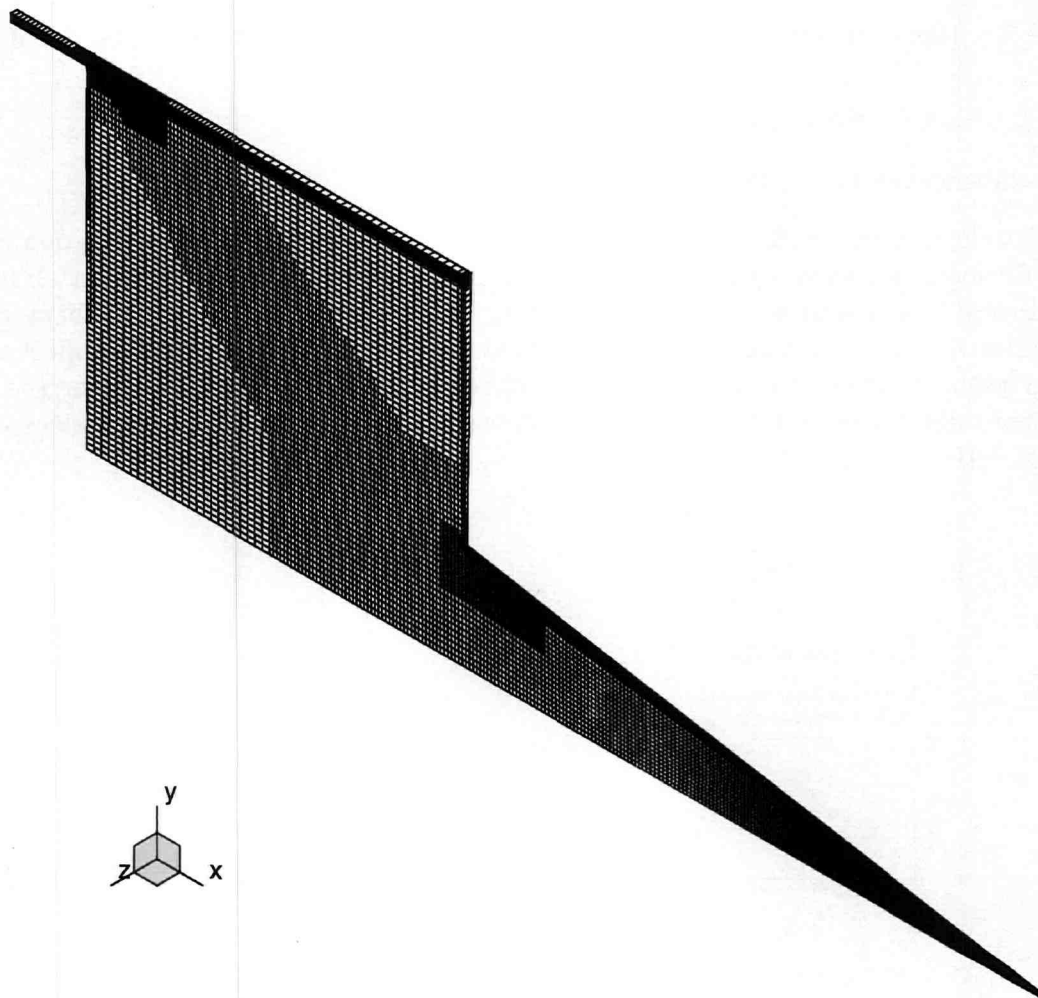


Figure 3.11: Coarsest numerical mesh used for the calculation of the nozzle inner flow with 17,579 control volumes.

Computed working line

The velocity at the nozzle outlet is to be used to set boundary conditions for the jet breakup simulations, which are to be compared with experimental data. To match the measured flow rate in the experiments, the appropriate pressure value has to be set at the nozzle inlet. Unfortunately, there exists no trivial relation between the mean value of the velocity at nozzle exit and the imposed pressure value at nozzle inlet. For this reason, this relation – called here working line – had to be computed. For this purpose, the inlet pressure has been varied and the resulting flow rate calculated. Finally, a set of points is obtained which is fit by a parabola. It has been found that this quadratic fit is a very good approximation of the obtained results. The calculations have been performed on three grid levels corresponding to the grids described in the preceding

subsection. The motivation of this procedure was to estimate the numerical error. The working line of the nozzle model is presented in Fig. 3.12. Fitting the points obtained to a quadratic

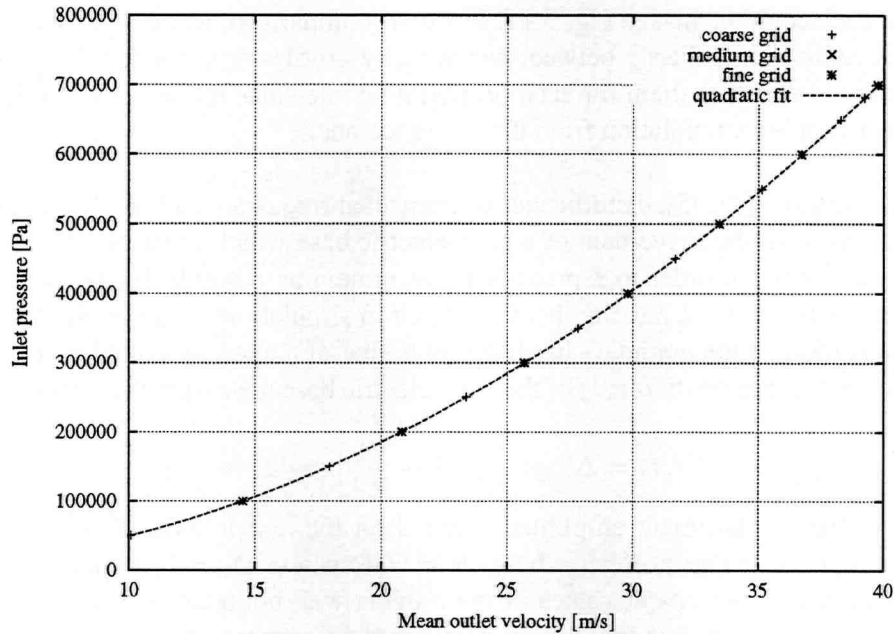


Figure 3.12: Working line of the nozzle

curve gives the relation between the inlet pressure p_{inlet} and the mean outlet velocity U_m with an overall discrepancy of less than 0.03%:

$$p_{\text{inlet}} \approx 419.016 U_m^2 + 1036.98 U_m - 3372.48 \quad [\text{Pa}] \quad (3.17)$$

It should be pointed out that all the calculations have been performed with 100% central differences and that the normalized residual levels have been reduced below than 10^{-4} . The iteration errors were thus smaller than 0.01. Comparison of solutions obtained on the three grids shows very small differences, so that the solution on the finest grid can be considered as very accurate.

Computed velocity profiles

From steady flow calculations, the actual velocity profile at the nozzle outlet is obtained. The profiles have some similarity with a block profile but boundary layer effects are still present, even if limited to a small region in the wall vicinity. Moreover, the radial component of the velocity is not negligible; to enlighten this feature, profiles of the axial and radial velocity components at an inlet pressure of 500,000 Pa are shown in Fig. 3.13. It shows the superposition of the velocity profiles obtained on the three systematically refined grids described above (see also Fig. 3.11 for the numerical grid). It can be observed that the differences between the coarsest mesh and the finest one are very small (less than 1% for the radial velocity) so that it can be assumed that the solutions from the coarse mesh are accurate enough. For this reason, only results obtained with the coarse grid will be presented in the following.

Varying the pressure at the nozzle inlet allows to obtain various outlet velocity profiles. The influence of the inlet pressure on the profiles of velocity components have been analyzed. These velocity profiles obtained for various inlet pressures are plotted in Fig. 3.14. Increasing the

pressure has the effect of increasing the outlet velocity in both axial and radial direction. At the same time, the thickness of the boundary layer reduces, as expected when the Reynolds number increases. This is better seen if the velocity profiles are normalized with the maximum velocity for each component, see Fig. 3.15. From the comparison, it can be concluded that there is obviously no trivial similarity between the velocity profiles at different inlet pressures. It is thus necessary to compute them for each desired flow rate since all velocity profiles cannot be deduced by a simple extrapolation from the reference one.

In the experiments of [17,95], disturbances of controlled frequency and amplitude are generated in the nozzle through the movement of a piezoelectric base which is excited by an electronic sine-wave generator. In order to reproduce as accurately as possible the experimental conditions, the piezoelectric base has first been modeled in simulations as a moving boundary. The imposed movement of the boundary has been set to that of a plate submitted to a uniform loading, so that the displacements $Z(r, t)$ of the piezoelectric base are assumed to obey the following law [32]:

$$Z(r, t) = \Delta Z \sin \left[\frac{\pi}{2} \left(1 - \frac{r}{R} \right) \right] \cos(\omega t + \varphi), \quad (3.18)$$

where ΔZ is the displacement amplitude reached on the nozzle axis of symmetry and R is the half diameter of the piezoelectric base ($R = D_1/2$ where $D_1 = 17.6$ mm, see Fig. 3.10). Unfortunately, the displacement values of the moving wall boundary are so tiny – actually in the range of one to several hundred nanometers – that the preprocessing tool of the flow solver, which is used to redefine the grid during the boundary movement, has not enough accuracy to capture them. Since the flow is supposed to be of laminar nature, it is then possible to redefine the moving wall boundary as an inlet boundary with a prescribed velocity equal to the time derivative of the wall movement. Taking the time derivative of equation (3.18), we get the model for the inlet velocity $U_z(r, t)$ applied at the moving wall boundary:

$$U_z(r, t) = \Delta U_z \sin \left[\frac{\pi}{2} \left(1 - \frac{r}{R} \right) \right] \sin(\omega t + \varphi), \quad (3.19)$$

where ΔU_z is related to ΔZ by the following equation:

$$\Delta U_z = -\omega \Delta Z. \quad (3.20)$$

In the following, the mean nozzle outlet velocity was set to 21 m/s as for the steady flow. From the working line of the nozzle (see also Fig. 3.12), the corresponding pressure for the nozzle inlet boundary has been obtained and set to 203,142 Pa. For verification, a steady nozzle flow simulation with this pressure value gives indeed the desired flow rate.

In all the calculations, the outlet boundary condition was set to be of pressure type, where the pressure level was forced to have the value of atmospheric pressure. Also, a convective boundary condition on pressure, as described in the preceding chapter, has been applied in expectancy that possibly developing convective instabilities would be better convected out the computational domain. However, no noticeable difference on the obtained outlet velocities between the use of both conditions could be found, so that the standard pressure condition was used for the rest of the calculations.

The excitation frequency was set to 126 kHz. The excitation amplitude has been set to various levels by changing the value of ΔZ . Only the results obtained for $\Delta Z = 175$ nm are presented

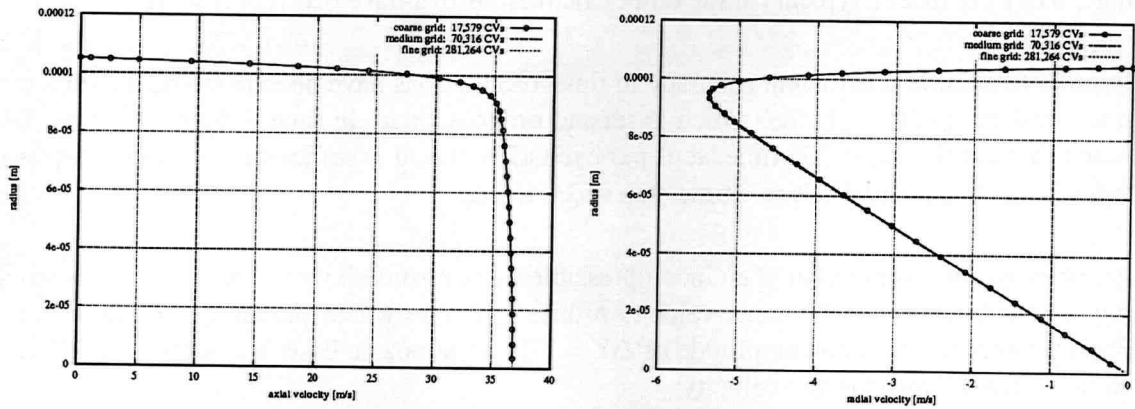


Figure 3.13: Outlet velocity profiles for different grid resolutions at an inlet pressure of 500,000 Pa.

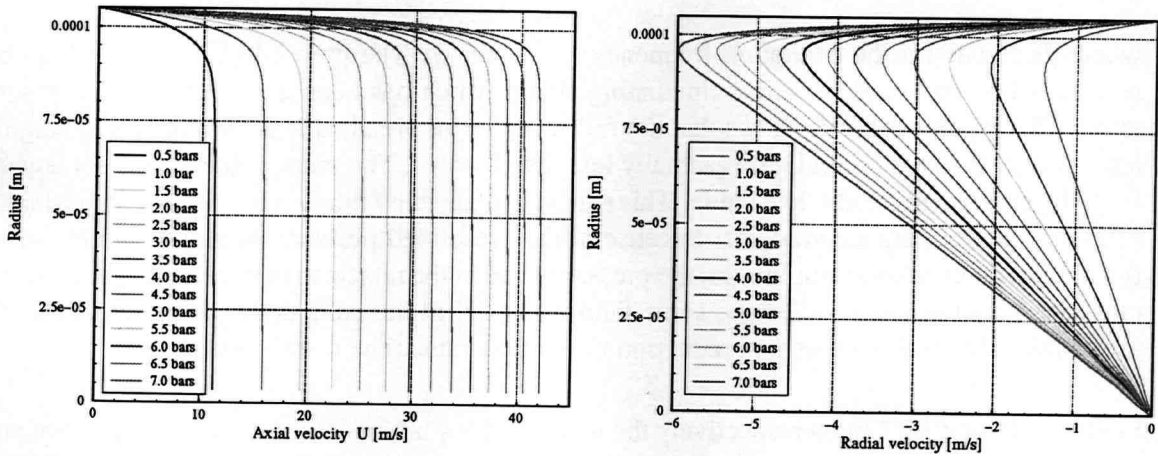


Figure 3.14: Profiles of axial (left) and radial (right) velocity profiles at the nozzle outlet for different inlet pressures. Results have been obtained on the coarse grid.

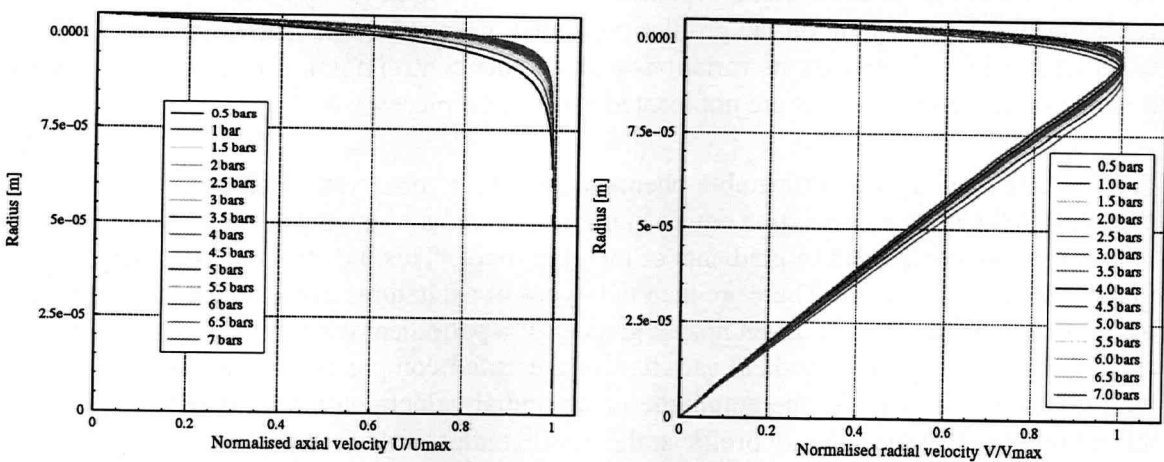


Figure 3.15: Normalized profiles of axial (left) and radial (right) velocity profiles at the nozzle outlet for different inlet pressures. Results have been obtained on the coarse grid. Normalization is performed with the maximum value of the velocity component.

here. They are indeed typical for the other calculations that have been conducted.

In order to achieve a sufficient accuracy in time, calculations have been performed with a three time level integration scheme, which is second order accurate in time. Moreover, it has been found that the choice of 300 time steps per excitation period is sufficient to obtain accurate integration in time. This leads to a time step of 26.455 ns.

As expected for a simulation of an incompressible fluid, results show no phase shift between the imposed excitation and the mean velocity profile: pressure waves propagate at infinite speed. For the imposed excitation amplitude of $\Delta Z = 175$ nm at nozzle base, we obtain the following variation for the mean outlet velocity:

$$U_m(t) \approx 20.63575 + 5.83612 \sin(2\pi f_0 t) \quad [\text{m s}^{-1}], \quad (3.21)$$

where f_0 stands for the excitation frequency ($\omega = 2\pi f_0$). The preceding expression can be seen as a Fourier series of a time fluctuating signal which has been truncated to the first two terms. The Fourier analysis shows that the following terms are all at least two orders of magnitude smaller than the second term (actually less than 0.15%). The mean value differs somewhat from the prescribed steady flow value. This can be explained by the development of an unsteady boundary layer in the annular slot. Because of the prescribed pressure boundary and because, for significant excitation amplitudes, the pressure level in the nozzle may become larger than the prescribed inlet pressure of 2 bars, some fluid flows out of the computational domain through the annular slot, leading thus to a reduction of the flow rate at the nozzle outlet.

Figures 3.16 and 3.17 show respectively the modifications in time of the axial and the radial velocity components over an excitation period. Considering control points located in wall vicinity – corresponding approximately to the zone $0.095 \text{ mm} < r < R = 0.105 \text{ mm}$ –, they are all influenced by the presence of an unsteady boundary layer. As a matter of fact, they are differently accelerated or decelerated depending on their position in the boundary layer. Taking for instance a control point on the profiles presented on Fig. 3.16, its variations in time are of sinusoidal nature. Comparing its variations with another control point, one can observe that the maxima of the time variations are not located at the same places.

For the radial velocity, a comparable phenomenon can be observed. But, because of incompressibility, the mass conservation equation imposes to redistribute the changes on the gradient of one velocity component to gradients of the other ones. This induces a phase change on the radial velocity component. There are then two types of excitations of the jet for a given perturbation frequency and for the given nozzle geometry: a periodical variation of the axial velocity as well as an additional periodical variation of the radial component which has a phase shift with the axial velocity. As the amplitude of the radial velocity component is not negligible, the assumption that the velocity profile at the nozzle outlet could be modeled by the sinusoidal modulation of a block profile is not valid. For this reason, it is then indispensable to calculate for a given frequency and a given excitation level the outlet profiles for both velocity components (radial and axial) and to store them over one period for each time step, in order to use them as inlet boundary conditions for jet simulations.

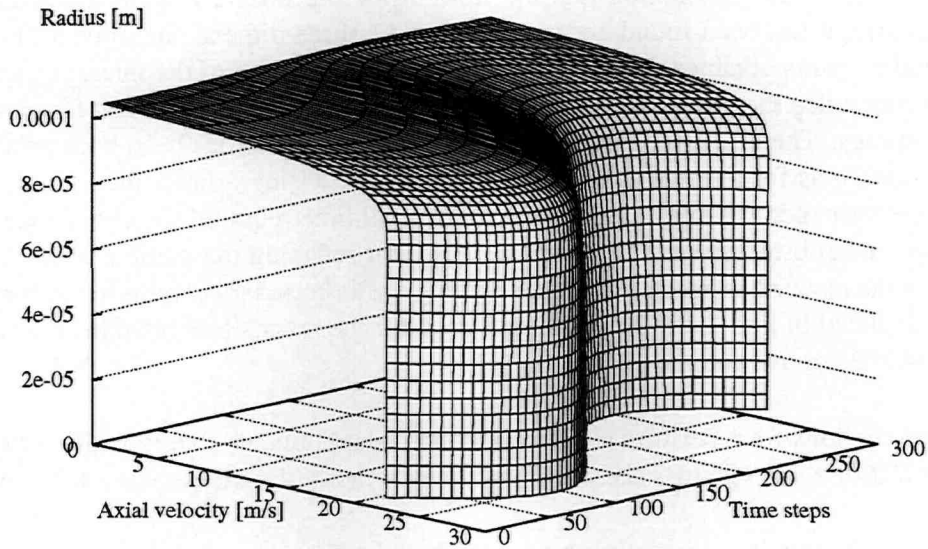


Figure 3.16: Axial velocity profiles at nozzle outlet vs. time over one period. $\Delta Z = 175$ nm, $f_0 = 126$ kHz.

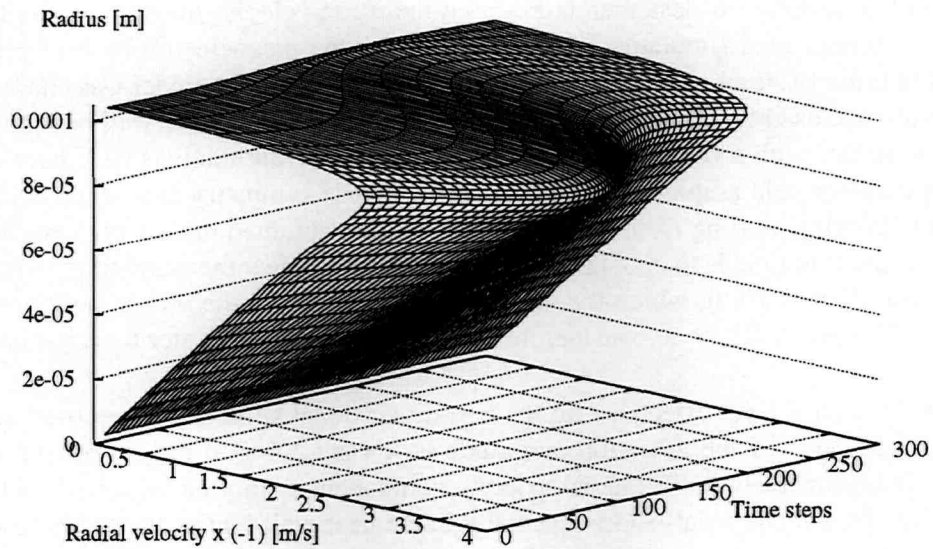


Figure 3.17: Radial velocity profiles at nozzle outlet vs. time over one period. $\Delta Z = 175$ nm, $f_0 = 126$ kHz.

Three-dimensional model

In order to verify the assumption that the flow inside the nozzle is almost two-dimensional axi-symmetric, it has been found necessary to build a three-dimensional model of the nozzle. Based on the results obtained for the two-dimensional simulation of the internal nozzle-flow, it has been concluded that the mesh resolution of the coarse grid was sufficient for obtaining sufficient accuracy. Therefore, the three-dimensional nozzle-model has been built using the same mesh resolution as for the two-dimensional coarse grid. Using a finer three-dimensional grid would have tremendously increased the computational time required for performing the calculations with no substantial gain in accuracy. Also, for reducing the computational effort, only one half of the nozzle has been simulated, applying cyclic boundary conditions on the symmetry plane as depicted in Fig. 3.18. The final grid used for the results presented hereafter contained thus 1,324,862 control volumes.

All the calculations were performed with a second-order boundary extrapolation procedure and full central-difference schemes (i.e. no blending with first order differencing schemes).

As in the two-dimensional case, the pressure at the inlet boundary of the computational domain has been varied and the mean outlet velocity has been calculated for obtaining the steady-state working line of the nozzle. The working line so obtained is depicted Fig. 3.19. The calculated operating points have been compared with the quadratic fit obtained for the two-dimensional model, eq. (3.17). Excellent agreement between the quadratic fit and the computed operational points is found, confirming that the grid choice for the three-dimensional simulation based on the two-dimensional coarse grid leads to accurate enough results, see Fig. 3.19.

Choosing a pressure level at the inlet boundary of 203,190 Pa gives a mean outlet velocity of 21 m/s with a deviation of less than 0.005% on the mean velocity magnitude. As in the case of the two-dimensional simulation, the movements of the piezoelectric base of Fig. 3.9 are imposed in order to simulate unsteady flow. The wall displacement model was chosen to correspond to the one used for the two-dimensional computations, hence the wall being modeled by an inlet boundary with a velocity profile obeying eq. (3.19). Simulations have been performed using the displacement amplitude of 100 nm at the nozzle symmetry axis at the excitation frequency of 126 kHz, starting from the converged solution obtained in a steady-state analysis. A periodic solution in time is then obtained very rapidly after a few thousand time steps. This can be seen from Fig. 3.20, in which the area averaged velocity at the nozzle outlet over time is displayed. The graph allows to consider the solution being periodic after 6 excitation periods.

The same boundary layer effects as for the two-dimensional simulation are observed, see Fig. 3.21 and 3.22, even if the actuation amplitude is lower ($\Delta Z=100$ nm instead of 175 nm in the two-dimensional case): The radial velocity component cannot be neglected; both velocity components (radial and axial) show especially in the near wall region strong phase shifts with the imposed actuation, due to the unsteadiness of the flow field.

Once the periodic state had been reached, the velocity profiles at the nozzle outlet were stored over one period for later use as inlet boundary condition for the jet breakup simulation. Typical velocity profiles obtained at the nozzle outlet for are shown in Fig. 3.23.

From the results obtained from the two-dimensional and three-dimensional simulations of the

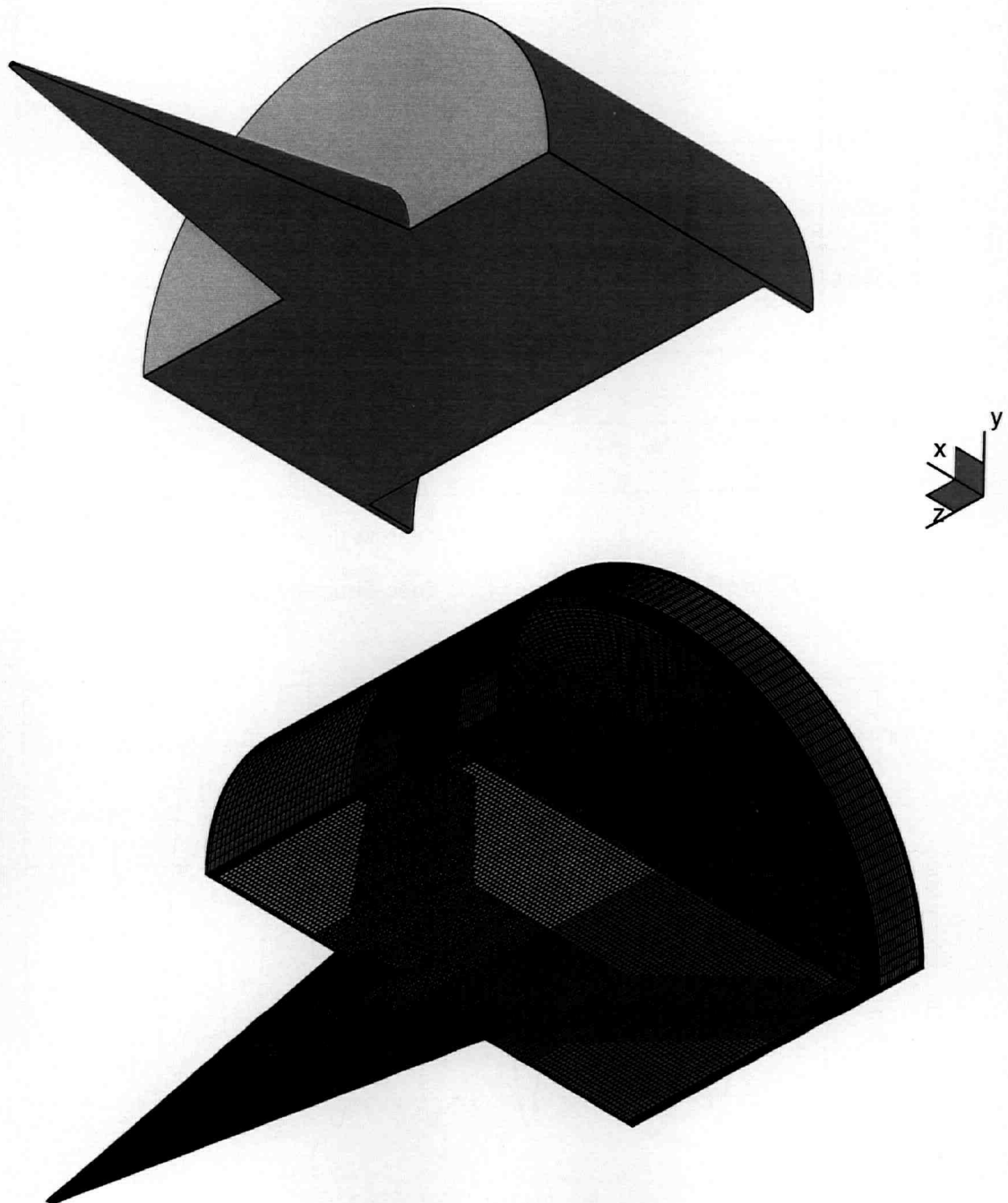


Figure 3.18: Geometry (top) and numerical mesh (bottom) used for the 3D nozzle simulation. The same mesh density is used as in the two-dimensional case, Fig. 3.11. Periodic boundary conditions are depicted in gray and red on the figure.

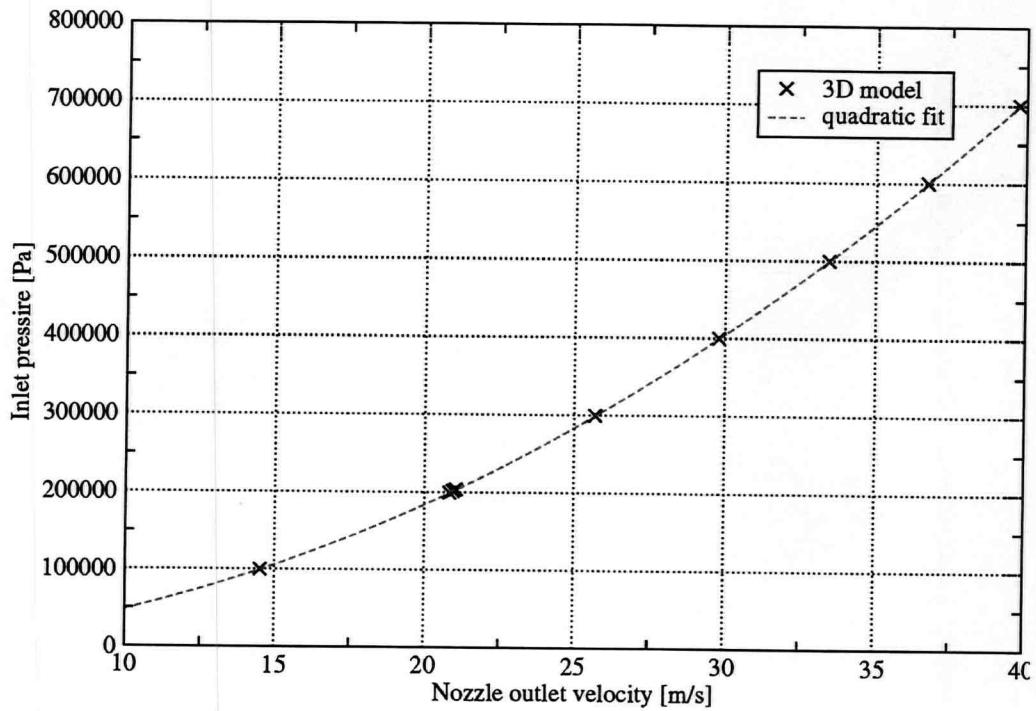
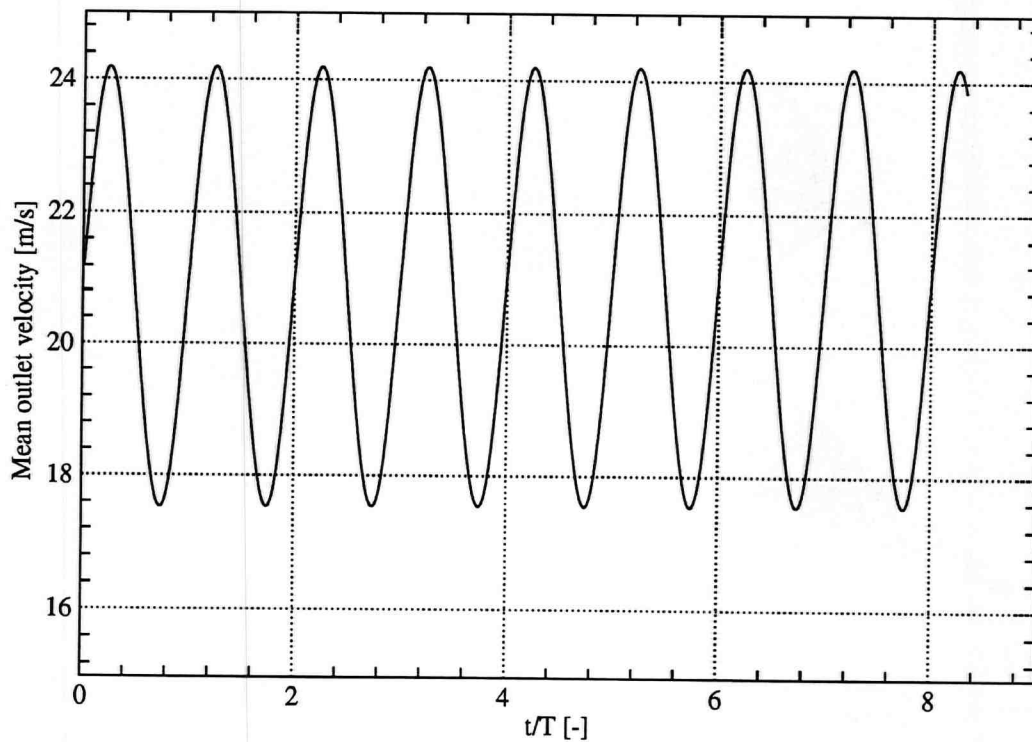


Figure 3.19: Working line of the three-dimensional nozzle

Figure 3.20: Mean velocity at the nozzle exit over time. Time is made dimensionless by using the excitation period. Periodicity is achieved within a few excitation periods. $\Delta Z = 100$ nm.

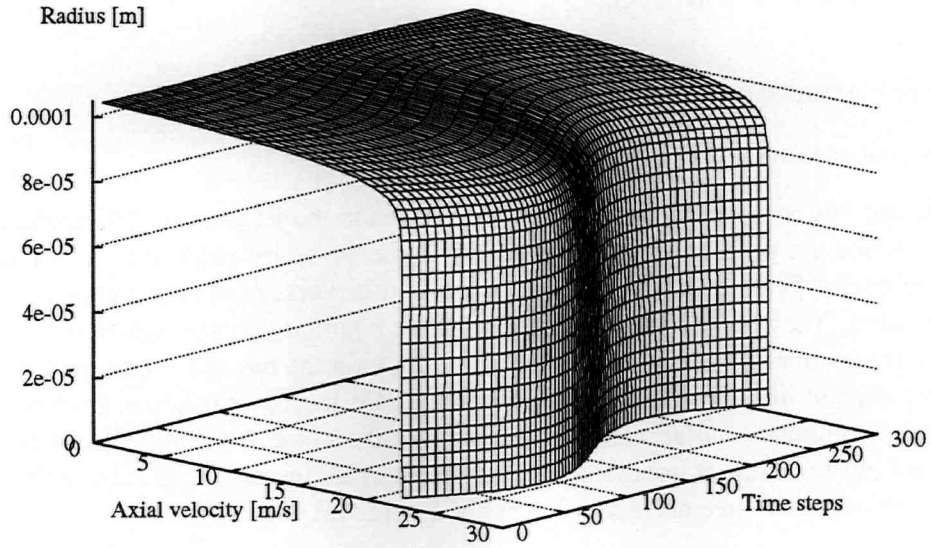


Figure 3.21: Axial velocity profiles at nozzle outlet vs. time over one period. The velocity profile is obtained at one cross section of the nozzle outlet. $\Delta Z = 100$ nm, $f_0 = 126$ kHz.

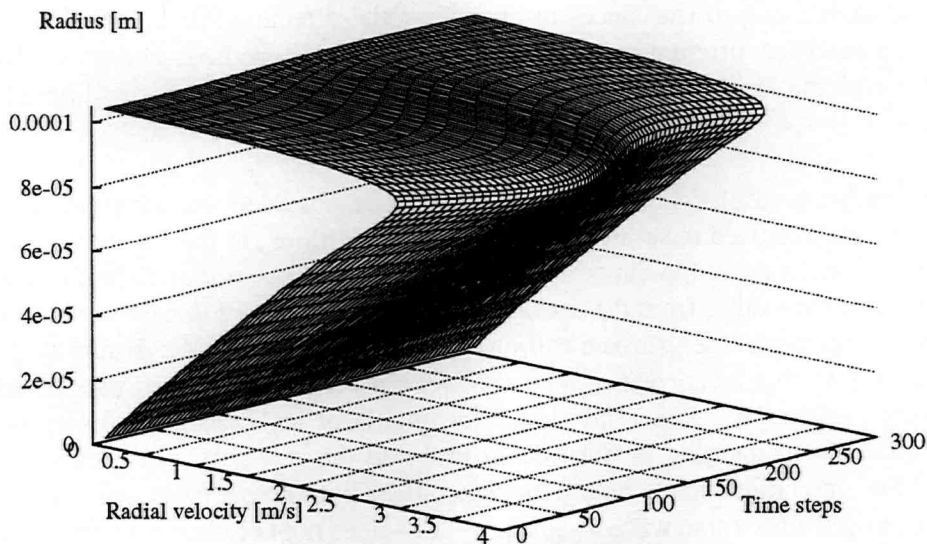


Figure 3.22: Radial velocity profiles vs. time over one period of actuation. The velocity profile is obtained at one cross section of the nozzle outlet. $\Delta Z = 100$ nm, $f_0 = 126$ kHz.

nozzle internal flow, no noticeable difference between the results is found and it can be concluded that, up to the assumption made concerning the boundary conditions and fluid properties, the nozzle internal flow is axi-symmetric.

3.3.3 Jet-breakup simulations

Two-dimensional model

Assuming initially that the phenomena to be observed in the jet are axi-symmetric, it is meaningful to reduce the problem from three to two dimensions by modeling only a slice with a one-degree angle. For the simulations presented in this work, numerous numerical grids have been generated. They all use the geometry with the boundary conditions of Fig. 3.24. Experience has shown that the pressure boundary condition on the top of the computational domain allows entrainment of the background fluid in which the liquid jet is issued from the lower left corner of the computational domain. An example of the numerical grids for this purpose used is presented in Fig. 3.25. It uses local refinement in order to capture as accurately as possible the deformations of the free surface at lower computational costs.

It is worth to analyze the influence of the use of a “realistic” inlet boundary condition which has been obtained with the nozzle-flow simulation and the one with a very simple model, i.e. a block profile modulated in time by a sine wave as:

$$U_z(r, z = 0, t) = U_m[1 + \epsilon_0 \sin(2\pi f_0 t)]; \quad 0 \leq r \leq \frac{D}{2}, \quad (3.22)$$

where ϵ_0 is a measure for the disturbance amplitude. This model – in addition to neglecting boundary-layer effects – does not take any time variations of the radial velocity component into account and allows only disturbances to apply in axial direction. This model is very simple and has been used for different values of ϵ_0 . These values have been chosen so that they are comparable with the disturbance level on the mean outlet velocity obtained with various nozzle simulations.

From the simulation results shown in Fig.3.27, it can be observed that the form of the velocity profiles at nozzle exit used to set the inlet boundary conditions for the jet flow simulation have various effects on the development of instabilities at the jet free-surface. Using on the one hand velocity profiles emanating from the nozzle-flow simulation allows to capture some interesting effects: waves on the jet free-surface roll-up until a certain level of the disturbance amplitude is reached. Up to this level, one observes a forward merging of the surface waves creating gas inclusions in the jet. Above this level, the inertia of the created waves is too large for allowing a backward merging of the free surface and the free surface is deformed as in the manner of the simulations made with a block profile. On the other hand, using a block profile modulated in time with a sine wave – see eq. (3.22) – does not take into account boundary layer effects which are caused by the nozzle walls. Moreover, the radial velocity component is totally neglected. In that case, free surface deformations are only developing from a disturbance on the axial velocity. Compared to the other type of inlet condition, no merging of the free surface is observed. On the contrary, for a much smaller disturbance amplitude, the jet already develops a typical bell-shaped form. For greater amplitudes, droplet ejection – tube ejection would be a more appropriate term here – is also captured. Therefore, the velocity differences between the

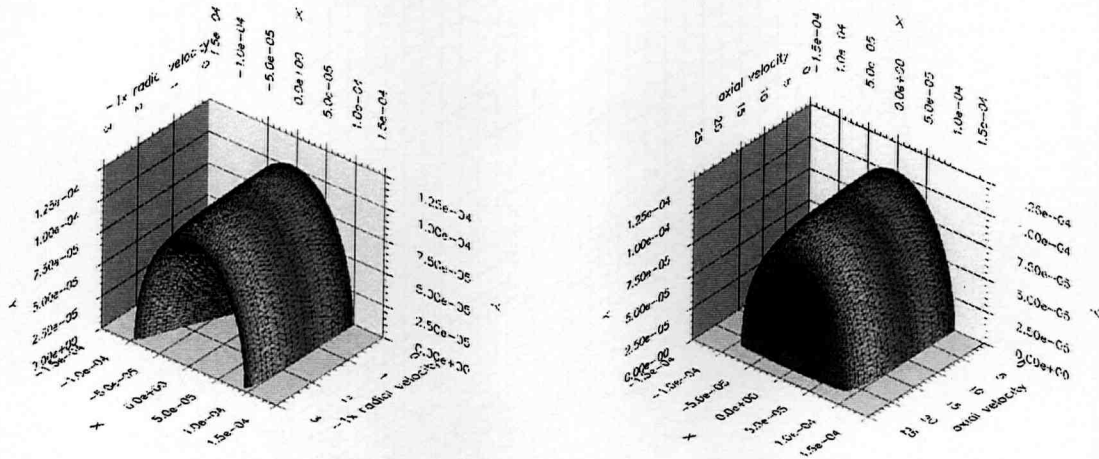


Figure 3.23: Typical velocity profiles in radial and axial directions obtained at the nozzle outlet.

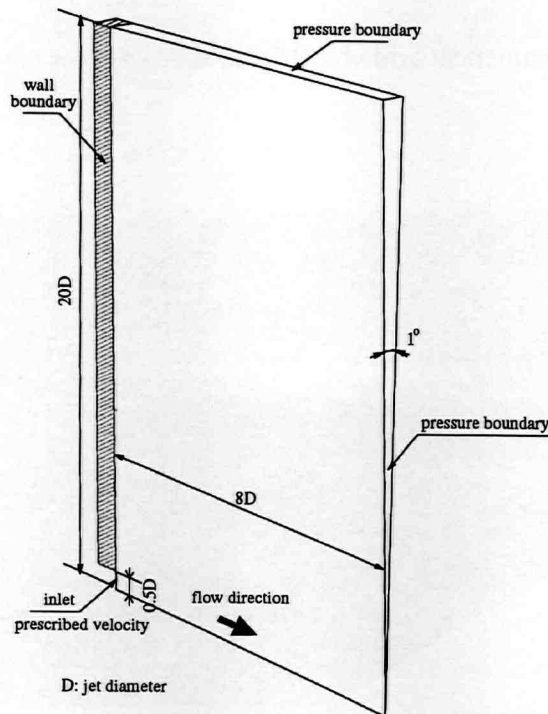


Figure 3.24: Layout of the computational domain with the boundary conditions employed.

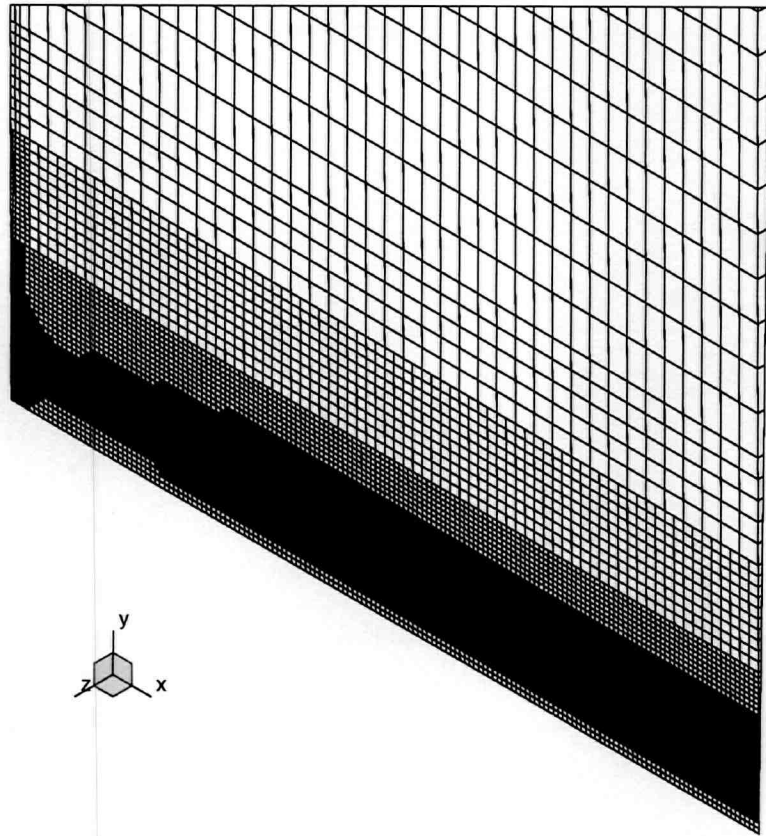


Figure 3.25: Detail of a numerical grid with 16,960 CVs used for the two-dimensional simulations of jet breakup.

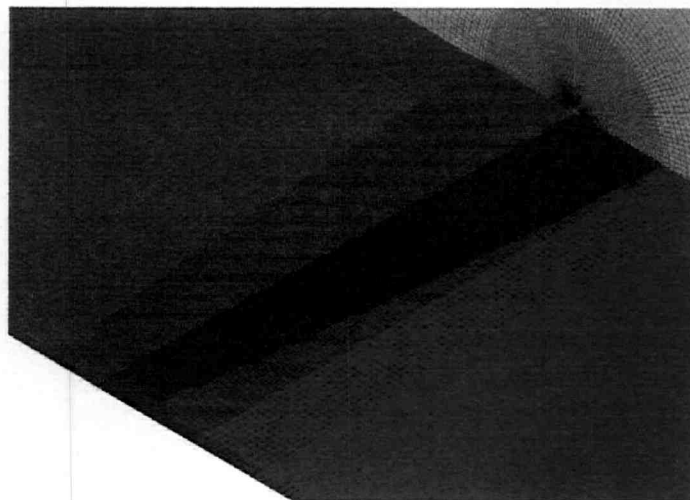


Figure 3.26: Detail of the mesh used for the three-dimensional jet-breakup simulations. Cyclic boundary conditions are used on the regions colored in red and green on the figure.

jet core and the jet surface – because of the nozzle boundary layer – as well as radial velocity components are responsible for the wave roll-up on the jet surface. The core velocity is only responsible for the wave transport in downstream direction. If the inertia is high enough, the waves are convected more rapidly than they can roll-up, which explains the development of a bell-shaped wave form, provided that the disturbance amplitude exceeds a certain level.

Three-dimensional model

In the previous two-dimensional study of the forced jet breakup, it has been found that, depending on the actuation amplitude, rings of fluid detach from the jet free-surface. But, because of the size of the ejected rings (in the range of several $10 \mu\text{m}$), surface-tension effects are likely to force the rings to undergo a Rayleigh-type breakup and eventually droplets are created. The motivation of the present study is to use three-dimensional models in order to capture the expected jet breakup behavior and eventually the formation of droplets.

Simple actuation model

In order to check whether the same strong influence of the velocity profile imposed at the inlet boundary of the jet flow simulation is obtained in 3D as well, or some other three-dimensional effects will be more dominant, it has been decided to neglect initially boundary layer effects arising from the nozzle internal flow and to assume the flow issuing the nozzle can be represented by a block profile. Hence, the velocity is represented by the sinusoidal modulation in time according to the following equation, when considering a cylindrical coordinate system which symmetry axis is aligned with the jet axis:

$$U_z(r, \theta, z = 0, t) = U_m [1 + \epsilon_0 \sin(2\pi f_0 t)]; \quad 0 \leq r \leq \frac{D}{2}, \quad (3.23)$$

where ϵ_0 is a parameter used for setting the level of actuation for the jet disturbance and is given in percentage of the mean jet velocity U_m ; f_0 represents the excitation frequency, which is set to the same value as the one used in the two-dimensional investigations, hence 126 kHz. Here, in order to compare directly the results with those obtained in the two-dimensional simulations, the excitation level has been fixed to $\epsilon_0 = 16\%$.

The velocity profile of eq. (3.23) has been imposed as the inlet boundary condition to the numerical mesh presented on Fig. 3.26. The numerical grid has been built with the same cell density as for the corresponding two-dimensional simulation with the same excitation level, so that direct comparison with two-dimensional simulation results can be undertaken. Also, in order to save computational effort, only one half of the complete three-dimensional computational domain has been modeled and cyclic boundary conditions have been applied. The final mesh involved so 1,376,862 control volumes.

Surprisingly enough, the results obtained with the forcing of eq. (3.23) – with a disturbance amplitude of $\epsilon_0 = 16\%$ – do not lead to the expected formation of droplets; the rings of liquid that detach from the developing wave train, see Fig. 3.29, remain stable and the solution is nearly axi-symmetric, corresponding to that obtained in two-dimensional simulations. The deformations of the jet free-surface are periodic with the same frequency as the one of the excitation

source. Therefore, results are shown over one period.

As in the case of the Rayleigh jet-breakup mode, the fluid rings ejecting from the jet free-surface are unstable and should break up and form droplets, provided that there exist some disturbances along the axis of the fluid torus, i.e. in azimuthal direction. However, from Figs. 3.30 and 3.31, it can be seen that the time averaged velocity in this direction is almost zero, or at least very small compared to the velocity components in radial and streamwise directions. The same is also observed for the rms values of the time averaged velocity fluctuations in the azimuthal direction. The highest values are obtained in the zone where the fluid torus detaches from the jet free surface and free surface contracts rapidly (film collapse). Nevertheless, the observed velocity fluctuations do not lead immediately to droplet formation.

Also from Figs. 3.30 and 3.31, it can be seen that the jet develops until the free-surface reaches a maximum amplitude, where fluid rings detach from the jet. Beginning from this position, the liquid and gas flow becomes more uniform: the bell-shaped free-surface travels downstream with almost the imposed jet ejection velocity (hence, 21 m/s), the velocity fluctuations decrease in amplitude. One can then conclude that, within a few nozzle diameters, if surface tension effect are neglected, convection is the only driving force for the flow.

Influence of the nozzle internal flow

Considering that the imposed variation of the velocity profile (eq. (3.23)) at the inlet boundary cannot account for any radial or azimuthal disturbances that may arise from the nozzle internal flow, it is then necessary to investigate the jet breakup behavior when such additional disturbances are present. The most meaningful velocity profile to be used corresponds to the one obtained from the three-dimensional nozzle flow simulation. Under the assumption that the disturbances in the jet do not travel backwards but rather in downstream direction (as shown in the experimental work of [17]), the nozzle flow simulation could be run separately and the outlet profiles stored at every time step. The profiles were then reused as an inlet boundary condition for the jet breakup simulation. Since the flow pattern in the nozzle is periodic, it is then only necessary to store the velocity profiles over one period. Special care has to be taken to determine the correct velocity at the jet inlet at any given time. In the present investigation, the mesh density at the nozzle exit was, however, chosen to match exactly the one used at the inlet boundary of the computational domain of the jet breakup simulation. Thus, any kind of interpolation errors due to non-matching surface grids could be avoided. Further, any kind of interpolation errors in time has been avoided by taking the same time step for the simulation of the nozzle internal flow and the jet flow. Finally, the inlet conditions for the jet flow simulation were obtained with an actuation amplitude matching the one of the simple excitation model.

The corresponding free-surface deformations obtained in the simulation are shown in Fig. 3.32. Again, as in the case with the simple excitation model, the flow pattern obtained is periodic with the period of the imposed actuation. Compared to the jet deformations obtained with the block profile, Fig. 3.29, the free-surface deformation here undergoes a totally different behavior: backward breaking of the growing waves is observed, leading first to a growing wave whose amplitude decreases after the gas-fluid interface has rolled up. The free-surface deforms in the same way as with the two-dimensional model. And again, no droplet ejection from the free-surface is observed.

As in the case of the simple jet actuation, the values of the velocity fluctuations decrease as the jet develops and it can be considered that after some distance downstream the nozzle, the flow pattern is uniform, Fig. 3.33 and 3.34. Of course, higher fluctuations are observed in the zone where the interactions between the liquid jet and the surrounding gas are important: near the nozzle exit, where gas entrainment due to the interfacial shear appears and where the pressure fluctuations pinch the free-surface, but also in the regions where the free-surface experiences backward merging. However, the intensity of the fluctuations, especially in the azimuthal direction, is not high enough to supersede the production or ejection of droplets from the jet free-surface.

Influence of azimuthal disturbances

As no droplet creation could be observed within the computational domain during the simulations with both simple actuation model and with the inlet profiles gained from the nozzle flow simulation, one can conclude that the absence of droplet creation is due to the fact that in both cases there exist little or no azimuthal disturbances. Such disturbances are, however, likely to be present in the reality due to imperfect axi-symmetry of the geometry and/or forcing displacements of the nozzle base. In order to investigate possible effects of azimuthal disturbances on the jet breakup behavior, a disturbance in azimuthal direction has been superimposed onto the block profile for the simple excitation model. The form of the disturbance has been chosen to have the spatial and temporal divergence-free variation given by:

$$U_r(r, \theta) = \epsilon_1 U_m \frac{k_\theta r}{2} \cos(k_\theta \theta) \quad (3.24)$$

$$U_\theta(r, \theta) = \epsilon_1 U_m r \cos(k_\theta \theta) \quad (3.25)$$

where k_θ is the disturbance wavelength in azimuthal direction and has been chosen to have a meaningful value, here 8. The maximum amplitude of the disturbance so applied is a fraction of the mean jet velocity, where the fraction is given by the factor ϵ_1 . For the results presented hereafter, ϵ_1 has been set to 2%. The excitation level in streamwise direction remained fixed to 16%.

The resulting flow pattern obtained with this kind of excitation also undergoes periodicity and therefore the free-surface deformations shown in Fig. 3.35 cover one actuation period T in steps of $0.1T$. As in the case of the simple excitation, waves grow on the jet free-surface and take a similar form as the ones of Fig. 3.29. But, because of the excitation applied in azimuthal direction, an azimuthal wave develops on the waves crowns and leads further downstream to the creation of droplets, from each torus in the same way as a jet undergoes a breakup of Rayleigh type [65]. The difference is that the mean azimuthal velocity in liquid rings is equal to zero; however, since only the disturbance around the mean is of importance for the development of instabilities, the mechanism of droplet generation is the same as in jets with a non-zero mean axial velocity.

Again, as observed in the previous simulation results, the velocity field becomes more uniform with the travel distance from the nozzle inlet, see Fig. 3.36. Also, since the imposed velocity variations in azimuthal direction are periodic in time, the resulting time averaged value must be nearly zero, at least in the vicinity of the nozzle outlet, which correlates well with the results

of Fig. 3.36. The root mean squared values of the obtained velocity field are shown Fig. 3.37. From this figure, the same behavior as for the case of the simple actuation is observed for the velocity fluctuations in radial direction, Fig. 3.31. In the azimuthal and streamwise directions, contrary to the case of the simple actuation, since an azimuthal disturbance exists, the root mean square values do not decrease any more and these perturbations are of a greater amplitude where the ejection of fluid rings is produced as well as where the droplets are created. This can be related to a Rayleigh type breakup of the liquid rings, for which the instability mechanism described in Section 3.1 is due to an in time exponentially growing disturbance.

Influence of azimuthal disturbances superimposed onto the nozzle flow

Finally, in order to complete the investigation on the influence of azimuthal disturbances on the jet breakup, the azimuthal disturbances of eqs. (3.24) and (3.25) have been superimposed onto the velocity profiles which were obtained with the simulation of the nozzle internal flow. Due to the liquid compressibility – see also next section –, azimuthal disturbances can be self-created from the forcing at the nozzle base and self-sustained because of possible resonant modes of the nozzle cavity. The form of the applied disturbance here is similar to the one obtained with an compressible simulation and, since the disturbances appear being of periodical nature, the disturbance applied to the nozzle velocity profiles obtained in an incompressible simulation model in a consistent manner disturbances which would arise from compressible simulations. The maximum amplitude of ϵ_1 in eqs.(3.24) and (3.25) has been set to the same level as in the case of the simple actuation ($\epsilon_1=2\%$), the excitation level in streamwise direction remained the same as in the case for which the nozzle internal flow was used for delivering the inlet boundary conditions to the jet breakup simulation. The wavelength of the azimuthal disturbance was set to $k_\theta=8$.

The deformations of the free-surface were found to undergo a periodic behavior after several periods of excitation. Thus, Fig. 3.38 shows the deformations of the jet-free surface obtained in the simulation over one period of actuation T in steps of $0.1T$. As in the case of the simulation of the jet breakup using the velocity profiles gained from the nozzle flow simulation, waves are formed, then roll up before merging with the next incoming wave. Because of the azimuthal disturbance applied, instead of obtaining bell-shaped, axi-symmetric waves, a fingering of the wave crown is observed. This phenomenon is amplified due to surface-tension which contracts the liquid-gas interface and will lead eventually to the formation of droplets further downstream the observation window.

From Fig. 3.39, it can be seen that, as found in all preceding simulation results, the flow field becomes more uniform with increasing distance from the nozzle outlet. The time averaged value of the azimuthal velocity is in this case still smaller than the values of the other velocity components (radial and axial) but shows higher variations in the zone where the free-surface undergoes roll-up and backward merging with the creation of large gas inclusions. This behavior is also found for the time-averaged root mean square (rms) value of Fig. 3.40. For all velocity components, the highest variations are obtained in the zone where breakup and backward merging occurs, except for the radial component of the velocity, for which the rms values are also high near the inlet of the computational domain. These values are mainly due to the gas entrainment in this region shown by the negative values of the radial velocities on Fig. 3.39 and to the form of superimposed excitation which increases with increasing radius, see also

eqs. (3.24) and (3.25). After some distance from the nozzle orifice, the rms level of the radial velocity becomes less important at the wave crowns compared to the splashing phenomenon, when waves are rolling up and merging backwards.

3.3.4 Comparison of the simulation results with experimental data

One of the motivations of the numerical simulations presented so far was to allow a direct comparison of the computations with the experimental observations in order to achieve a better understanding of the jet breakup phenomena. Corresponding experiments have been conducted at the IMFD (Institut für Mechanik und Fluidodynamik, Technical University Bergakademie Freiberg, Germany), which involved among others the injection of ethanoic alcohol into ambient air at various injection pressures, disturbance amplitudes and frequencies. Some of the experimental results have been made available for comparisons with present simulation in the frequency range presented in this work.

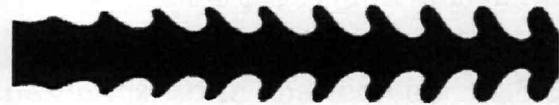
The nozzle geometry described in Figs. 3.9 and 3.10 approaches the geometry of the nozzle used in the experiments and the boundary conditions used were chosen to reproduce as accurately as possible the experimental conditions. Since the disturbance applied is of periodic nature, the observation of jet deformations under stroboscopic light has been realized. In most cases, it has been observed that the response of the jet deformations to the periodical excitation is also of periodic nature and that this flow feature is successfully reproducible. For this reason, it is considered that the photographs of Fig. 3.28 are typical for the wave growth on the jet free-surface for increasing amplitude of the imposed disturbance. Unfortunately, there is no explicit relationship between the imposed excitation level onto the piezoelectric base and the disturbance amplitude of the jet velocity. Therefore, excitation levels are indicated by a RMS voltage value in Fig. 3.28 and only a qualitative comparison between simulations and experiments is then possible and will be limited to the description of tendencies in the observed jet behavior when increasing the excitation level.

Comparing the simulation results with the experimental ones, the best agreement is found for the calculated jet deformations with the velocity profile at the inlet obtained from the nozzle-flow simulation. As it has been found in the experiments, there exists an excitation level up to which the jet free-surface does not develop any bell-shaped form. This corresponds approximately to the RMS value of 38 mV of Fig. 3.28. An interesting phenomenon can be pointed out for this level of actuation: the free surface begins to deform, waves grow up before their amplitude starts diminishing. The same behavior is observed in the simulation results of Fig. 3.27 for the excitation amplitude of 16% with the velocity profile gained from the nozzle flow simulation. In this figure, waves start growing, but because of the jet centerline velocity being higher than the liquid velocity at the surface, the created waves start breaking backwards and enclose some of the surrounding gas, their amplitude being reduced as they propagate further downstream. The same behavior is observed in the three-dimensional simulation of Fig. 3.32. Unfortunately, this assumption could not be confirmed experimentally, since it is difficult to observe on the stroboscopic photographs any of the aforementioned gas enclosures which result from the wave breaking.

Concerning the simulation of the nozzle flow, no experimental results were available to the author at the time this thesis was written, so that the boundary conditions applied as well as the



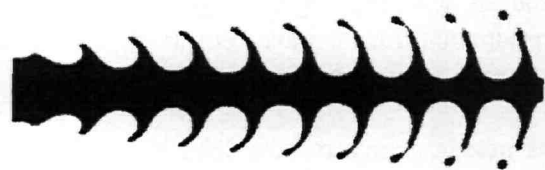
with simulated inlet velocity profile;
disturbance amplitude $\approx 8\%$; $St = 3.96$



with block profile at inlet; disturbance
amplitude = 8% ; $St = 3.96$



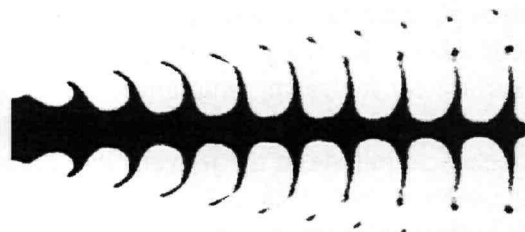
with simulated inlet velocity profile;
disturbance amplitude $\approx 16\%$; $St = 3.98$



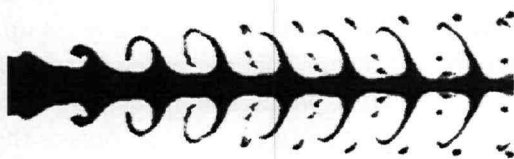
with block profile at inlet; disturbance
amplitude = 16% ; $St = 3.98$



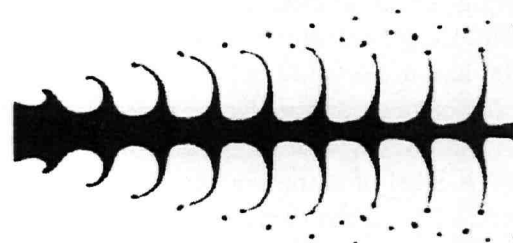
with simulated inlet velocity profile;
disturbance amplitude $\approx 24\%$; $St = 4.00$



with block profile at inlet; disturbance
amplitude = 24% ; $St = 4.00$



with simulated inlet velocity profile;
disturbance amplitude $\approx 32\%$; $St = 4.05$



with block profile at inlet; disturbance
amplitude = 32% ; $St = 4.05$

Figure 3.27: Cuts along the jet axis obtained for various disturbance amplitudes at nearly constant Strouhal number and for distinct inlet boundary conditions: an inlet profile obtained from the unsteady nozzle-flow simulation (left), a block profile modulated by a sine wave (right). Fluid flow is from the right to the left. Numerical grids have the same refinement level for capturing the free-surface position.

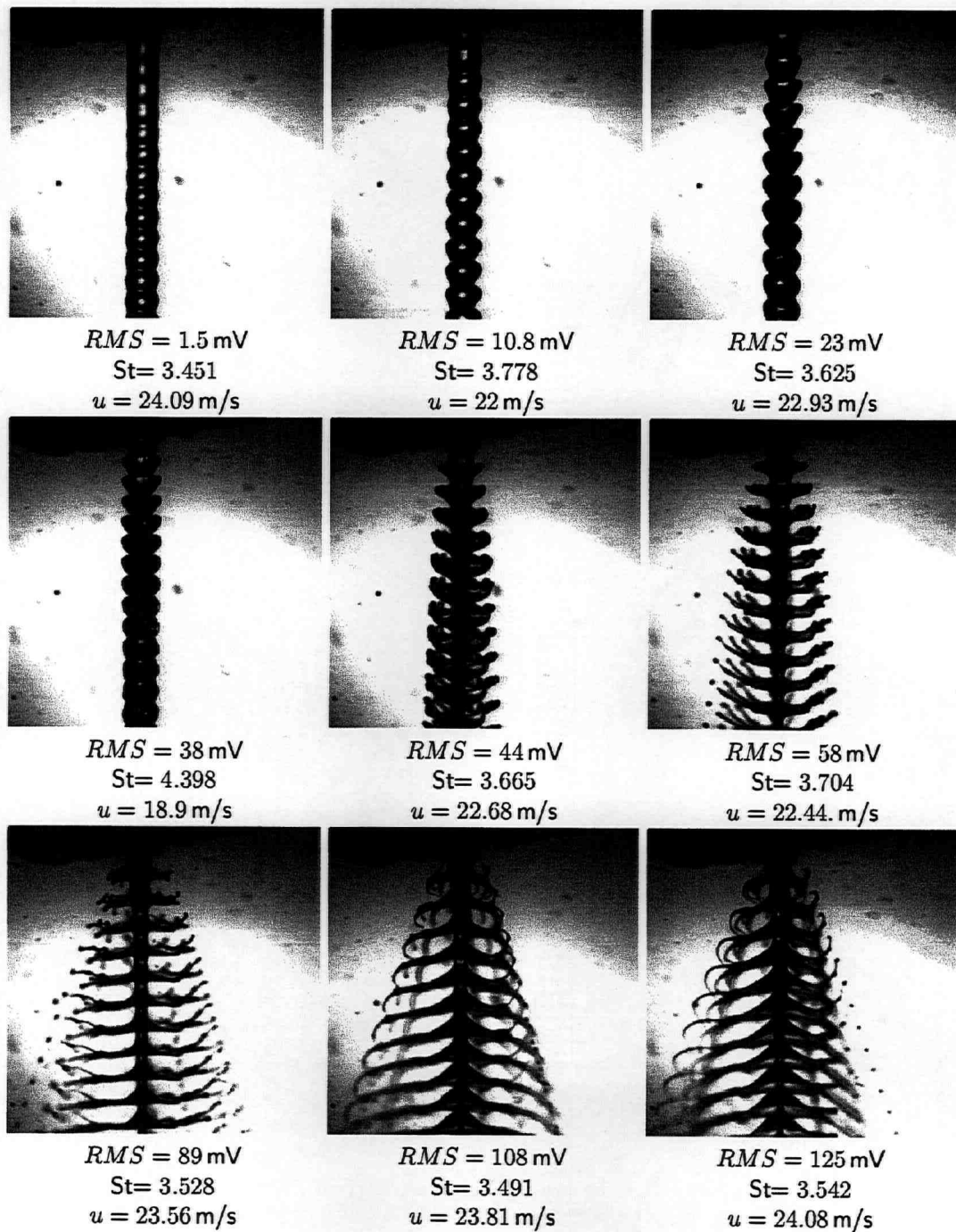


Figure 3.28: Stroboscopic photographs of the free-surface deformations of a jet of ethanoic alcohol under forced, periodical excitation at a frequency of 126 kHz (courtesy of IMFD, TU Bergakademie Freiberg, Germany). The excitation level increases from left to right and from left to bottom and is given by the RMS value of the input voltage. u indicates the mean nozzle outflow velocity and the jet issues from the nozzle at the top of each photograph.

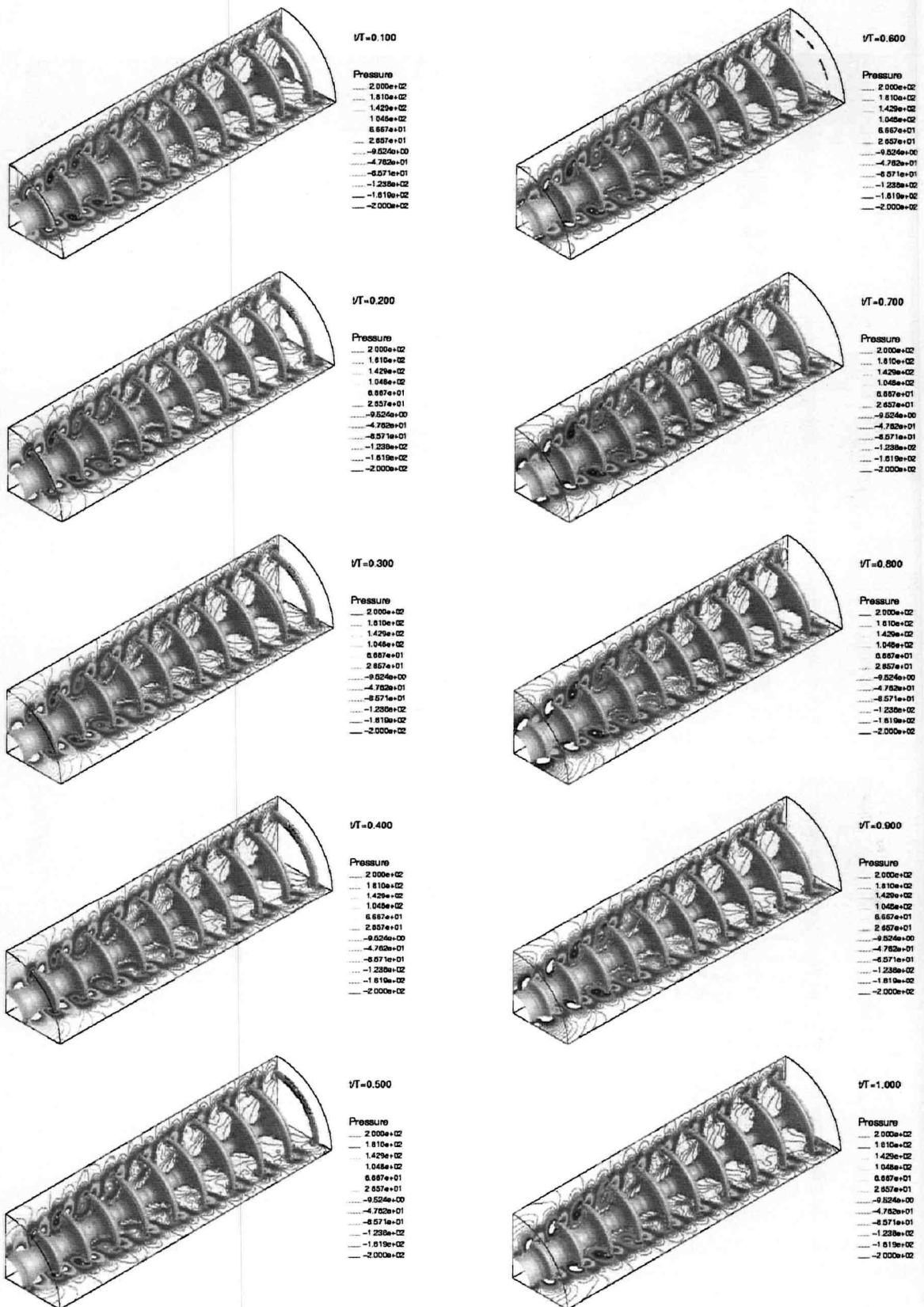


Figure 3.29: Jet free-surface deformation with pressure contours at different instants over an excitation period. Inlet velocity is obtained by the modulation of a block-profile. Excitation amplitude is $\epsilon_0 = 16\%$. Flow is from left to right.

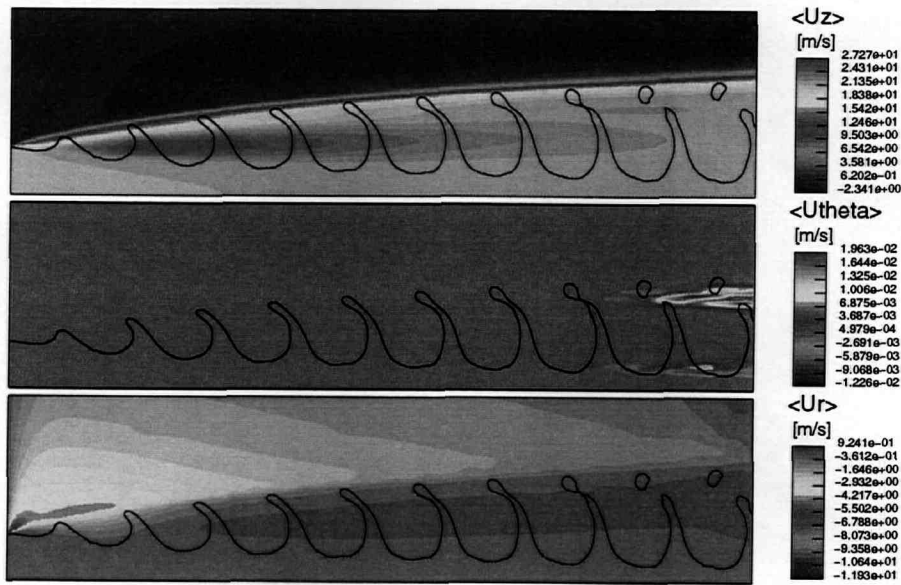


Figure 3.30: Time averaged velocity profile for both gas and liquid flow in the case of the modulated block profile of eq. (3.23). $\langle U_r \rangle$, $\langle U_{\theta} \rangle$ and $\langle U_z \rangle$ denote respectively the velocity components in radial, azimuthal and axial (streamwise) directions. The black line represents the instantaneous free-surface position in the midplane of the computational domain. Flow is from left to right.

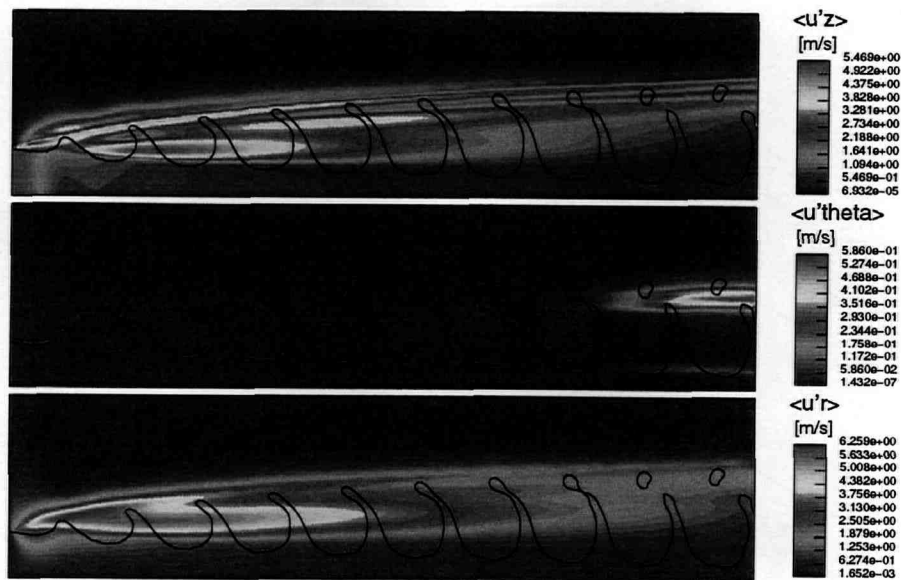


Figure 3.31: Time averaged profiles of the velocity fluctuations for both gas and liquid flow in the case of the modulated block profile of eq. (3.23). $\langle u'_r \rangle$, $\langle u'_{\theta} \rangle$ and $\langle u'_z \rangle$ denote respectively the root mean square (rms) values of the velocity components in radial, azimuthal and axial (streamwise) directions. The black line represents the instantaneous free-surface position in the midplane of the computational domain. Flow is from left to right.

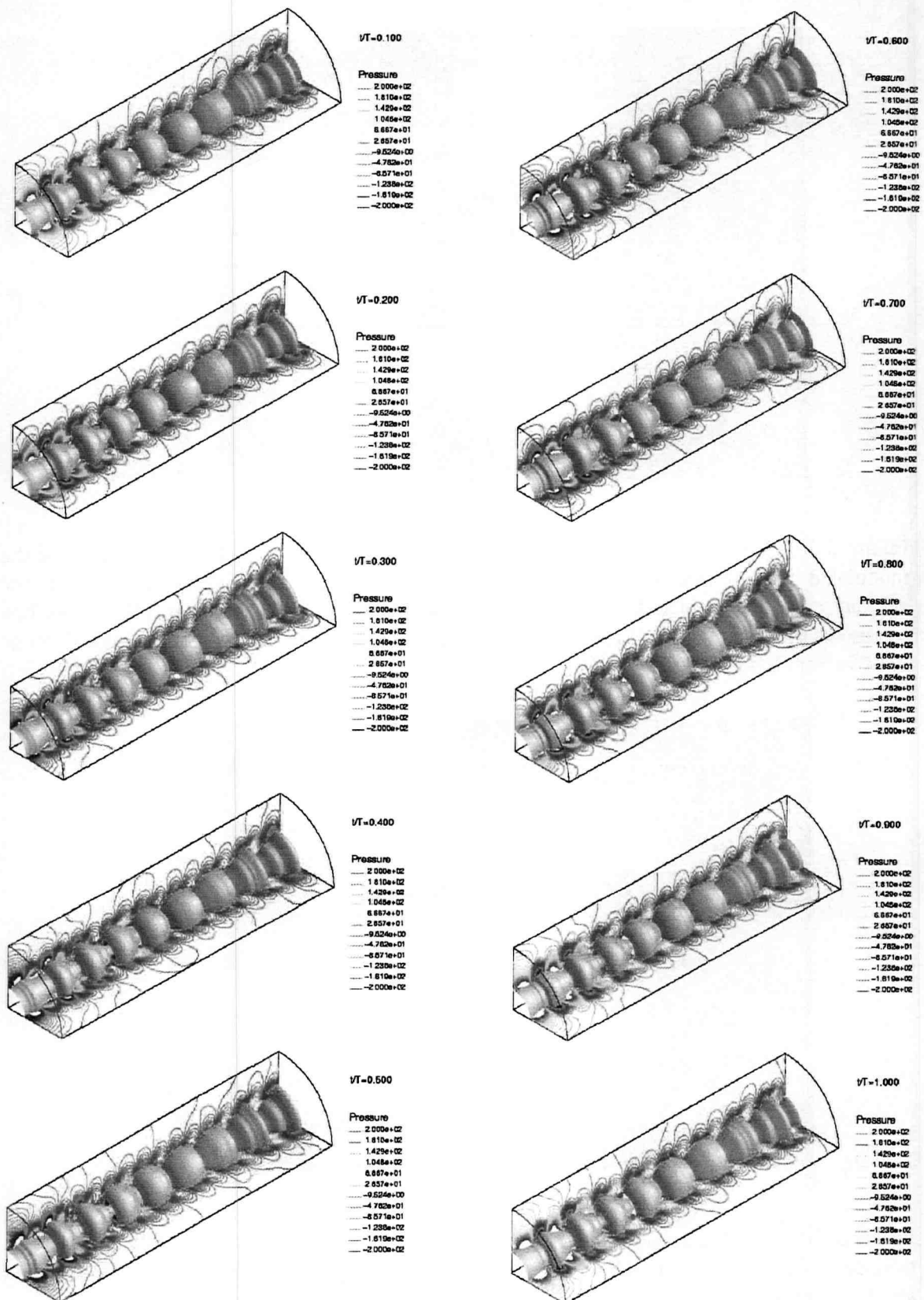


Figure 3.32: Jet free-surface deformation with pressure contours at different instants over an excitation period. Inlet velocity is obtained by the simulation of the nozzle internal flow. Flow is from left to right.

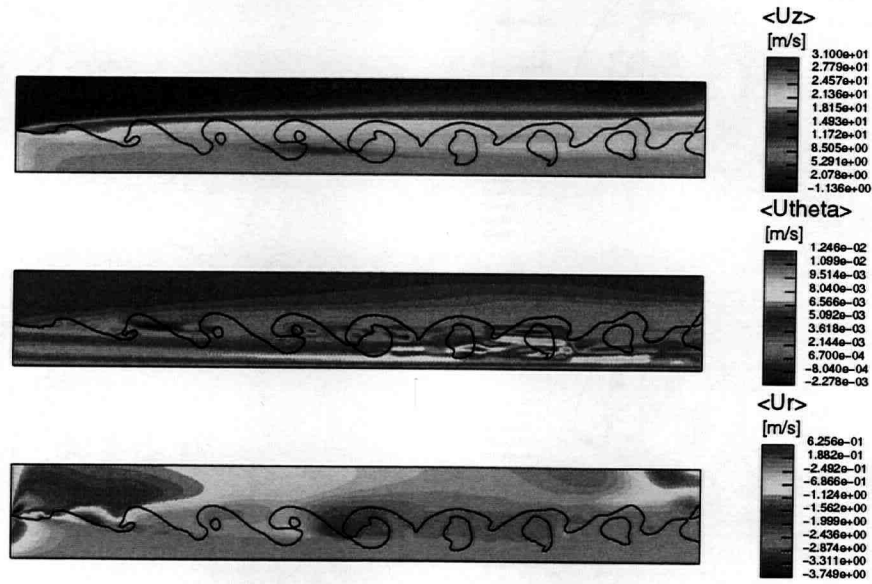


Figure 3.33: Time averaged velocity profile for both gas and liquid flow with inflow conditions gained from the nozzle simulation. $\langle U_r \rangle$, $\langle U_{\theta} \rangle$ and $\langle U_z \rangle$ denote respectively the velocity components in radial, azimuthal and axial (streamwise) directions. The black line represents the instantaneous free-surface position in the midplane of the computational domain. Flow is from left to right.

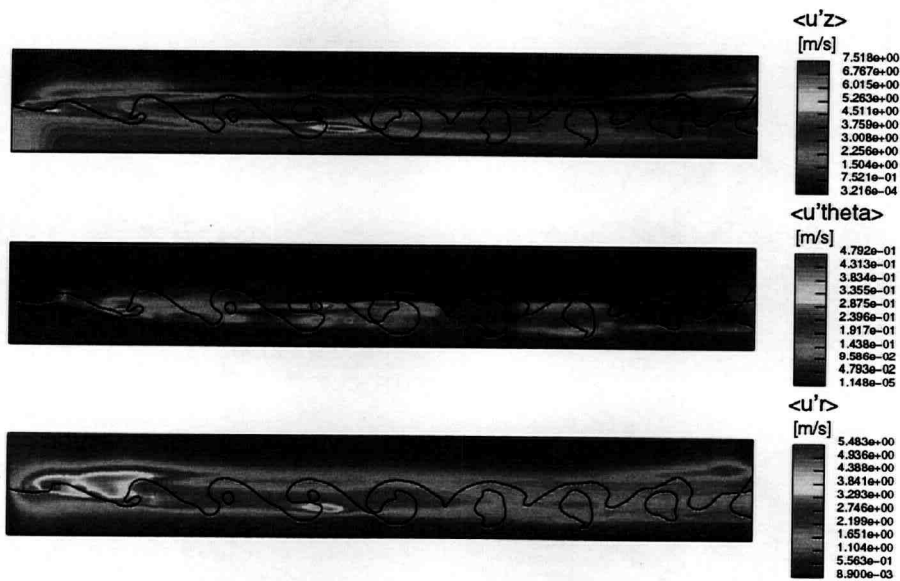


Figure 3.34: Time averaged profiles of the velocity fluctuations for both gas and liquid flow with inflow conditions gained from the nozzle simulation. $\langle u'r \rangle$, $\langle u'\theta \rangle$ and $\langle u'z \rangle$ denote respectively the root mean square (rms) values of the velocity components in radial, azimuthal and axial (streamwise) directions. The black line represents the instantaneous free-surface position in the midplane of the computational domain. Flow is from left to right.

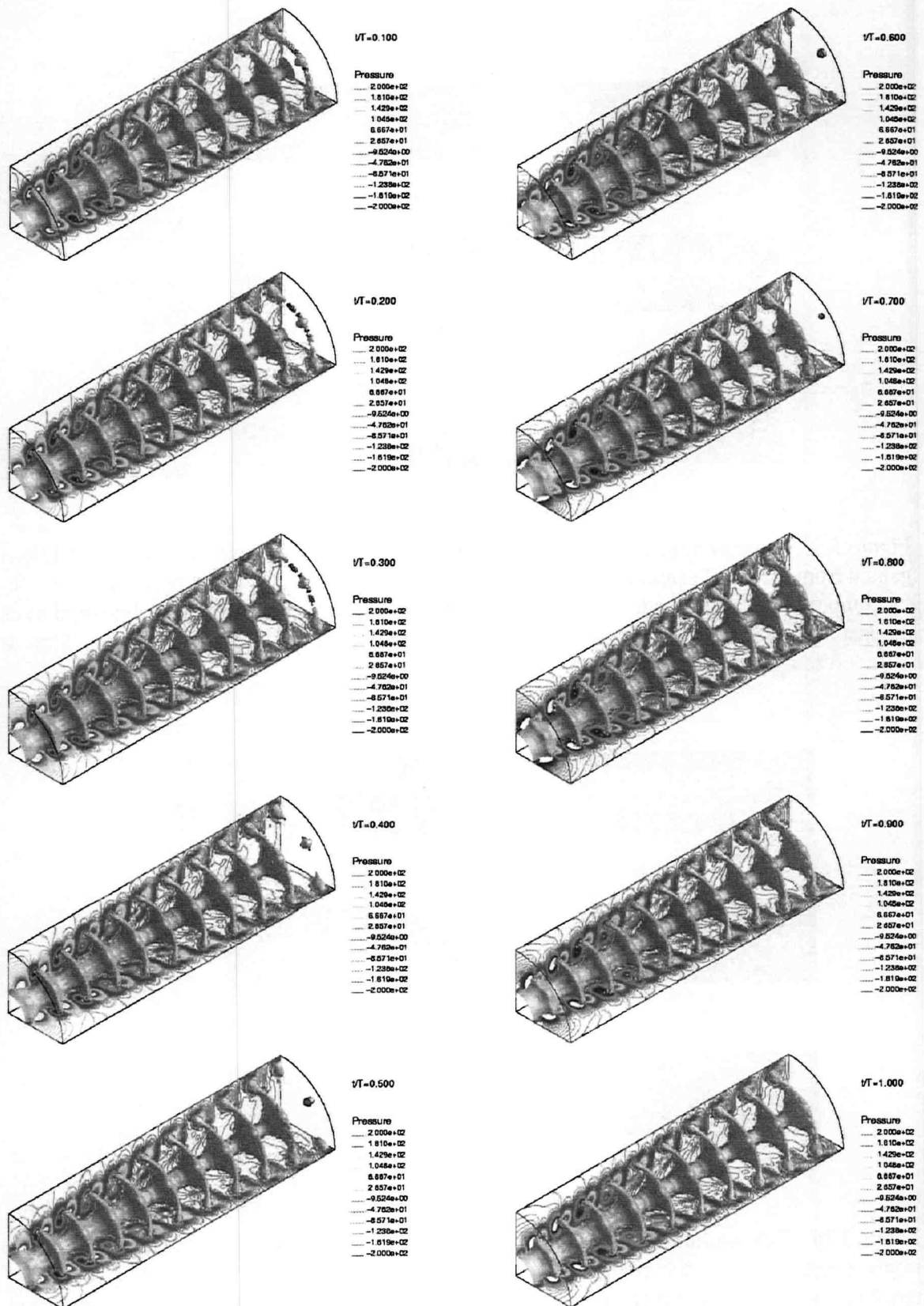


Figure 3.35: Jet free-surface deformation with pressure contours at different instants over an excitation period. Inlet velocity is obtained by a modulated block-profile with disturbances in azimuthal direction. Flow is from left to right.

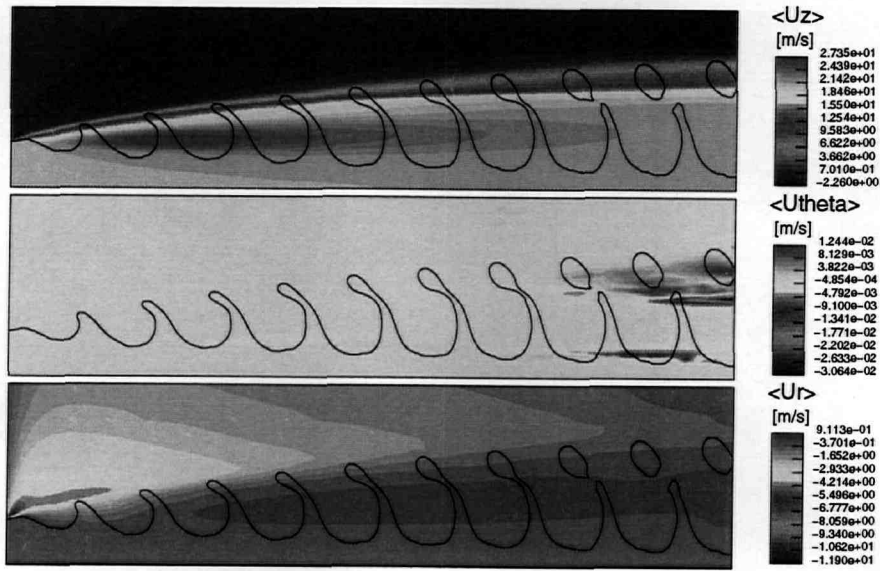


Figure 3.36: Time averaged velocity profile for both gas and liquid flow in the case the modulated block-profile with disturbances in azimuthal direction. $\langle U_r \rangle$, $\langle U_{\theta} \rangle$ and $\langle U_z \rangle$ denote respectively the velocity components in radial, azimuthal and axial (streamwise) directions. The black line represents the instantaneous free-surface position in the midplane of the computational domain. Flow is from left to right.

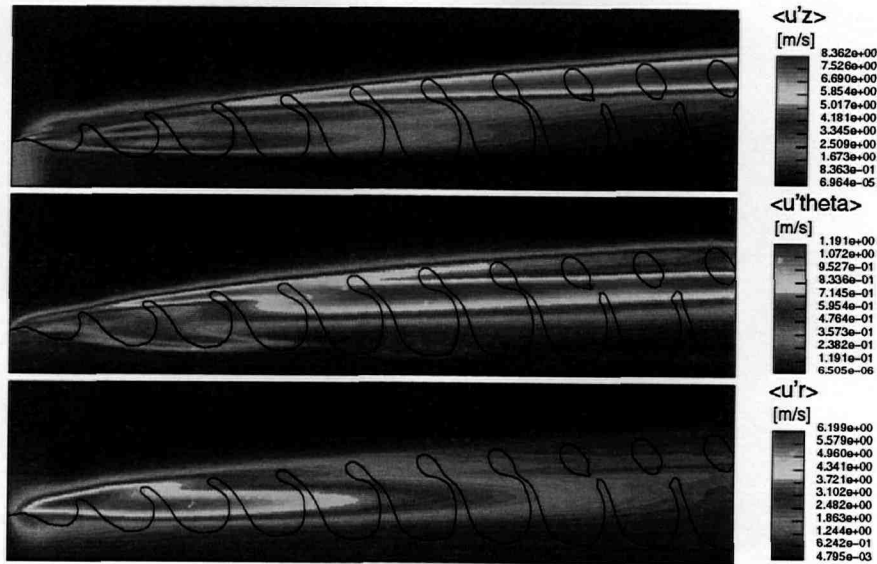


Figure 3.37: Time averaged profiles of the velocity fluctuations for both gas and liquid flow in the case the modulated block-profile with disturbances in azimuthal direction. $\langle u'_r \rangle$, $\langle u'_{\theta} \rangle$ and $\langle u'_z \rangle$ denote respectively the root mean square (rms) values of the velocity components in radial, azimuthal and axial (streamwise) directions. The black line represents the instantaneous free-surface position in the midplane of the computational domain. Flow is from left to right.

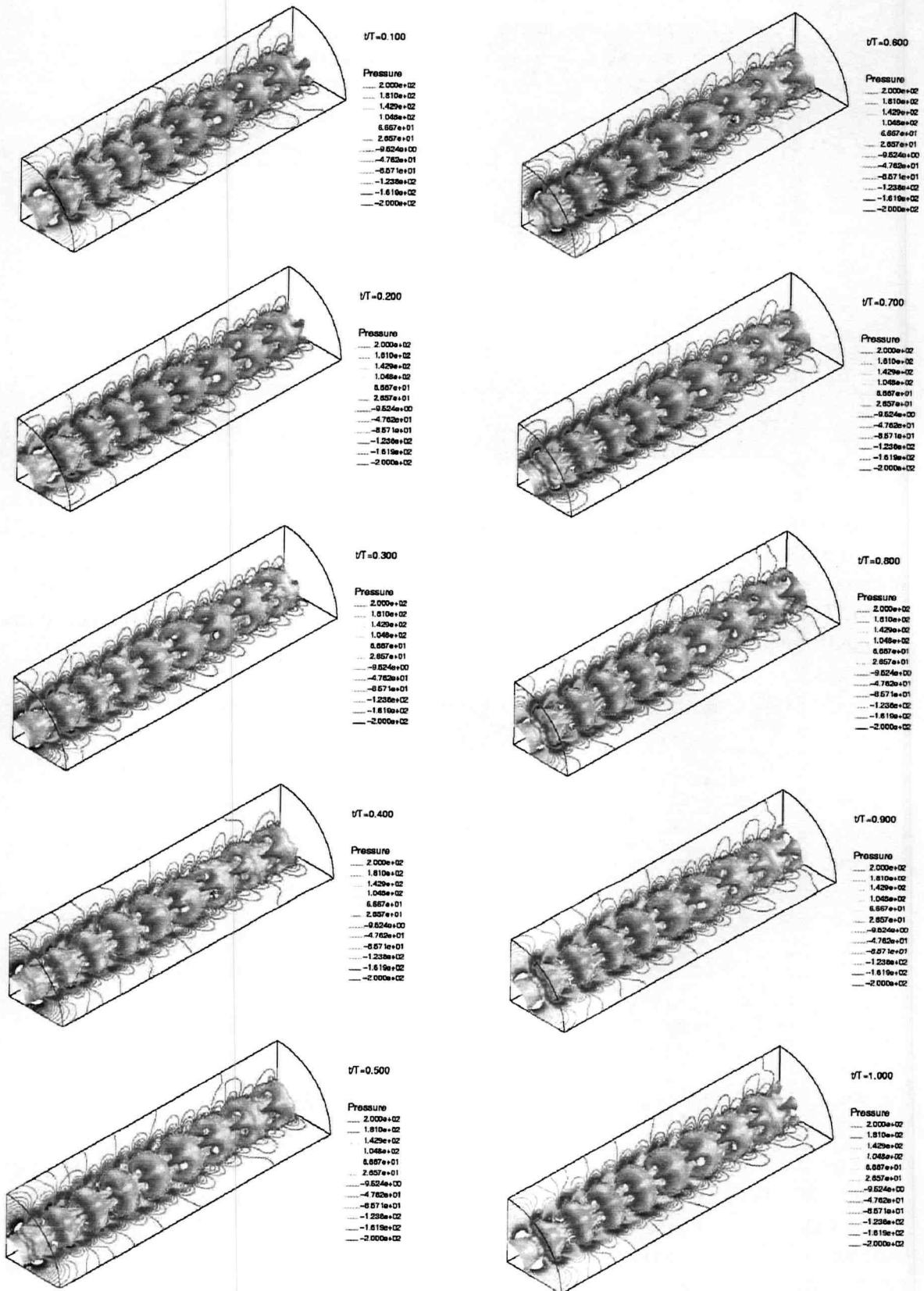


Figure 3.38: Jet free-surface deformation with pressure contours at different instants over an excitation period. Inlet velocity is obtained by the velocity profiles gained from the nozzle flow simulations with superposed disturbances in azimuthal direction. Flow is from left to right.

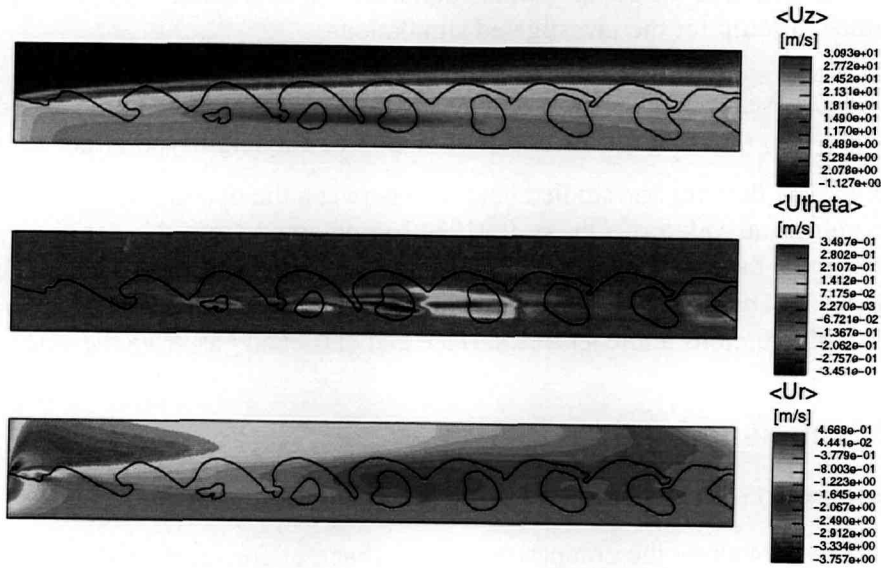


Figure 3.39: Time averaged velocity profile for both gas and liquid flow in the case of the nozzle flow with superimposed disturbances in azimuthal direction. $\langle U_r \rangle$, $\langle U_{\theta} \rangle$ and $\langle U_z \rangle$ denote respectively the velocity components in radial, azimuthal and axial (streamwise) directions. The black line represents the instantaneous free-surface position in the midplane of the computational domain. Flow is from left to right.

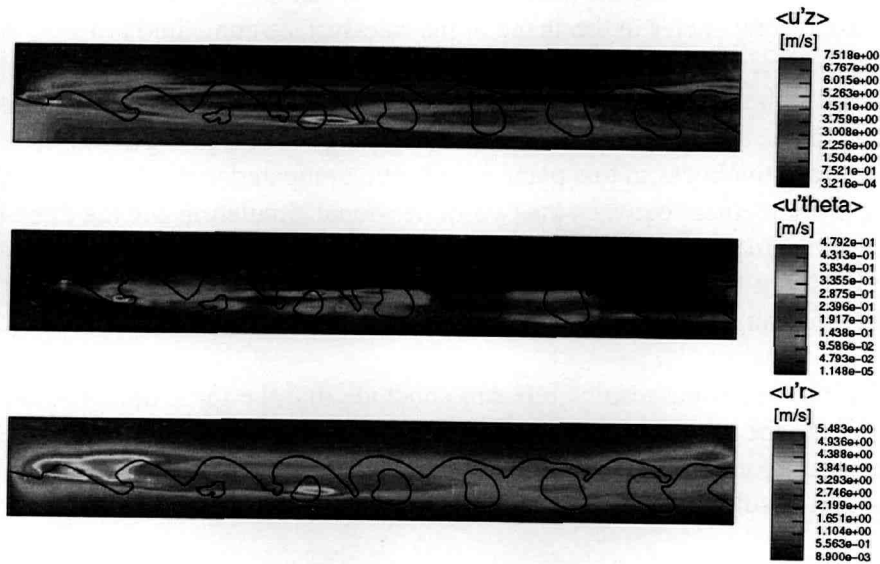


Figure 3.40: Time averaged profiles of the velocity fluctuations for both gas and liquid flow in the case of the nozzle flow with superimposed disturbances in azimuthal direction. $\langle u'_r \rangle$, $\langle u'_{\theta} \rangle$ and $\langle u'_z \rangle$ denote respectively root mean square (rms) values of the velocity components in radial, azimuthal and axial (streamwise) direction. The black line represents the instantaneous free-surface position in the midplane of the computational domain. Flow is from left to right.

geometrical definition of the computational domain must be considered as closest as possible to the experimental setup for the investigated simulations.

Defining the gas Weber number by $We_g = \frac{\rho_g U_m^2 D}{\sigma}$ and the Ohnesorge number of the liquid flow by $Oh = \frac{\mu_l}{(\rho_l D \sigma)^{1/2}}$, the criterion for the jet breakup of Rayleigh type is not satisfied ($We_g \approx 4.889 > 0.4$). The flow regime studied here falls between the bounds $13 > We_g > 1.2 + Oh^{0.9}$, where the numerical value of $Oh \approx 0.019642$ is obtained from the data of Table 3.4. For this flow regime – the so called wind-induced regime – the gas inertia sustains the jet breakup behavior [18,65]. This correlates very well with the simulation results obtained so far, for which both pressure fluctuations at the jet free surface and entrained gas drive the wave formation.

3.3.5 Discussion

Comparison of two-dimensional and three-dimensional simulations

Figures 3.41 to 3.44 show the comparison of the shape of free-surface deformations obtained in the two-dimensional and three-dimensional simulations. For all the simulations, excellent agreement is found concerning the wavelength of the disturbance as well as for the wave amplitude and for breakup behavior. Differences are found in Fig. 3.41 but only in the position and shape of the ejected fluid rings. In figure 3.43, discrepancies are also found, but in this case, the free-surface position for the three-dimensional model is given by a cut through a plane at $\theta=0$. On this plane, one obtains size and shape of the ejected droplets, due to the nature of the excitation, that are bigger than in the case of the simple actuation model of Fig. 3.41. The variation in size and in shape along the azimuthal direction can also be seen from Fig. 3.35. Figure 3.44 shows also discrepancies in the shape of the free-surface compared to Fig. 3.42, for which the agreement between two-dimensional and three-dimensional simulation is excellent. As the case of Fig. 3.43, the free-surface obtained in the three-dimensional simulation is given by a cut through the plane at $\theta=0$ and because of the fingering of the liquid-gas interface observed in Fig. 3.38, the wave thickness in this plane is different compared the axi-symmetric simulation. Nonetheless, the agreement between the two-dimensional simulation and the three-dimensional one is good: the same roll-up behavior is captured, wave amplitude and form correlate very well in the vicinity of the nozzle exit and the gas inclusions are located at the same places with approximately the same shape in both cases.

At the light of the presented results, one can conclude that the three-dimensional approach is only justified from the moment where disturbances in the azimuthal direction exist. In all other cases, if the simulation conducted here may allow a generalization, the two-dimensional simulation approach is sufficient for obtaining qualitatively adequate deformations of the jet free surface.

Comparison of numerical results with theoretical investigations

For high frequencies of the excitation, the wavelength of the disturbance at the free surface of a round laminar jet becomes smaller than the jet circumference and according to the Rayleigh theory (valid under the assumption of an incompressible, inviscid liquid jet in a gas of negligible density [84,89]) the jet free surface should not experience any kind of wave growth. However,

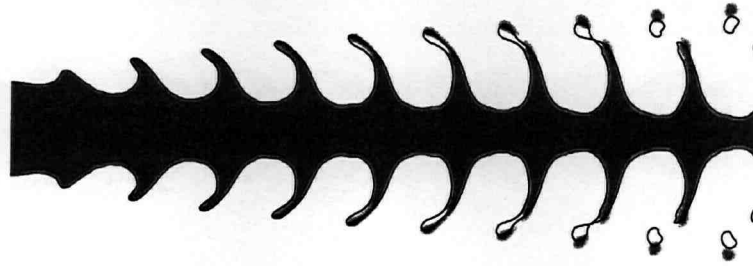


Figure 3.41: Comparison of the shape of the free-surface obtained with the two-dimensional simulation (contoured shape) and the one obtained with the three-dimensional simulation (black line). Both results use the simple actuation model from eq. (3.23).

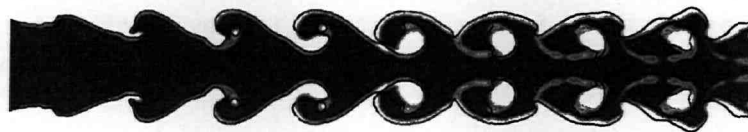


Figure 3.42: Comparison of the shape of the free-surface obtained with the two-dimensional simulation (contoured shape) and the one obtained with the three-dimensional (black line) simulation. Both results use the velocity profile gained from the resp. two-dimensional and three-dimensional nozzle simulation.

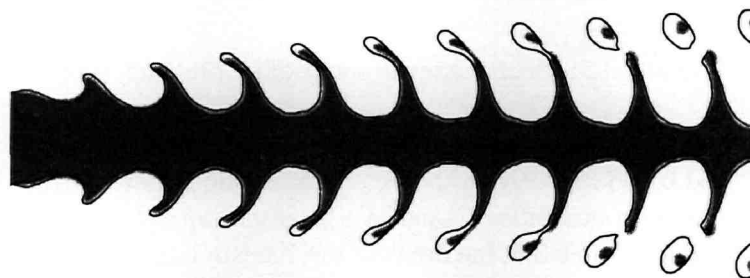


Figure 3.43: Comparison of the shape of the free-surface obtained with the two-dimensional simulation (contoured shape) and the one obtained with the three-dimensional simulation (black line). The two-dimensional simulation uses the simple actuation model of eq. (3.23), the three-dimensional one uses the actuation with additional disturbances of eqs. (3.24) and (3.25).

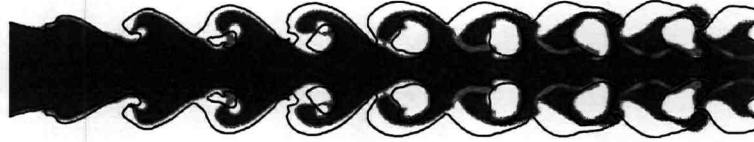


Figure 3.44: Comparison of the shape of the free-surface obtained with the two-dimensional simulation (contoured shape) and the one obtained with the three-dimensional simulation (black line). The two-dimensional simulation uses the velocity profiles gained from the two-dimensional nozzle flow simulation, whereas the three-dimensional simulation uses the velocity profiles of the 3D nozzle simulation with additional disturbances of eqs. (3.24) and (3.25).

wave growth is observed in both simulations and experiments and another mechanism has to be found in order to explain the jet free-surface behavior for wavelengths that are shorter than the jet perimeter. According to the work of Lin & Lian [63], the instability mechanism must be of convective nature and it must be distinguished between three major mechanisms for the onset of jet breakup. Defining the liquid Weber number $We = \sigma / \rho_l U^2 r_0$, where U is the jet velocity and r_0 the undisturbed jet radius, the gas to liquid density ratio $Q = \rho_g / \rho_l$ and the Reynolds number $Re = Ur_0 / \nu_l$, the mechanisms of breakup onset can be summarized according to Table 3.5.

Mechanism	Characteristic length	Parameter range
Capillary pinching	r_0	$Q \ll We$
Pressure fluctuations	$(We/Q)r_0$	$We \ll Q < 1$ $Q < We$
Shear waves	$26180 r_0 (\nu_g / \nu_l) / Re$	$Q > We$

Table 3.5: Mechanisms of onset of jet breakup, [63]

For the present simulations, with the data of Tab. 3.4, the values obtained for Q and We are resp. $1.5057 \cdot 10^{-3}$ and $6.898 \cdot 10^{-4}$, using the jet characteristic outlet velocity of 21 m/s and diameter of 0.205 mm. Both quantities Q and We have the same order of magnitude and it is expected that, according to Table 3.5, the breakup mechanism is essentially driven by two kinds of mechanisms: capillary pinching and pressure fluctuations. One can argue that, also according to Table 3.5, shear waves at the gas-liquid interface must play an active role. In the latter case, the characteristic length of the disturbance is given by $26180 r_0 (\nu_g / \nu_l) / Re$, which turns out to have a numeric value of approx. $184.03 r_0$, whereas the wavelength of the imposed disturbance is approx. $1.5873 r_0$. Therefore, the instability mechanism related to the shear waves is not relevant.

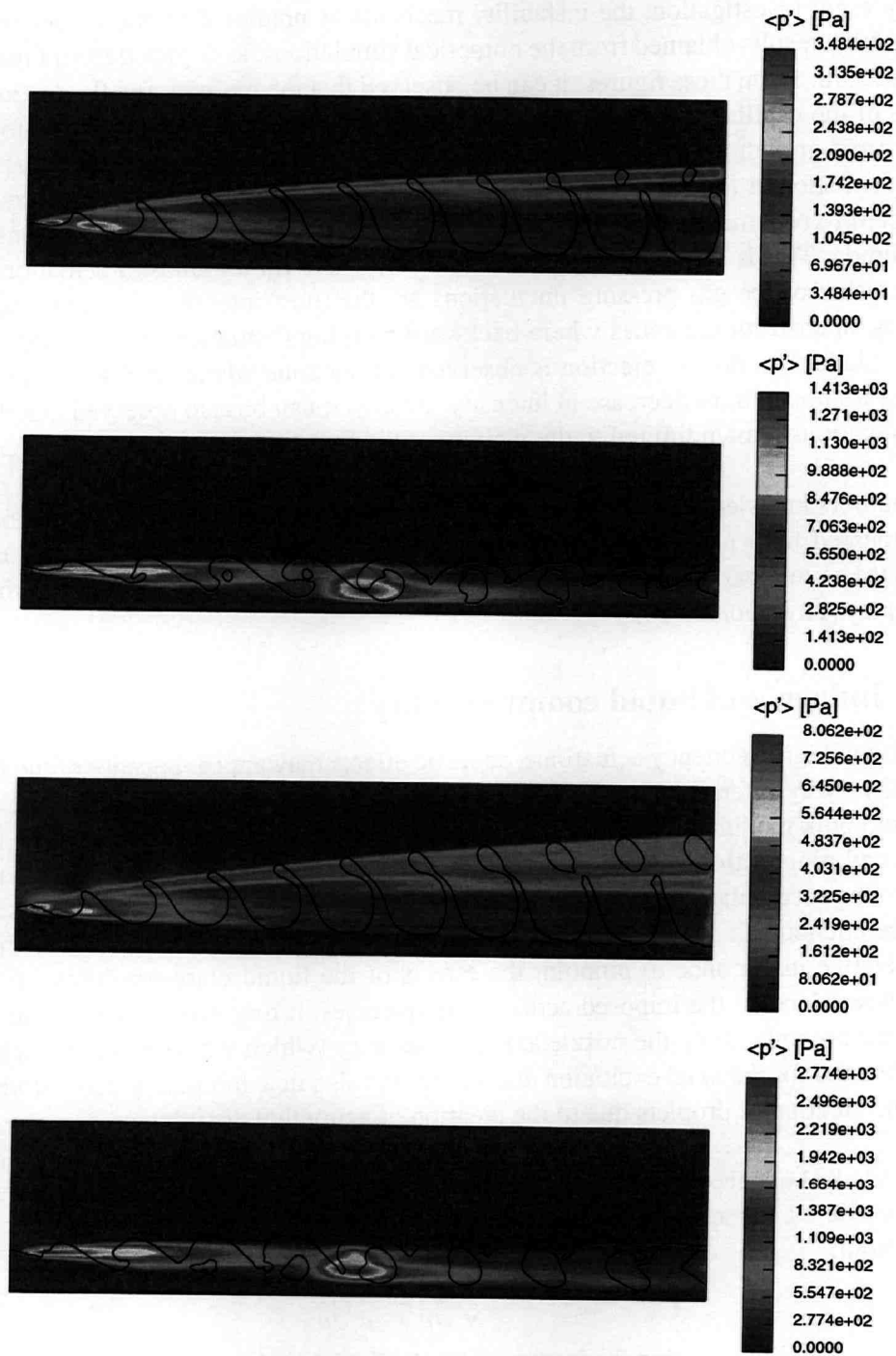


Figure 3.45: Time-averaged values of the gas pressure fluctuations $\langle p' \rangle$ for the four different types of jet actuations investigated. From top to bottom: simple actuation model from eq. (3.23), actuation with the velocity profile gained from the nozzle simulation, simple actuation model with additional azimuthal disturbances of eqs. (3.24) and (3.25), actuation with the nozzle velocity profiles and superimposed azimuthal disturbances of eqs. (3.24) and (3.25). The black line shows the instantaneous position of the jet free surface for the corresponding actuation level.

In the present investigation, the instability mechanisms predicted by the theory correlate very well with the results obtained from the numerical simulations, as depicted from Figs. 3.29, 3.32, 3.35 and 3.38. From these figures, it can be observed that the gas pressure fluctuations assist the process of the capillary pinching in the vicinity of the inlet boundary and they are responsible for the rapid growth as well as the steepness of the waves at the jet free-surface, partly due to vortex formation at the wave edge. After some distance from the inlet boundary, convective forces start to become the major driver of the flow pattern, the pressure fluctuations decreasing in amplitude. This can also be seen on Fig. 3.45, where for all kinds of actuation types used, the rms-value of the gas pressure fluctuations are the most intense in the zone near the inlet boundary, apart from the zones where backward merging (actuation obtained from the nozzle flow simulation) or droplet ejection is observed. In the zone where convection dominates, the gas pressure fluctuations decrease in intensity. Finally, it can be also observed that the gas pressure fluctuations remain limited to the vicinity of the free-surface.

To the authors knowledge, this is the very first time that the theory of Lin & Lian [63] has been complemented by a numerical simulation. The results obtained in the present investigation validate the numerical method employed herein for this particular kind of flows where surface tension plays an important role.

3.3.6 Influence of liquid compressibility

In the case of high-frequency actuations, acoustic effects may appear because of the liquid compressibility. Very often the liquid compressibility can be neglected, because of the high value of the fluid bulk modulus. But, in some cases, like for the flow within a cavity, the finite value of the sound propagation velocity can lead, at some frequencies (depending also on the cavity shape), to the accumulation and amplification of pressure waves, which corresponds to acoustic resonance phenomena. For the nozzle flow investigated in previous sections of this chapter, it is of relative importance to pinpoint the effects of the liquid compressibility on the nozzle internal flow, since, at the imposed actuation frequencies, it may be resonated. The resonance may appear not only along the nozzle axis of symmetry (which would explain that high levels can be obtained for the axial excitation amplitude) but also in azimuthal direction (which would sustain the creation of droplets due to the creation of azimuthal disturbances).

For a liquid, the bulk elasticity K is a physical parameter which determines the volume decrease of the considered substance due to a pressure increase, [34]. By definition, the following relations hold:

$$K = -\frac{1}{v} \frac{\partial v}{\partial p} = \frac{1}{\rho} \frac{\partial \rho}{\partial p} \quad (3.26)$$

For a liquid, assuming also that the isothermal and adiabatic values of the bulk elasticity remain the same in the application range presented hereafter, one can obtain the sound celerity c_ℓ in the liquid only by the knowledge of K and the fluid density. By definition:

$$c_\ell^2 \stackrel{\text{def.}}{=} \frac{\partial p}{\partial \rho} \quad (3.27)$$

And, as a matter of consequence:

$$c_\ell = \frac{1}{\sqrt{K\rho}} \quad (3.28)$$

ρ [kg m ⁻³]	K [m kg ⁻¹ s ²]	c_ℓ [m s ⁻¹]
789	1.1 10 ⁻⁹	1073.4

Table 3.6: Physical properties of ethanol to be used for compressibility analysis.

In the assumption of small pressure fluctuations and small density variations of a fluid for which viscosity effects can be neglected, one can define a velocity potential φ for which the Navier-Stokes equations degenerate into the form [52]:

$$\frac{\partial^2 \varphi}{\partial t^2} - c_\ell^2 \Delta \varphi = 0 \quad (3.29)$$

This is the *wave equation* for sound propagation in a fluid. Assuming that φ depends only on one spatial coordinate x , the Laplacian operator Δ can be replaced by the second derivative in space with respect to x and one obtains then for φ the following equation:

$$\frac{\partial^2 \varphi}{\partial t^2} - c_\ell^2 \frac{\partial^2 \varphi}{\partial x^2} = 0 \quad (3.30)$$

A general solution to this equation can be seen as the superposition of monochromatic waves of the form (by decomposition of the general solution onto the Fourier space):

$$\varphi = \Re \{ A e^{i(\pm kx - \omega t)} \}, \quad (3.31)$$

where A is a complex argument and k is the so-called wave number related to the wavelength λ and the frequency ω by:

$$k = \frac{\omega}{c_\ell} = \frac{2\pi}{\lambda} \quad (3.32)$$

A particular version of the general solution of eq. (3.31) is the standing wave of the form:

$$\varphi = B \cos(kx) \sin(\omega t) \quad (3.33)$$

This particular solution is obtained as the superimposition of a forward traveling ($+kx$) and a backward traveling ($-kx$) wave. This can happen when, due to geometrical constraints, the forward traveling wave is reflected at some boundaries. If standing waves are, for a given calculation domain, solution of the wave equation, it is very likely that this wave is going to be amplified. In this case, the frequency ω is called *the resonance frequency* and the spatial variation of the solution ($B \cos(kx)$) is called *the resonance mode*.

A simple analysis based on the sketch depicted by Fig. 3.46 shows that a resonance frequency is to be expected for the nozzle geometry investigated previously, with a mode in axial direction. For the mode sketched by Fig. 3.46, the estimated wavelength of the resonance mode is one third of the nozzle length L . Using the physical data of Table 3.6, the corresponding resonant frequency is given by:

$$f = \frac{c_\ell}{\lambda} = \frac{3}{L\sqrt{K\rho}} \approx 127787 \text{ Hz} \quad (3.34)$$

The value so obtained lies within the range in which both experiments and simulations have been conducted.

Because of the crude approximation made here for estimating the frequency of a particular mode, an analysis of the nozzle cavity has been performed using the program LMS Sysnoise, [66]. The program is designed to perform acoustical analyses and allows among others to obtain for a cavity both resonance modes and frequencies. Using the input of Table 3.6 and looking only for the frequency range 120 to 130 kHz, one obtains among others the two solutions depicted by Figs. 3.47 and 3.48. The numerical grid used for the simulations involved 30,000 control volumes which gives for the acoustical analysis performed a fairly accurate estimate of the resonance modes and frequencies. Even if other resonant modes exist (there exist 17 others at lower frequencies), only the ones depicted in Figs. 3.47 and 3.48 have been retained, since they have about the same frequency as the one used in the experiments of the IMFD and the simulations presented here. It should be pointed out here that both frequencies captured are narrow (126,670Hz vs. 127,368Hz) and it can be expected that both respective modes may appear during the process of actuation at the imposed frequency of 126kHz. This will then lead to an increase of the excitation level, so that a bell-shaped wave train can develop on the jet-free surface, but also to an azimuthal disturbance which will be eventually responsible of droplet ejection.

In order to check if both resonant modes of Figs. 3.47 and 3.48 can also be obtained with the present numerical method, a coarse three-dimensional numerical grid has been built involving 223,552 control volumes, Fig.3.49. Since the working fluid is assumed to be a compressible liquid, this feature had to be accounted for in the numerical simulation. The numerical method implemented in the flow solver is based on a modified SIMPLE method for pressure-density-velocity coupling when considering compressible flows, [25]. For closing the extended equation system, it is necessary to introduce an equation of state for the fluid – $\rho = \rho(p, T)$ – as well as to give the variations of density according to pressure changes (i.e. the quantity $\partial\rho/\partial p$). Considering that the fluid experiences such small variations of density and pressure that the expansion and compression processes can be considered as isothermal, eq. (3.26) allows by integration to obtain an equation of state for the fluid:

$$K = \frac{1}{\rho} \frac{\partial\rho}{\partial p} \Rightarrow \frac{\partial\rho}{\rho} = K \partial p \Rightarrow \rho = \rho_0 e^{K(p-p_0)}, \quad (3.35)$$

where ρ_0 is the reference density at the reference pressure p_0 ². The quantity $\partial\rho/\partial p$ is then obtained by derivation of eq. (3.35):

$$\frac{\partial\rho}{\partial p} = \rho_0 K e^{K(p-p_0)}. \quad (3.36)$$

This model for the density variations has been used on the computational mesh presented on Fig. 3.49. For the simulations undertaken, the same actuation model as for the investigations of the nozzle internal flow has been used (see also eq. (3.19)). The actuation frequency was set again to 126kHz and 300 time-steps for one period of actuation were used. The boundary conditions remained the same as in the case of the three-dimensional, incompressible nozzle model. The simulation was run transient for 100,000 time steps so that a periodical flow can

²The obtained expression of eq. (3.35) degenerates to the linear variation of the density according to pressure $\rho/\rho_0 = 1 + K(p - p_0)$ if one assumes $p - p_0 \ll p_0$ and one retains terms up to the first order of the integer series development of the exponential function, hence $e^x = 1 + x + O(x^2)$. This kind of expression is widely used for obtaining the sound velocity in fluids.

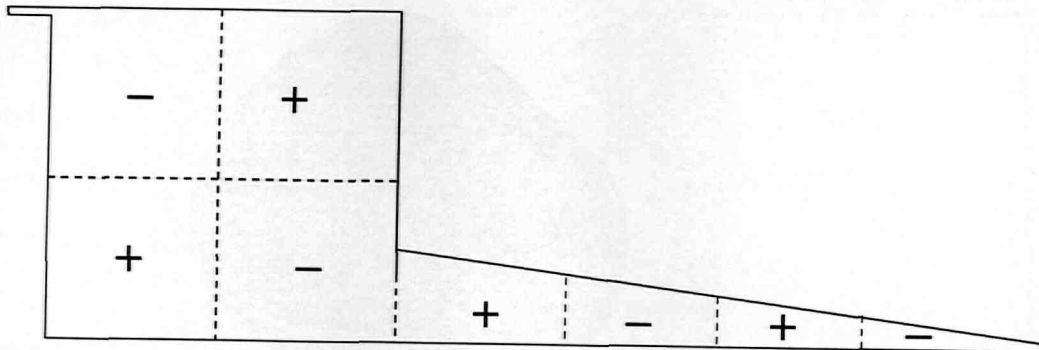


Figure 3.46: Estimated resonance mode for the investigated nozzle geometry. The dashed lines denote the modal lines of zero amplitude, the + signs the locations of crests and the - signs the locations of troughs.

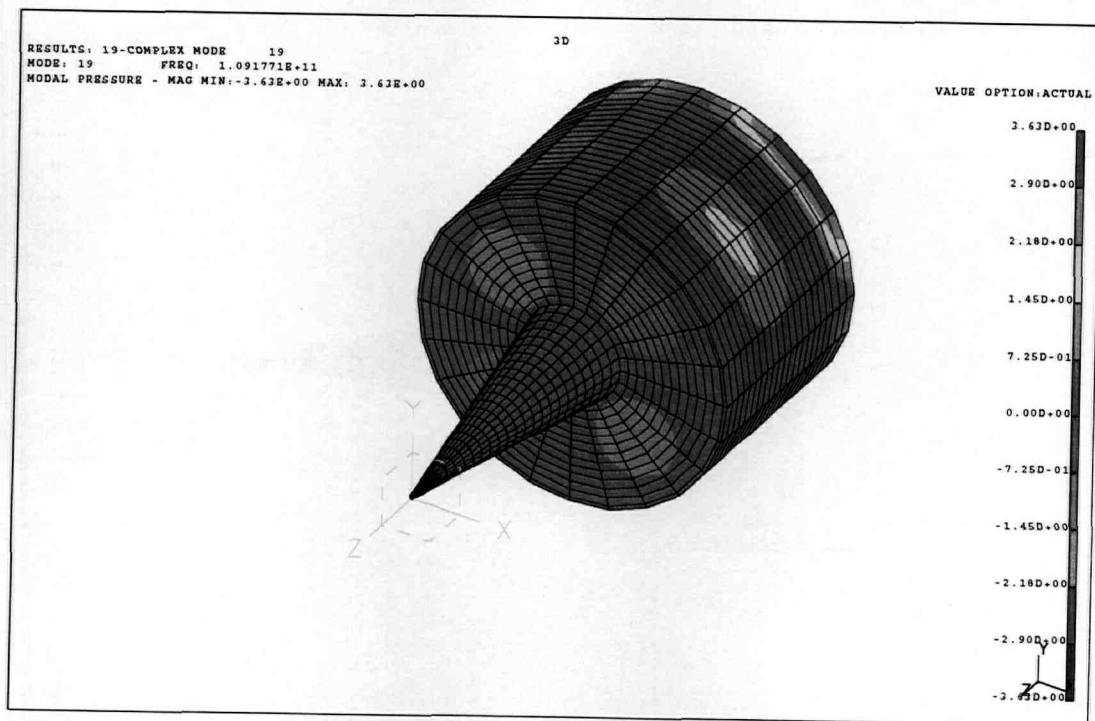


Figure 3.47: Superposition of numerical mesh used for the analysis and resonance mode at the frequency $f=127.368$ kHz.

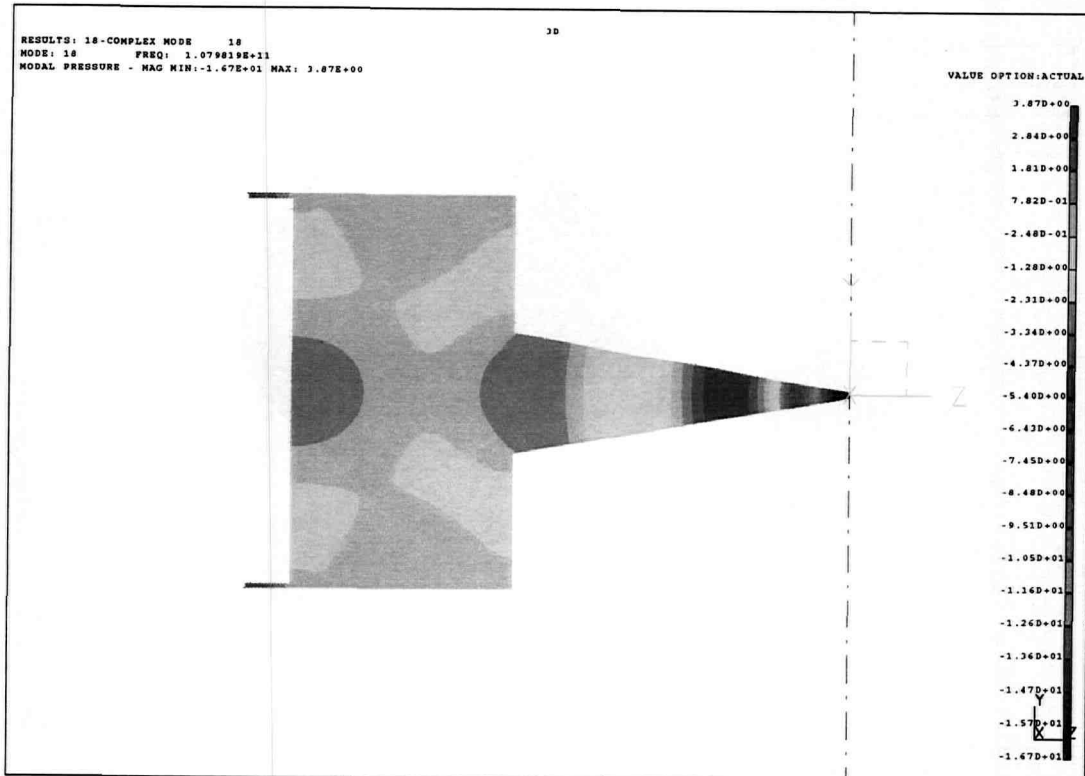
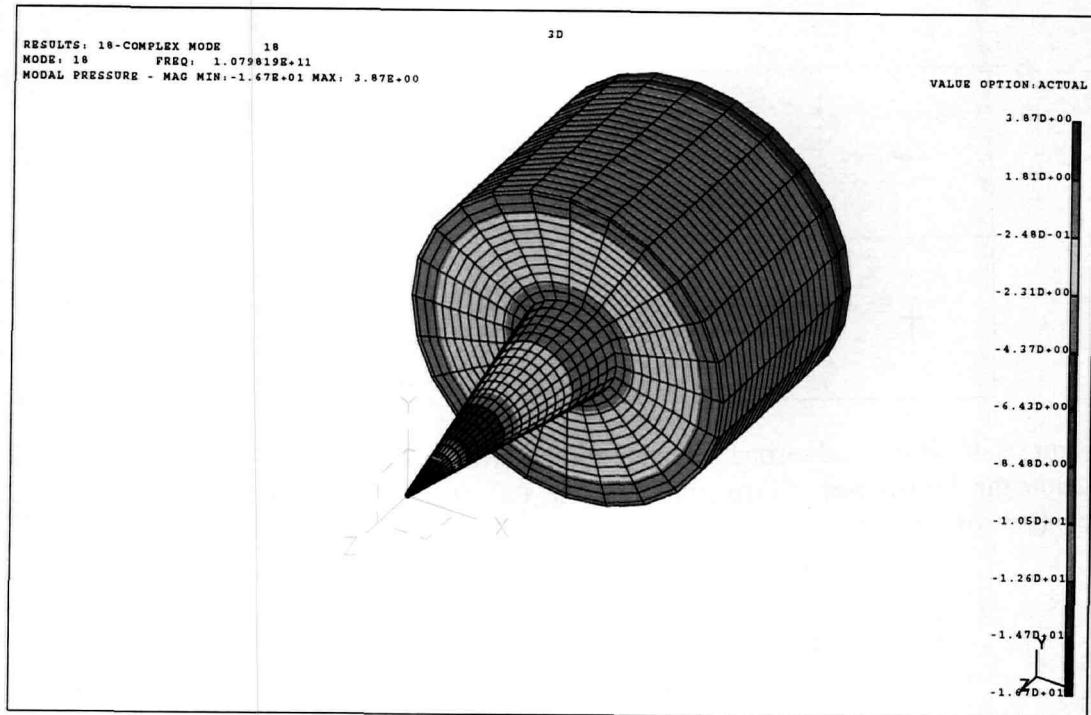


Figure 3.48: Resonance mode at frequency $f=126.670$ kHz: Superposition of numerical mesh used for the analysis and modal pressure (top), cut through the nozzle midplane showing the distribution of the modal pressures (bottom).

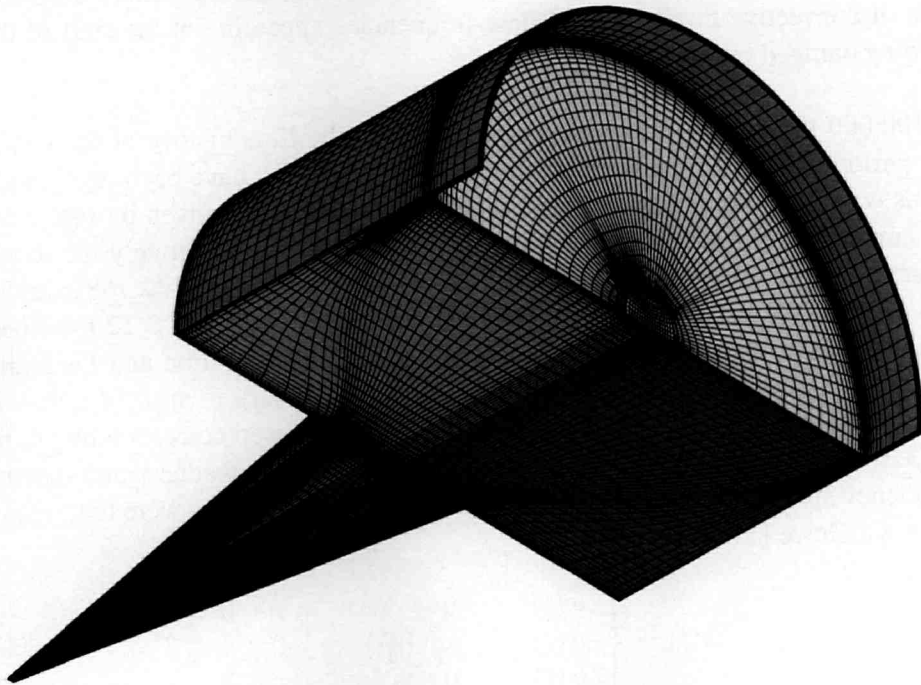


Figure 3.49: Numerical grid used for the compressible simulation of the nozzle internal flow. Only the half of the entire model is used and for recovering the complete model, a pair of periodic boundary conditions is used, depicted in blue and magenta on the figure.

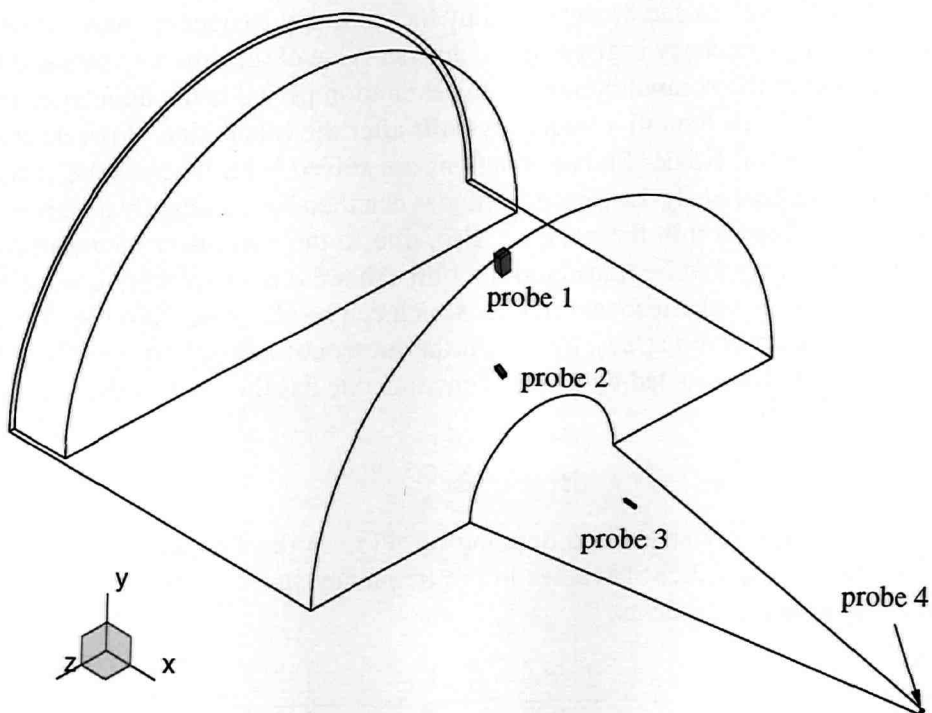


Figure 3.50: Location of the probes within the computational domain, used for registering the time signals of pressure and velocity.

establish in the nozzle. Because of the high amount of central-differences used for the approximation of convective fluxes (100%), low-frequencies appearing at the start of the simulation were being damped out only slowly.

After 100,000 time steps, it has been assumed from the time history of the residuals that the flow is periodic and the time signals of pressure and velocity have been registered at 4 distinct locations within the computational domain. These locations are given by Fig. 3.50. The number of samples taken was chosen to be big enough to capture accurately the lower part of the frequency spectrum of the registered time signals. With a number of 32,768 samples, the power spectra of pressure and azimuthal velocity shown in Fig. 3.51 and 3.52 have been obtained. Unfortunately, the registered time-signal has a finite length in time and the start and ending values may not necessarily be the same, so that it is necessary to apply a time-window to the observed signal. Here the Welch time-window has been chosen corresponding to the definition of eq. (3.37), because of its very good compromise between peakedness and spectral leakage in the frequency space [98]. The resulting discrete Fourier transforms were then realized with the software XmGrace [110].

$$w(t) = \begin{cases} w(t) = 0 & ; & t < 0 \\ w(t) = \sin\left(\frac{\pi t}{T}\right) & ; & 0 \leq t \leq T \\ w(t) = 0 & ; & t > T \end{cases} \quad (3.37)$$

From Fig. 3.51, it can be seen that there exists a dominant frequency centered on $f_0=125,749$ Hz for all pressure probes. This corresponds to the frequency of the imposed disturbance, here 126 kHz and is 0.7% off of the predicted resonance frequency for the axial mode of Fig. 3.48. The difference in the values can be explained by the sampling frequency used during the simulation. The sampling frequency is given by the inverse value of the time step size and because of the finite precision of the computer algebra, the excitation period is not an integer value of the time step size. This leads then to a frequency-shift after the calculation of the discrete Fourier transform. Also, the full Navier-Stokes equations are solved here, whereas the program SYS-NOISE performs a linear analysis. Resonant modes can then have a slightly different frequency due to the viscous flow within the nozzle. Also, due to the non-linear nature of the Navier-Stokes equations, energy can be transferred not only from the main excitation frequency to the higher but also to lower-order resonant modes, which can be observed from Fig. 3.51, in which frequency peaks are observed at $2f_0, 3f_0 \dots$. Furthermore, considering eq. (3.29) and applying to it a burst in time to be modeled by a Dirac function, one has then to find the solution of:

$$\frac{\partial^2 \varphi}{\partial t^2} - c_t^2 \frac{\partial^2 \varphi}{\partial x^2} = \delta(t) \quad (3.38)$$

Switching to the frequency space and defining by $\hat{\Phi}(x, \omega)$ the Fourier transform of $\varphi(x, t)$, the time derivative of eq. (3.38) becomes in the frequency space $-\omega^2 \hat{\Phi}(x, \omega)$ and eq. (3.38) rewrites after some rearrangements:

$$\hat{\Phi} + \frac{1}{k^2} \frac{\partial^2 \hat{\Phi}}{\partial x^2} = -\frac{1}{\omega^2} = -\frac{1}{4\pi^2 f^2} \quad (3.39)$$

From eq. (3.39), apart from the resonance phenomena, it can be deduced that at a given location, the slope of the frequency spectrum is proportional to f^{-2} . This is exactly the slope obtained

on Figs. 3.51 and 3.52. It can be concluded that the physical model introduced with eq. (3.35) combined with the numerical solution of the Navier-Stokes equations is able to capture the physics described by the wave equation describing sound propagation.

In order to compare the pressure fluctuations resulting from the simulation with the modal/acoustic analysis of the SYSNOISE software, the density fluctuations at a frequency of $f_0=126,670$ Hz have been filtered out by calculating over the same period of time for each cell the integral value of the density times $\cos(2\pi f_0 t)$. These fluctuations are depicted by Fig. 3.53 and are in very good agreement with the resonant mode of Fig. 3.48. Nevertheless, the position and amplitude of crest and trough are slightly different in Fig. 3.53, which can be inferred to the use of a much finer mesh in the numerical flow simulation than in the acoustical analysis (223,552 control volumes for one half of the nozzle vs. 30,000 for the complete nozzle).

Surprisingly enough, even if the numerical mesh has been built in a completely symmetrical way and the imposed excitation does not vary with the angular coordinate, disturbances in the azimuthal velocity are obtained, see Fig. 3.52. As in the case of the registered pressure signal at the same locations, the dominant frequency is obtained for $f_0=125,749$ Hz; also, higher fluctuation intensities are observed at lower and higher frequencies which are an integer part or multiple of the dominant frequency f_0 . Again, concerning the slope of the frequency spectrum, the same argument as for the pressure fluctuations holds for the velocity fluctuations since they result from the same kind of partial differential equation. By filtering out the time variations of the azimuthal velocity at the frequency of 127,368 kHz, which corresponds to the predicted resonance frequency of Fig. 3.48, one obtains the magnitude distribution of the azimuthal disturbances presented Fig. 3.54. The magnitude distribution is very similar to the pressure variations obtained for the resonant mode of Fig. 3.47. From the observed spatial distribution, it becomes then obvious why azimuthal disturbances may appear, even if the actuation imposed at the nozzle base is only applied in axial direction: Energy can be transferred from the mainly axial variations of pressure to excite the azimuthal velocity component through its own axial and radial variations.

In the section related to the jet simulation breakup, it has been shown that droplet ejection from the jet free-surface could only be obtained if an azimuthal disturbance exists. The presence of these azimuthal disturbances can then be explained if one takes into account the fluid compressibility. Depending on the nozzle geometry, resonant modes can exist at different frequencies and induce azimuthal variations of the velocity. Depending on the excitation frequency and the form of the imposed actuation, the azimuthal fluctuations can be damped out but also amplified. Therefore, it can be concluded that the liquid compressibility contributes among other phenomena (like the nozzle own mechanical vibrations and the possible coupling to the fluid flow) to the creation of azimuthal disturbances which eventually will trigger the creation of droplets after the fluid has been ejected out of the nozzle.

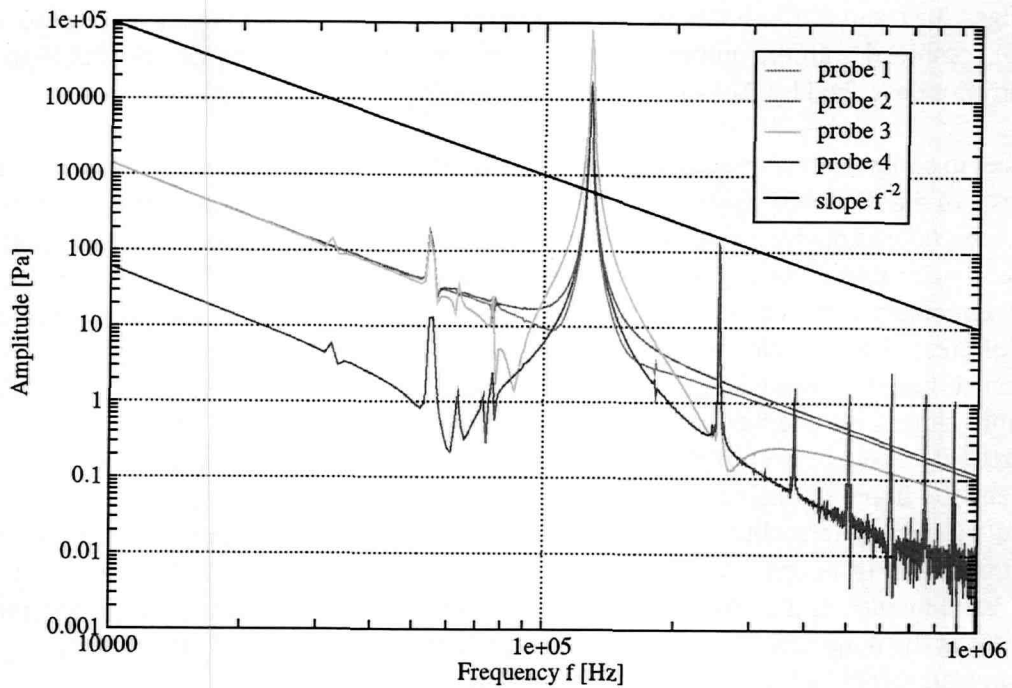


Figure 3.51: Fourier transform in frequency space of the pressure time signal registered at four different locations within the computational domain. The probe locations are given by Fig. 3.50

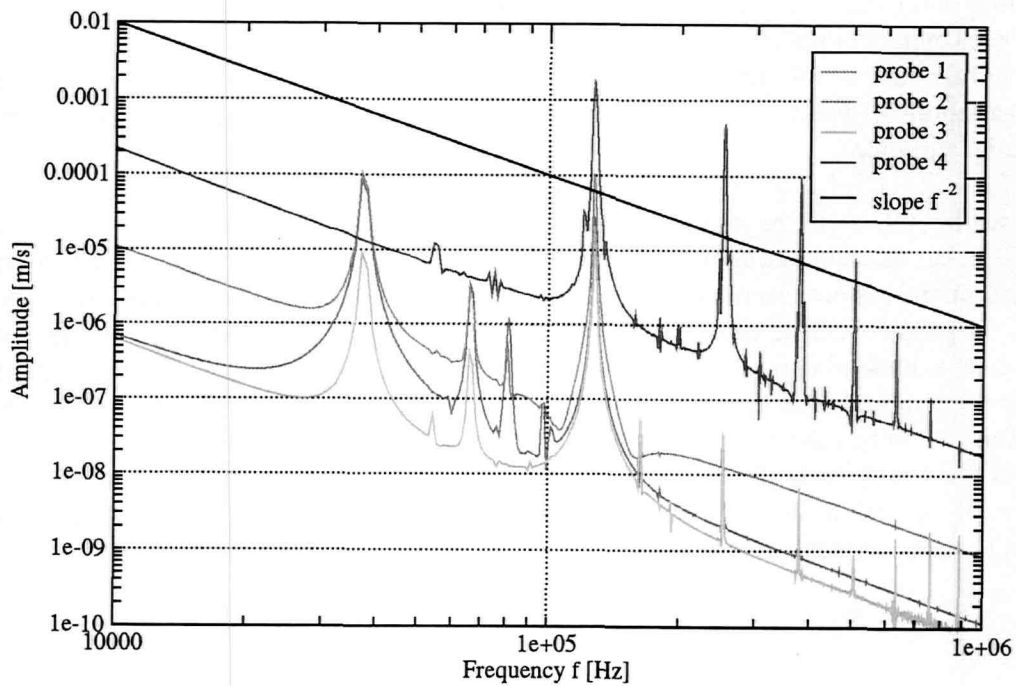


Figure 3.52: Fourier transform in frequency space of the time signal of the azimuthal velocity registered at four different locations within the computational domain. The probe locations are given by Fig. 3.50

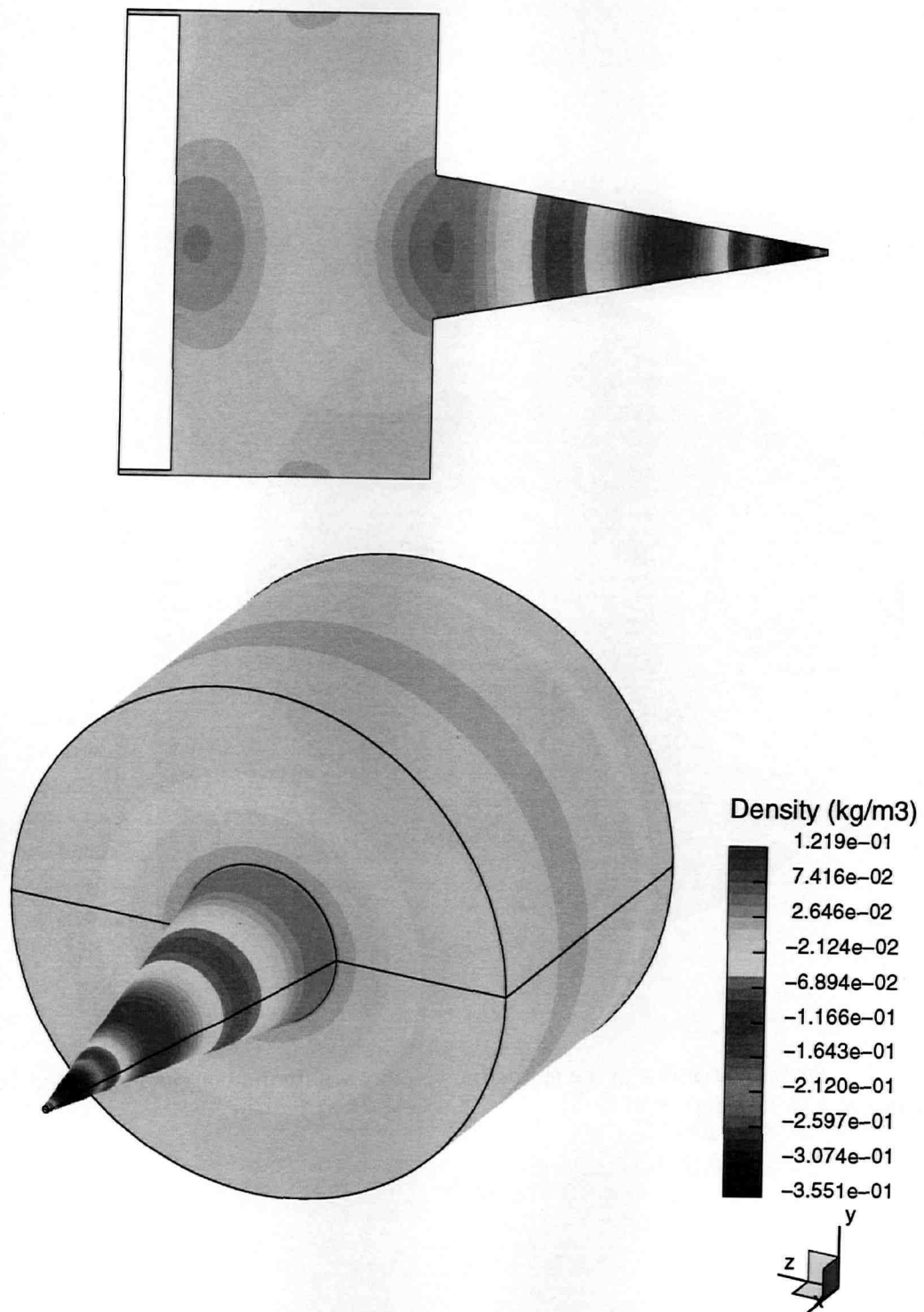


Figure 3.53: Density variation within the nozzle at a frequency of 126,670 kHz obtained for a section passing through the nozzle midplane (top) and on the nozzle external surface (bottom).

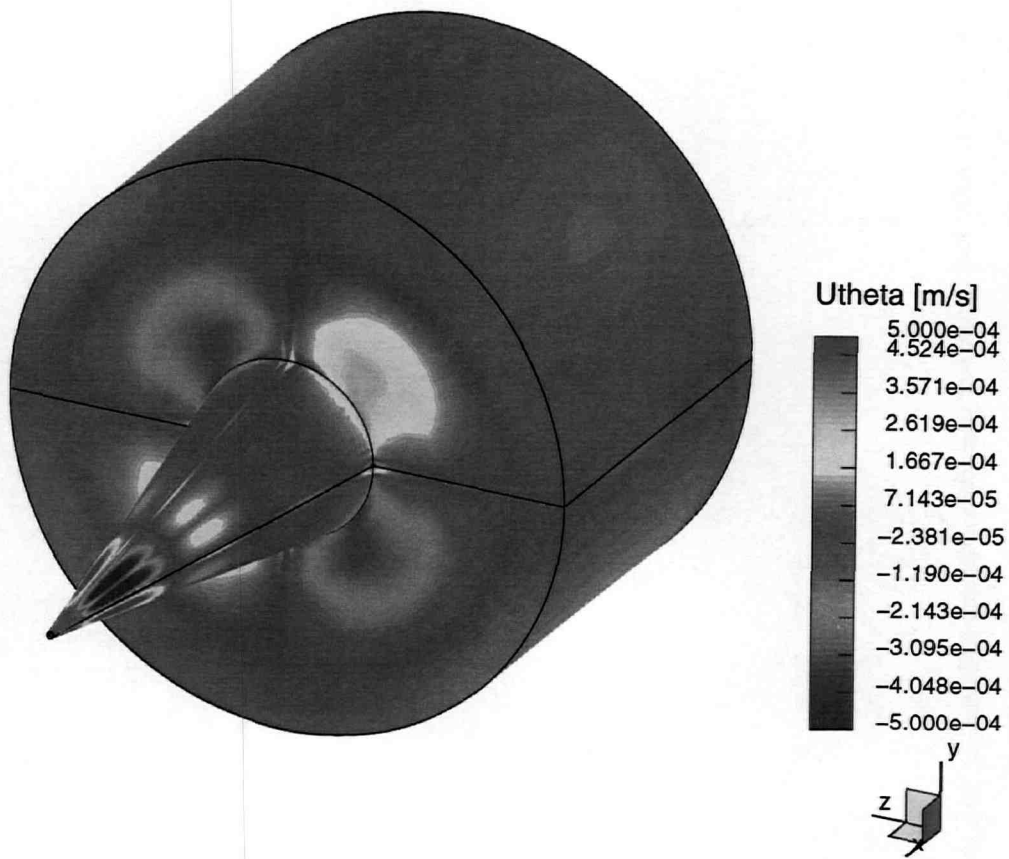


Figure 3.54: Spatial variations of the azimuthal velocity within the computational domain at a frequency of 127,368 Hz.

3.4 Air-flow sustained breakup of a capillary jet

The breakup of a round liquid jet can be enforced by the introduction of a well-defined disturbance. One possibility consists in the control of the jet velocity at the nozzle exit, as was the case in the examples studied in the preceding sections of this chapter. Another possibility is to apply disturbances to the jet free-surface through the surrounding gas. In this section, the present numerical method is tested under such conditions, i.e. using a surrounding air flow to trigger jet instability and subsequently breakup. The results of the numerical simulations presented hereafter are aimed to reproduce the breakup of a jet issuing from a capillary tube and submitted to elongation produced by a surrounding air flow (see also Fig. 3.55 for a schematic principle). This technique has the advantage to produce droplets whose size is much smaller than the diameter of the capillary tube and has been introduced first by Schmelz *et al.* [92]. Moreover, by forcing the jet breakup with a superimposed vibrational disturbance of given frequency, almost monosized droplets can be produced. However, the numerical simulations will remain focused on the “natural” jet breakup, i.e. without any additional forcing other than the surrounding air flow, since the numerical method has shown to give satisfactory results in the case of forced vibrations.

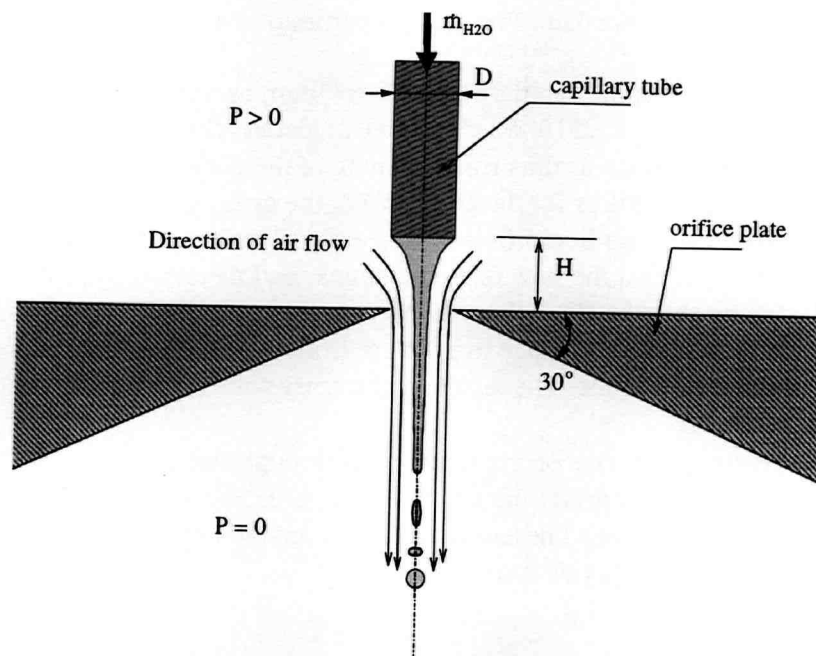


Figure 3.55: Pneumatic extension nozzle flow: schematic principle. Due to the pressure difference across the orifice plate, an air flow develops and strains the capillary jet that breaks up into droplets due to the Rayleigh instability. The orifice plate is placed at a distance H from the nozzle exit. In the present analysis: $H=D$.

3.4.1 Simulation approach

In this study, the liquid – whose physical properties are listed together with the ones of air in Table 3.7 – is water and flows out of a capillary tube at a constant mass flow rate $\dot{m}_e = 25$ g/min. A strong air flow is used to stretch the drop forming at the capillary tube under the

conjugated actions of flow and surface tension into a liquid jet. The air flow is induced by a pressure difference between a pressure chamber – separated from the surrounding air at rest by an orifice plate – and the environment. The pressure drop has been set to $\Delta p = 90$ Pa and corresponds to one of the values presented in the experiments of Schmelz *et al.*, [92]. For this pressure difference between pressure chamber and the ambient air at rest, one can assume that the air flow speed will have a magnitude of the order given by the following relation, obtained using Bernoulli's second law:

$$U_g = \sqrt{\frac{2\Delta p}{\rho}} = 12.31 \text{ m s}^{-1} \quad (3.40)$$

fluid	ρ [kg m ⁻³]	ν [m ² s ⁻¹]	σ [kg s ⁻²]
water	998.3	$1.003 \cdot 10^{-6}$	0.074
air	1.188	$1.550 \cdot 10^{-5}$	-

Table 3.7: Air-flow assisted breakup: Physical properties of the fluids used for the simulations.

Using the orifice diameter of the capillary tube ($D = 9$ mm) as a reference length, the Reynolds number for the air flow is $Re_g = 7216$, which is quite moderate. Since the capillary tube diameter has been chosen to be the same as the orifice opening of the plate, the reference length scale of the water flow is then the same as for the air flow. For the given mass flow rate – $\dot{m}_\ell = 25$ g/min –, the Reynolds number of the liquid flow is $Re_\ell = 59$. Because of the low Reynolds number values, it can be assumed that the flow remains laminar and therefore no turbulence model has been used. Assuming that the flow phenomena investigated are symmetric with respect to a rotation axis, it is meaningful to reduce to problem from three to two dimensions by modeling only a slice with one degree angle. The resulting geometry with the boundary conditions applied is shown in Fig. 3.56.

Because of the creeping velocity of the liquid flow through the capillary tube – $Re_\ell = 59$ –, some undesired side-effect appears, the so called *parasitic currents* (see also Chapter 2 for a description). The results obtained hereafter are to the author's opinion at the feasibility limits of the numerical method due to this feature.

3.4.2 Analysis of the air flow

Because of the sharp orifice edge, an unsteady air flow develops downstream of it. If no special attention is paid to the grid quality and the numerical scheme used (for example by using a first-order differencing scheme), the velocity gradients leading to detaching vortices at the plate edge will not be accurately enough resolved and a very smooth flow develops, showing no vortices detaching. In order to achieve sufficiently high spatial accuracy at the critical region around the orifice edge for capturing the onset of the vortex shedding, the use of local grid refinement is very helpful and has been employed here, as shown in Figure 3.57 by the detail of one of the numerical grids used in the simulations. Since vortices detaching at the orifice edge interact with the jet free-surface and act as an external disturbance, it is important to make sure that the distance λ between two vortex cores – which is linked to the vortex shedding frequency by the relation $f = U_g/\lambda$ – is captured correctly. To this end, a coarse grid with 30,248 CVs and a fine

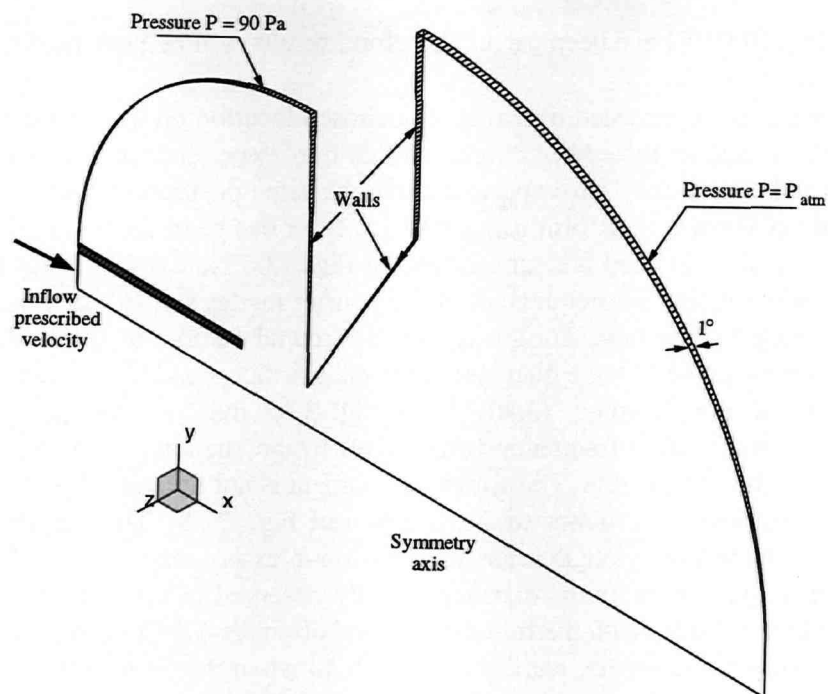


Figure 3.56: Computational domain used for the calculations. The distance between the nozzle outlet and the orifice plate corresponds to one nozzle diameter. The inflow velocity profile is the parabolic one of the Couette-Poiseuille laminar pipe flow.

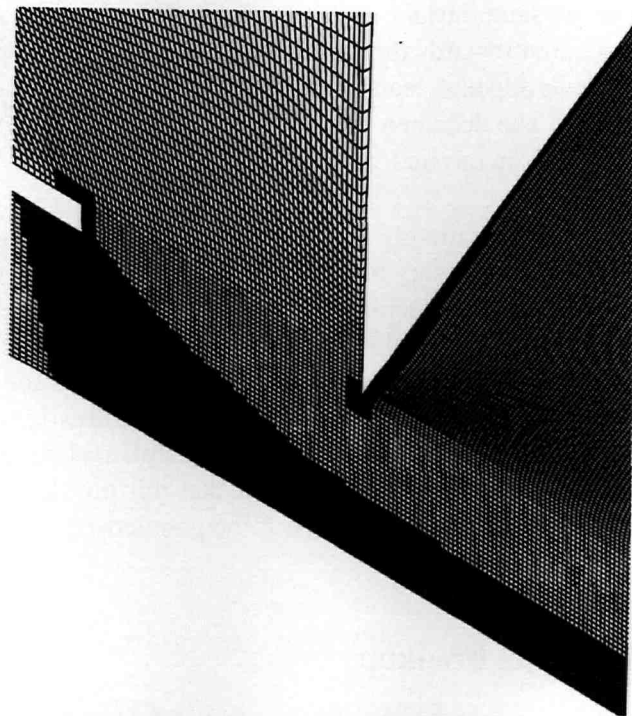


Figure 3.57: Detail of a numerical grid used for the simulations using the advantage of local refinement for resolving accurately the free-surface deformations as well as the detachment of vortices at the orifice edge.

grid with 125,210 CVs have been used. Therefore, results will be presented hereafter for both grids.

The pressure has been recorded over time at a chosen location on the coarse as well as on the fine grid. The locations have been chosen so that they experience at least the passage of one vortex core and so that they have approximately the same position in space on the coarse and the fine grid. A Fourier transform using a Welch filter has been applied to the recorded time signals. The results obtained are summarized in Figs. 3.62 and 3.63. It has been considered meaningful to normalize the frequencies of the Fourier modes so that one can easier recognize phenomena related to the flow. For this reason, a Strouhal number St is introduced and is built with the reference length D – the diameter of the plate orifice – and U_g , the estimated convective velocity of the air flow from eq. (3.40). From Fig. 3.62, the dominant Strouhal number is in the range 0.47–0.48. This frequency corresponds to the shedding frequency of the vortices detaching from the orifice edge. The vortex detachment is not influenced by the jet free-surface yet (no breakup) and corresponds to the situation of Fig. 3.58. The Strouhal number range would correspond to a wavelength separating two low-pressure regions of $\lambda = D/St = 0.01875$ – 0.01915 and is approximately the distance actually observed in the computations. Due to the interaction of the vortices with the free surface, one observes a shift in the dominant frequency to the lower Strouhal numbers, namely to $St \approx 0.40$ when the jet breaks up and droplets are formed, Fig. 3.63. This corresponds to the situation of Fig. 3.59.

A typical pressure distribution within the computational domain can be seen in Fig. 3.58, where the low pressure regions reveal vortex cores. Figure 3.59 shows liquid distribution with air pressure in the background: liquid drops are formed after jet break up, but they are not spherical yet, as they undergo oscillations in both axial and radial directions. Figure 3.60 shows the velocity field for the gas flow at the same instant as in Fig. 3.59. From this figure, it can be seen that the air is strongly accelerated towards the orifice edge and, because of the sharp angle of the orifice, a zone of high-shear appears, leading to the formation of an unsteady air flow, characterized by vortex shedding. The detached vortices eventually interact with the free-surface and the droplets after the jet breakup has undergone breakup.

Because of the need to resolve accurately in time the air flow in order to capture the detaching vortices at the plate edge, it is necessary to have a time step which is at least one hundredth of the characteristic frequency of the detaching vortices but also meet the restriction on the local Courant number due to the numerical scheme employed for modeling the free-surface flow. This leads practically to a time step in the range of $5 \cdot 10^{-5}$ seconds for the coarse grid and of $4 \cdot 10^{-6}$ seconds for the finer grid. Considering that the characteristic time for the liquid flow to form a jet is in about 1 second, it is then necessary to calculate about 20,000 to 250,000 time steps, depending on the grid spatial resolution. This makes this problem very tough to calculate because of the computational effort needed, even if the geometrical model and the physics are relatively simple.

3.4.3 Analysis of the jet breakup

Due to the pressure difference between the upside and the downside of the orifice plate, an air flow develops. This air flow has two major features:

- The strong acceleration of the air flow through the orifice allows, with the help of viscous shear, to strain the jet and thus reduce substantially its diameter. After Rayleigh breakup

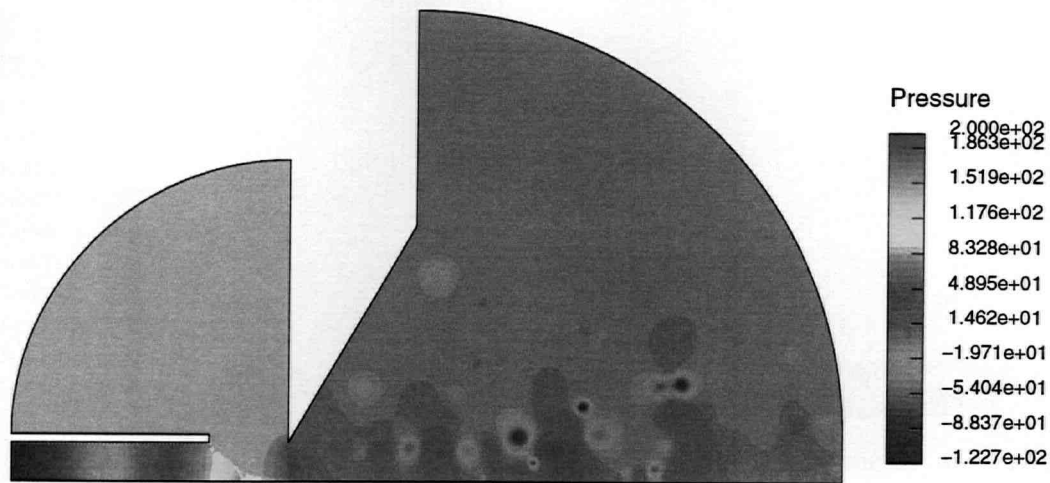


Figure 3.58: Instantaneous pressure distribution in the computational domain. Low pressure regions are marked in blue and indicate the presence of vortices ($\Delta p = 90\text{Pa}$). The pressure jump extending downward the nozzle exit (bottom left) corresponds to the actual position of the free-surface and is mainly due to surface tension effects. Flow is from left to right.

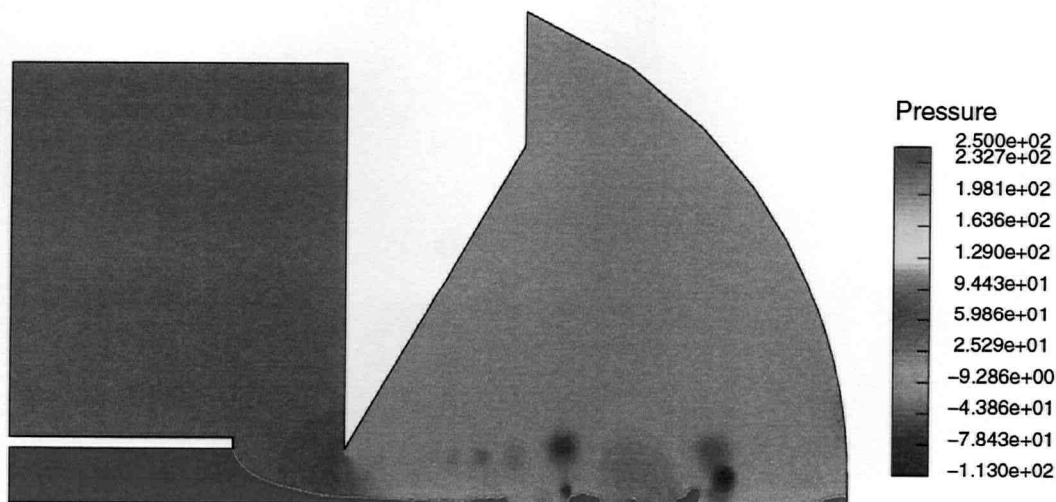


Figure 3.59: Instantaneous pressure distribution and free-surface deformation of the capillary jet (in red) within the computational domain on the coarse grid. Low pressure regions are marked in blue and indicate the presence of vortices. The vortices interact with the jet free-surface and detaching vortices because of the air flow over a droplet is observed as well (to be seen on the first droplet of the figure). Flow is from left to right.

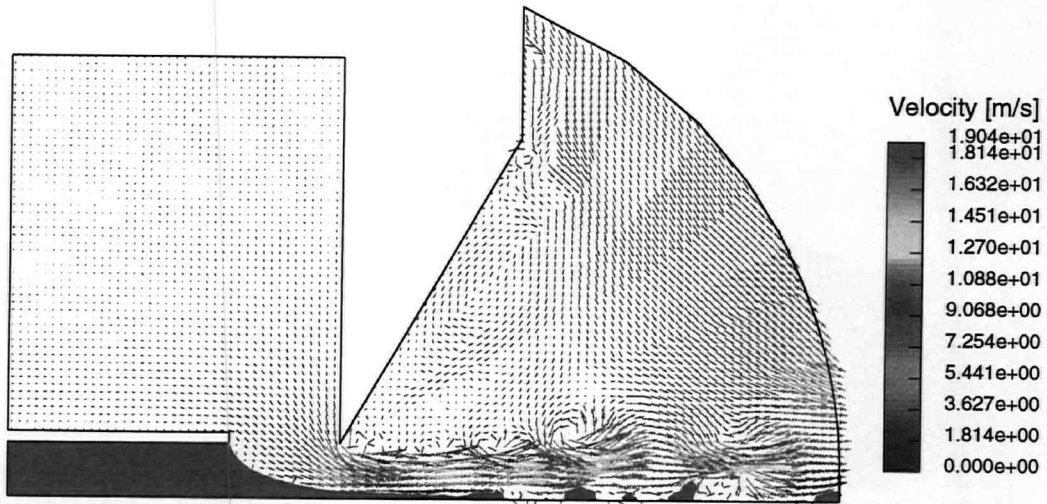


Figure 3.60: Instantaneous velocity distribution and free-surface deformation of the capillary jet (in red) within the computational domain on the coarse grid. The air flow is accelerated towards the orifice edge and an unsteady airflow develops downstream of it. Eventually vortices are created which interact with the jet free-surface (in red). Flow is from left to right.

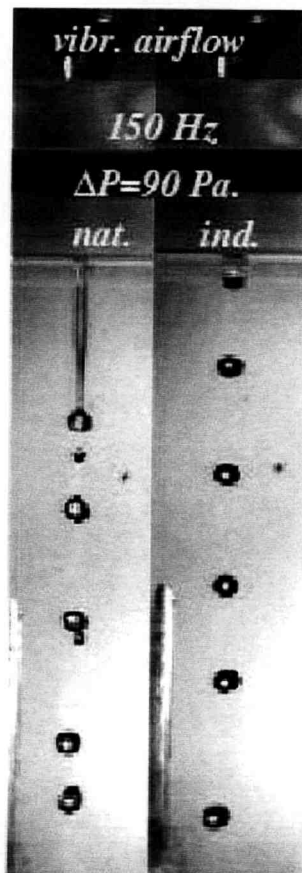


Figure 3.61: Free-surface shape obtained in the experiments of Schmelz *et al.*, reproduced from [92]. Although there are no indications about the distance between nozzle exit and orifice, it can be deduced from the experimental photographs that the ratio is $H/D \approx 0.5$.

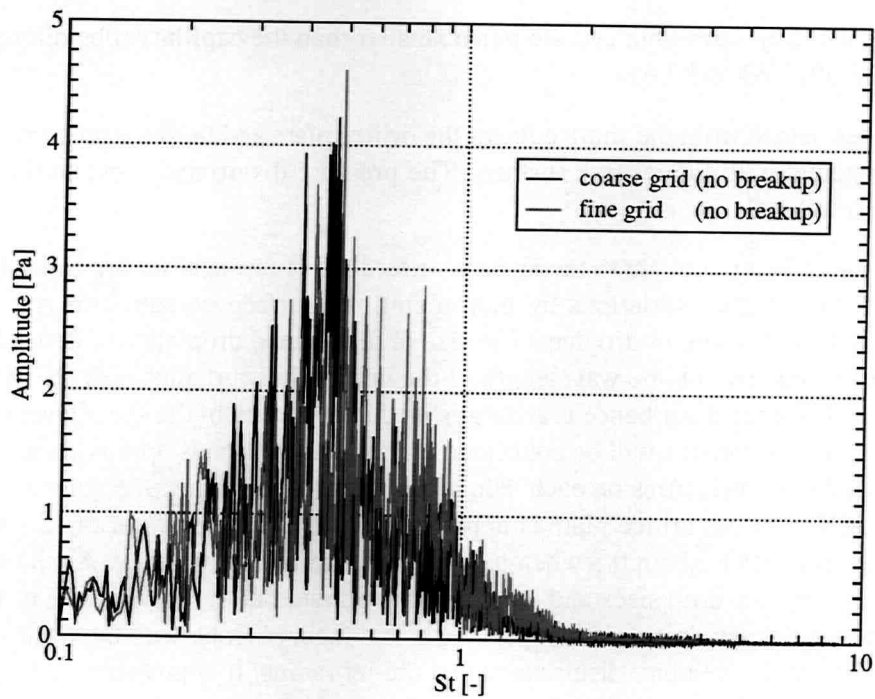


Figure 3.62: Amplitudes of the Fourier modes of the recorded time signals vs. the Strouhal number. The measured frequencies correspond to the situation of Fig. 3.58, for which the vortices detaching from the orifice edge do not interact with the jet free-surface (“no-breakup condition”); the jet has not formed yet and the liquid starts to drop from the capillary nozzle. The frequency spectrum registered is then solely due to vortices detaching from the orifice edge.

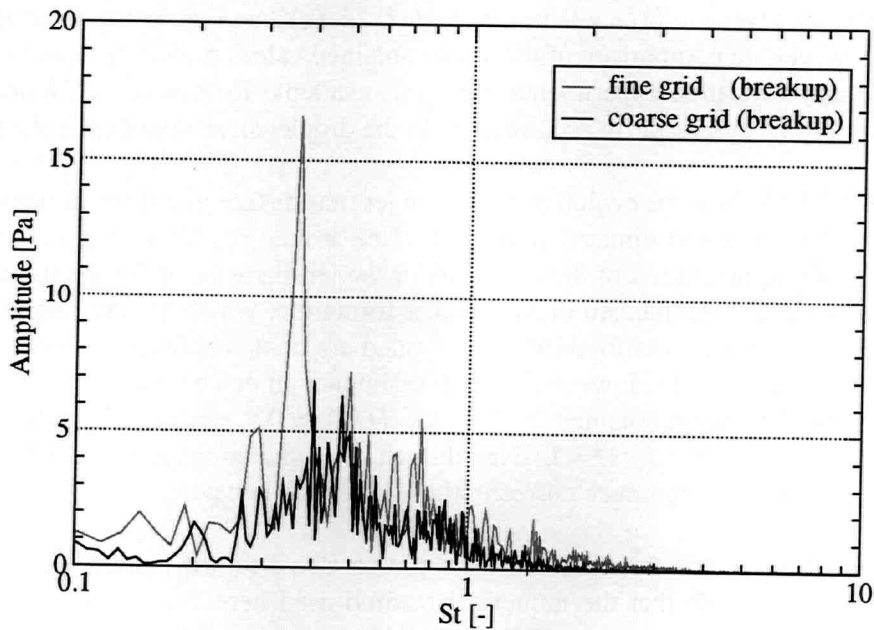


Figure 3.63: Amplitudes of the Fourier modes of the recorded time signals vs. the Strouhal number. The measured frequencies correspond to the situation of Fig. 3.59, for which the vortices detaching from the orifice edge interact with the jet free-surface (jet breakup conditions).

of the jet, drop sizes obtained are much smaller than the capillary tube diameter (see also Figs. 3.59, 3.64 and 3.65).

- Vortices detach from the sharp edge of the orifice plate and produce pressure disturbances that interact with the jet free surface. The pressure disturbances excite then the jet and force it to break up.

The disturbances being brought to the jet free-surface are of pressure nature and surface-tension acts against the pressure variations by minimizing the surface potential energy, which leads ultimately to the formation of droplets. The size of the formed droplets will depend not only on the jet diameter but also on the wavelength of the imposed disturbance (see also Section 3.1 of this chapter). Since the disturbance is arising from the instability of the shear layer developing at the orifice edge, the vortices will be convected at a velocity which is approximately the average value of the air-flow velocities on each side of the shear layer. Thus, the velocity at which the vortices detach from the orifice plate is approximately $U_g/2$. Therefore, the Strouhal number of the jet disturbances is about 0.8 when using $U_g/2$ as reference velocity. As shown in Section 3.1 of this chapter, the drop sizes and wavelength computed in the simulations of the Rayleigh breakup are in good agreement with experiments and theory. Thus, with the only knowledge of the wavelength of the velocity disturbance and the jet radius, it is possible to deduce the drop sizes that are obtained. Introducing the reduced wave-number k^* as:

$$k^* = \frac{2\pi r_0}{\lambda} = \frac{2\pi r_0}{D} St \quad (3.41)$$

where r_0 is the radius of the strained jet, we get from the computations $k^* \approx 0.27-0.34$ ($r_0 \approx 0.5-0.6\text{mm}$). From experimental and theoretical results [51, 89], one can determine for a given k^* the sizes of the main and satellite drops. In the investigated case, the satellite drops will have a non-dimensional diameter D_{drop}/D in the range 0.16–0.17 and the main drops in the range 0.26–0.30. However, no comparison of the above obtained values with experimental data could be performed as no detailed experimental data was available for this case. Nonetheless, the predicted droplet size agrees fairly accurately with the droplet sizes obtained in the simulation.

Figures 3.64 and 3.65 show the evolution in time of jet free surface as a three-dimensional view, obtained by rotating the two-dimensional free-surface around the jet axis of symmetry. This view gives a better appreciation of the reduction of the jet diameter under the influence of the air flow and also in the mechanism of the droplet formation, which arises from the Rayleigh instability. The free-surface deformations so obtained are comparable to those obtained in experiments, see also Fig. 3.61. However, no direct comparison can be made since the operating conditions of Fig. 3.61 were obtained for the ratio $H/D \approx 0.5$, whereas the simulations were undertaken for the fixed ratio $H/D = 1$. Even though, the simulations results can be considered as satisfactory, since they reproduce correctly the jet breakup behavior.

The results obtained for this test case and their comparison with the available information reported in [92] demonstrate that the numerical method used here is capable of predicting jet break-up due to excitation by surrounding air flow. This means that the present numerical approach – subject to a sufficient resolution in space and time – can predict primary jet breakup driven by the three main forcing types: capillary pinching, pressure fluctuations and shear effects on the free surface. It can therefore be used to design and test procedures for droplet generation and/or atomization, and in particular to aid experimental studies by providing a detailed

insight into flow structures and physical phenomena involved. Moreover, the results obtained with the numerical method employed in the present study show clearly that the widely accepted assumption for which the natural breakup of a capillary jet always occurs for the wavelength which is the most unstable (i.e. $k^* \approx 0.697$) is not valid, since the jet disintegration occurs for a wavelength which is dictated solely by the air flow instabilities ($k^* \approx 0.27-0.34$).

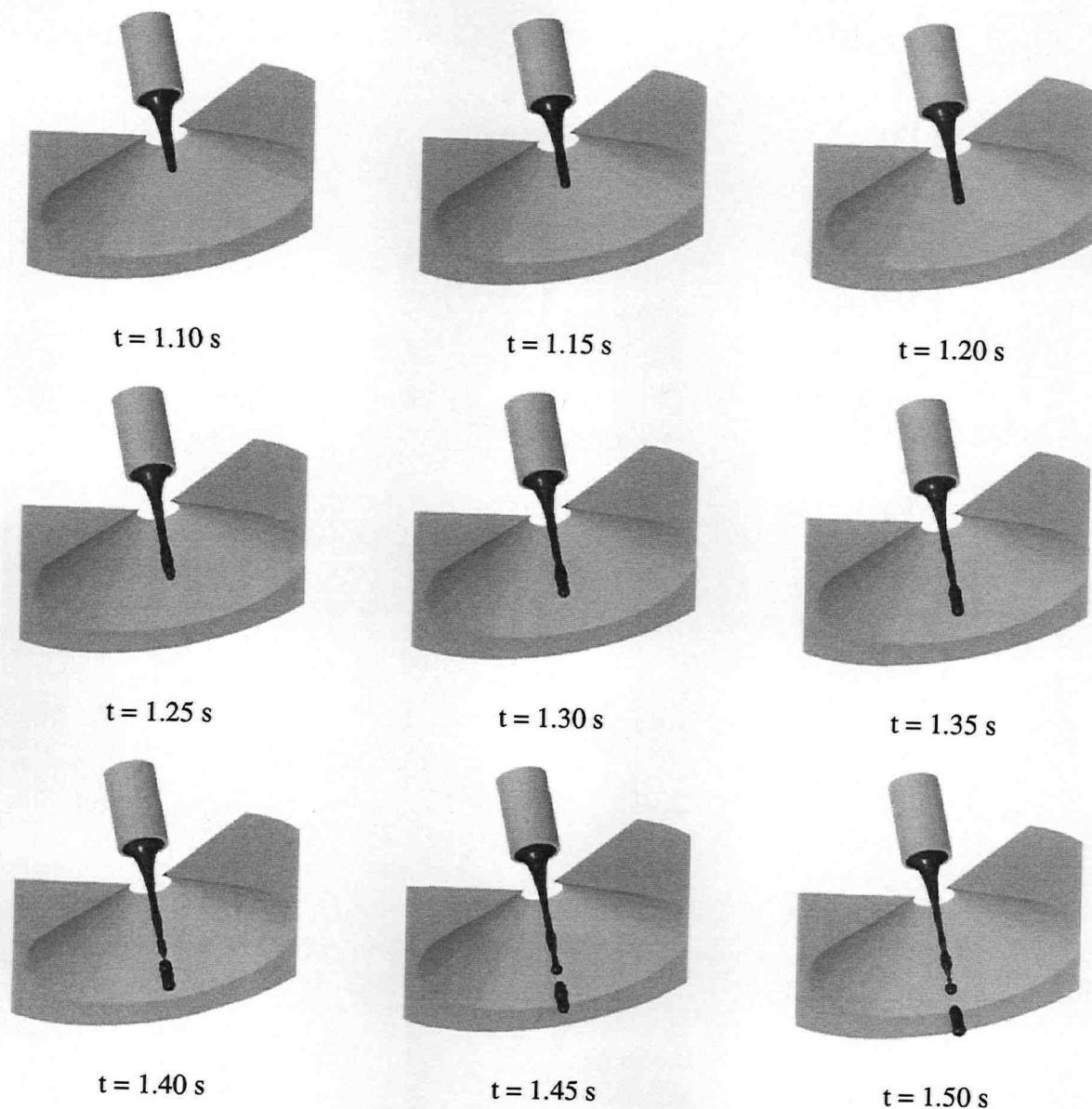


Figure 3.64: Evolution in time of the free-surface of the capillary jet submitted to an external disturbance arising from the vortex shedding of the surrounding air flow. Continuation on figure 3.65.

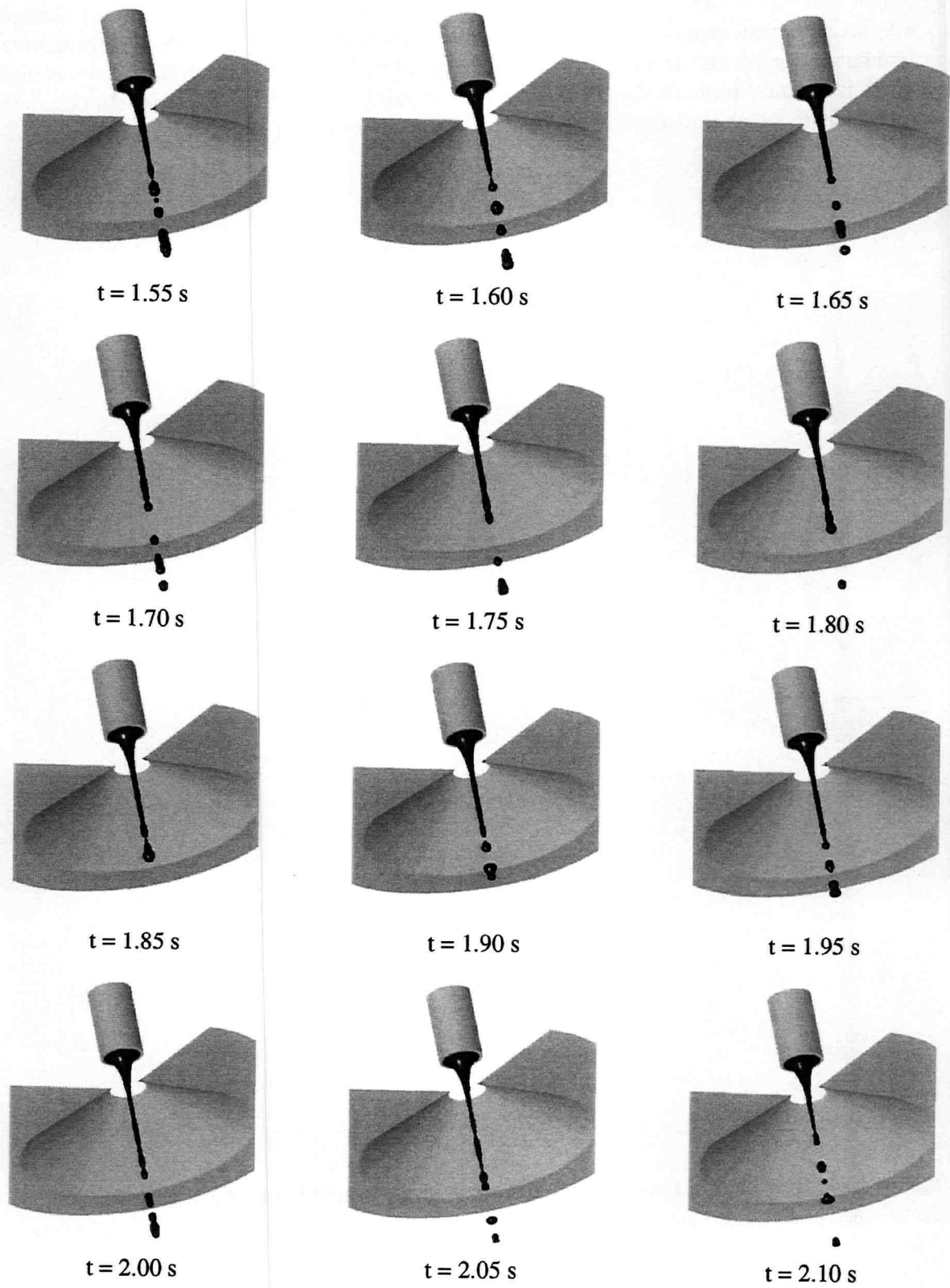


Figure 3.65: Continuation of figure 3.64

Chapter 4

Concluding remarks and further work

This chapter is devoted to concluding remarks concerning the work presented in the previous chapters. First, some remarks are made relatively to the Navier-Stoke solver used in this work. Then, after conclusions have been drawn relatively to the results obtained in the numerical simulations, an extension to the present work is proposed.

4.1 Concluding remarks

4.1.1 Discussion about numerical aspects

The numerical method employed, given by the commercial code *comet* [15], has shown to be able to handle efficiently (concerning both observed computational times and solution accuracy) free-surface flows involving surface-tension effects. Nevertheless, the numerical method has still some limitations inherent to the numerical scheme employed to discretize the surface-tension force using the CSF method. For high surface-tension coefficients and for low Reynolds number flows, the numerical method can also fail to predict correctly the shape of the free-surface because of the presence of parasitic currents. In all the applications presented here, parasitic currents are non-negligible, but, fortunately enough, they do not affect too much the flow field, since convective forces are at least one order of magnitude higher than the residual force occurring due to the imbalance between the pressure term and the discretized surface-tension force. Also, in order to reduce significantly the parasitic current intensity, a novel non-conservative discretization procedure was introduced and the results obtained so far look very promising.

During the creation process of the work summarized herein, it has been found necessary to extend the standard features of the computational method of *comet*. These extensions have been realized using the code facility to embed user defined functions and subroutines. This could be used to implement both methods described in this work for setting up the level of the free-surface and for the use of a convective outlet boundary condition.

The set-up of the free-surface level with the method described in Section 2.3.2, especially at the start of the jet simulation and also for imposing boundary conditions during the whole simulation, can substantially decrease the overall computational time, since the computational grid to be used for the simulations can be of arbitrary topology and the gas-fluid interface has not necessarily to follow the grid lines in order to obtain smooth variations of the void-fraction

field. This initialization practice has been applied successfully to other types of flow simulations involving a free-surface, for instance by Azcueta [11].

For investigating the effects of compressibility on the flow, it has been judged necessary to develop on the base of literature references and implement a new type of boundary which has been shown to have less influence on the pressure field when pressure disturbances have to escape the computational domain through its outlet. This boundary condition of convective type has been extensively tested as shown in Section 2.5 of the present thesis and has been also applied to the nozzle flow simulations. Nevertheless, no noticeable differences between the standard boundary condition (of Neumann type) and the newly implemented one could be found in this case. However, this special kind of boundary condition has been applied to other simulations, not reported here, also involving a free-surface, for which the convective boundary condition allowed to convect vortical and/or waves flow patterns out of the boundary, without the need to extend the computational domain near its outflow boundary by using coarse cells in order to damp out artificially any kind of disturbances whose wavelength is shorter than the mesh size.

4.1.2 Discussion of the simulation results

It is no doubt that the numerical method used here, hence the software package *COMET* [15], can be successfully used for the simulation of the primary breakup of liquid jets at scales for which surface tension plays a major role in the jet disintegration process.

The numerical method has been validated using experimental and theoretical results which can be found in the literature: In the case of the Rayleigh breakup, excellent agreement has been found with experimental data. For medium-ranged actuation frequencies, the deformations of the jet free surface correlate very well with the results gained from the linear wave theory, at least when the wave amplitude is not too high compared to its wavelength. Finally, for higher excitation frequencies, again very good concordance is found with both theoretical investigations and experimental data. When the cause of excitation is due to external sources triggered by, for instance, the presence of vortices, the wavelength of the disturbance can be used for obtaining the droplet size which corresponds fairly well to the one obtained in the simulation.

During the simulation work presented herein, it has been found that, when the deformations of the jet free-surface are not known *a priori*, the changes in the form of the free-surface are best captured if one uses a numerical mesh for which the aspect-ratios of the control-volumes are of the order of unity. This has also the advantage to achieve faster convergence with the solving procedure used compared to a numerical mesh having more stretched cells (thus having control-volumes with higher aspect-ratios). For this reason, the use of local refinement leads to a faster and more accurate capturing of the free-surface deformations at lower computational costs compared to a block-structured computational mesh at the same fineness level. Moreover, local refinement allows to concentrate efficiently most of the control-volumes in the regions of the computational domain where the deformations of the free-surface are expected, for which the variations of all physical quantities are large, and also to coarsen rapidly the numerical mesh in the regions where the gradients of all flow variables are small.

The use of different boundary conditions will lead to different simulation results. This is, of course, from the mathematical point of view and from the nature of the Navier-Stokes equations, a quite obvious assumption, but it should again be emphasized here. This result has a

quite dramatic influence on the shape of the free-surface deformation, as shown in the case of the forced breakup of a liquid jet at high excitation frequencies. Neglecting the influence of boundary layer effects resulting from the nozzle internal flow leads to a completely different jet-deformation behavior. Following this argumentation, also neglecting any kind of azimuthal disturbances explains why droplet formation within the observation window given by the computational domain cannot be obtained. Only with an additional azimuthal perturbation – the origin of which is to be found in possible acoustical resonance phenomena within the nozzle used for the fluid injection – droplets eject from the jet free-surface.

4.2 Further work

Of course, this work has not been intended to be extensive in its approach and in its coverage of the topic simulation of the primary breakup of liquid jets. Merely, the work presented here has had the purpose to first validate the numerical method presented here (and, to a certain point, to extend it) with regard to the investigated topic and, second, to set-up techniques and methods for being able to undertake efficiently this kind of simulations.

The extension of the numerical method has been undertaken in order to provide better initial position of the free-surface on arbitrary grids as well as a better type of boundary condition in the case of transient flows. Even if the formulation of the methods used is very general, their implementations remain limited to the cases investigated so far (and presented herein). Therefore, it is desirable to extend the implemented method to handle arbitrary polyhedral control volumes. Also, the implemented convective boundary condition can only be applied to laminar flows – which fits well for direct numerical simulations – and it would be useful to extend it to turbulent flows. Depending on the turbulence model used, an additional convective boundary condition could be used for any additional variable solved for on the base of the work presented here. Finally, the numerical scheme developed to tackle the problem of parasitic currents needs to be further developed, the physical pressure needs to be reconstructed from the non-conservative formulation employed in the novel discretization procedure.

Due to the fact that the Navier-Stokes solver used for the computations was only able to handle incompressible media when solving for liquid/gas flows with the interface-capturing scheme, it has not been possible to investigate the effects of any propagating acoustic waves on the behavior of the jet breakup. This feature requires the modeling of the fluid media to be compressible for the simulation of the free-surface flow. However, the numerical approach of the *COMET* solver relies on the assumption of the involved media being incompressible. The fluids, gas and liquid, do not mix and therefore, the gas-liquid flow is modeled as a single incompressible fluid with variable physical properties. With these assumptions, the mass conservation equation degenerates into the one for single-phased, incompressible media. This in turn allows to use the standard solving procedure. On the other hand, assuming both fluids compressible, even though weakly for being able to capture wave propagation phenomena, would have required the solver to be fundamentally changed.

The complete system nozzle + jet has been mostly simulated by separating the nozzle flow (for which a given velocity profile could be assumed and applied), from the jet flow. This allowed to lower the computational effort required for the simulation of the whole system. It has

also the advantage to study separately the respective flows, when assuming that the interaction between both flows is weak and that effectively the nozzle flow drives the jet breakup. This assumption is validated by experimental investigations and it is also the base of all theoretical models found in the literature and used for describing jet-breakup mechanisms. Further work is then needed to verify the validity of this assumption. The numerical method can then provide a very detailed picture of the flow features. How fine the resolved scales are, depends only on the resolution employed on the numerical grid. This is all the more important when turbulent flows are involved. The numerical tool could be used to correlate length scales of fluctuations arising from the wall-bounded nozzle flow and the turbulent structures responsible for the jet-breakup and/or disintegration. This valuable data is not necessarily accessible by the experiment due to the difficulty of measuring these flow features at scales of several 100 micrometers.

Bibliography

- [1] Knut Akselvoll and Parviz Moin. Large-eddy simulation of turbulent confined jets. *Journal of Fluid Mechanics*, 315:387–411, 1996.
- [2] F.-O. Albina, S. Muzaferija, and M. Perić. Numerische Simulation von Strahlinstabilitäten. In *Spray '99*, University of Bremen, Bremen, Germany, October 5–6 1999.
- [3] F.-O. Albina, S. Muzaferija, and M. Perić. Numerical simulation of jet instabilities. In *Proceedings of the 16th Annual Conference on Liquid Atomization and Spray Systems*, Darmstadt, Germany, September, 11 – 13 2000.
- [4] F.-O. Albina and M. Perić. Numerical simulation of pneumatic extension nozzles. In *Proceedings of the 17th ILASS-Europe*, Zurich, Switzerland, Spetember 2–6 2001.
- [5] F.-O. Albina and M. Perić. Numerische Simulation von Düseninnenströmungen und vom Strahlzerfall. In *Spray 2001, 6. Workshop über Technicken der Fluidzerstäubung und Untersuchungen von Sprühvorgängen*, Technische Universität Hamburg-Harburg, Hamburg, Germany, November 14–15 2001.
- [6] F.-O. Albina and M. Perić. Numerical simulation of forced breakup of a liquid jet. In E. Krause and W. Jäger, editors, *High Performance Computing in Science and Engineering 2003*. Springer, 2003.
- [7] D.M. Anderson, G.B. McFadden, and A.A. Wheeler. Diffuse-interface methods in fluid mechanics. *Ann. Rev. Fluid Mech.*, 30:139–165, 1998.
- [8] D.M. Anderson, G.B. McFadden, and A.A. Wheeler. A phase-field model of solidification with convection. *Physica D*, 135:175–198, 2000.
- [9] D.M. Anderson, G.B. McFadden, and A.A. Wheeler. A phase-field model with convection: numerical simulations. *Interfaces for the Twenty-First Century*, pages 1–15, December 3 ,1999.
- [10] N. Ashgriz and J.Y. Poo. FLAIR: Flux-line segment model for advection and interface reconstruction. *J. Comput. Phys.*, 93:449–468, 1991.
- [11] Rodrigo Azcueta Repetto. *Computation of turbulent free-surface flows around ships and floating bodies*. PhD thesis, Technical University of Hamburg-Harburg, 2001.
- [12] B.J. Boersma. Direct simulation of a jet diffusion flame. Technical report, Center for Turbulence Research, Annual Research Briefs, 1998.

- [13] J.U. Brackbill, D.B. Kothe, and C. Zemach. A continuum method for modeling surface tension. *J. Comput. Phys.*, 100:335–354, 1992.
- [14] L.S. Caretto, A.D. Gosman, S.V. Patankar, and D.B. Spalding. Two calculation procedures for steady, three-dimensional flows with recirculation. In *Proc. Third Int. Conf. Numer. Meth. Fluid Dyn.*, Paris, 1972.
- [15] CD adapco Group. *comet* user manual. Computational Dynamics Germany, Dürrenhofstrasse 4, 90402 Nuremberg, Germany, 2001.
- [16] K.C. Chaudhary and Redekopp L.G. The non-linear capillary instability of a liquid jet. *J. Fluid Mech.*, 96:257–297, 1980.
- [17] H. Chaves, H. Glate, F. Obermeier, T. Seidel, V. Weise, and G. Wozniak. Disintegration of sinusoidally forced liquid jet. In *ILASS-Europe 2000*, Darmstadt, Germany, September 11–13 2000.
- [18] N. Chigier and R.D. Reitz. *Recent Advances in Spray Combustion: Spray Atomization and Drop Burning Phenomena*, chapter 4 Regimes of Jet Breakup and Breakup Mechanisms (Physical Aspects), pages 137–160. American Institute of Aeronautics and Astronautics Inc., Reston, Virginia, 1995.
- [19] A.J. Chorin. On the convergence of discrete approximations to the Navier-Stokes equations. *Math. Comp.*, 23:341–353, 1969.
- [20] P. Collela, D.T. Graves, D. Modiano, E.G. Puckett, and M. Sussman. An embedded boundary/volume of fluid method for free surface flows in irregular geometries. In *Proceedings of FEDSM99, 3rd ASME/JSME Joint Fluid Engineering Conference*, San Francisco, California, USA, July 18–23 1999.
- [21] M.S. Darwish. A new high-resolution scheme based on the normalized variable formulation. *Numerical Heat Transfer, Part B*, 24:353–371, 1993.
- [22] E. de Korte. *Simulation of Thin Film Flows*. PhD thesis, University of Twente, Enschede, The Netherlands, 2002.
- [23] R.J. Donnelly and W. Glaberson. Experiments on the capillary instability of a liquid jet. *Proceedings of the Royal Society of London*, A 290:547–556, 1966.
- [24] Milton Van Dyke. *An Album of Fluid Motion / assembled by Milton Van Dyke*. Parabolic Press, 1982.
- [25] Joel Ferziger and Milovan Perić. *Computational Methods for Fluid Dynamics*. Springer Verlag, 3rd edition, 2001.
- [26] J. Fromm. Finite difference computation of the capillary jet, free surface problem. In Springer, editor, *Proceedings of the 7th International Conference in Numerical Methods in Fluid Dynamics*, 1981.
- [27] P.H. Gaskell and A.K. Lau. Curvature-compensated convective transport: SMART, a new boundedness preserving transport algorithm. *International Journal for Numerical Methods in Fluids*, 8:617–641, 1988.

- [28] I. Ginzburg and G. Wittum. Two-phase flows on interface refined grids modeled with VOF, staggered finite volumes, and spline interpolants. *Journal of Computational Physics*, 166:302–335, 2001.
- [29] E.F. Goedde and M.C. Yuen. Experiments on liquid jet instability. *Journal of Fluid Mechanics*, 40:495–511, 1970.
- [30] G.H. Golub and C.F. Van Loan. *Matrix Computations*. The John Hopkins University Press, third edition, 1996.
- [31] A. Göpfert, T. Riedrich, and G. Riedrich. *Funktionalanalysis*, volume 22 of *Mathematik für Ingenieure, Naturwissenschaftler, Ökonomen, Landwirte*. Teubner Verlag, 2nd edition, 1986.
- [32] P. M. Gould. *Analysis of plates and shells*. Prentice Hall, 1998.
- [33] R.P. Grant and S. Middleman. Newtonian jet stability. *AIChE Journal*, 12:669–678, 1966.
- [34] Igor S. Grigoriev and Evgenii Z. Meilikhov, editors. *Handbook of physical quantities*, chapter 4. CRC Press, 1997.
- [35] F.A. Harlow and J.E. Welsh. Numerical calculation of time dependent viscous incompressible flow with free surface. *Phys. Fluids*, 8:2182–2189, 1965.
- [36] E.H. Hirschel, editor. *Notes on Numerical Fluid Mechanics*, volume 52 of *Flow Simulation with High-Performance Computers II*. Vieweg Verlag, Vieweg Braunschweig, 1996. DFG Priority Research Programme Results 1993–1995.
- [37] C.W. Hirt and B.D. Nichols. Volume of fluid (VOF) method for dynamics of free boundaries. *J. Comput. Phys.*, 39:201–221, 1981.
- [38] J.W. Hoyt and J.J. Taylor. Waves on water jets. *J. Fluid Mech.*, 83:119–127, 1977.
- [39] D. Jacqmin. An energy approach to the continuum surface tension method. *AIAA Paper 96-0858*, 1996.
- [40] D. Jacqmin. Calculation of two-phase Navier-Stokes flow using phase-field modelling. *J. Comput. Phys.*, 155:96–127, 1999.
- [41] D. Jamet, D. Torres, and J.U. Brackbill. On the theory and computation of surface tension: The elimination of parasitic currents through energy conservation in the second gradient method. *Journal of Computational Physics*, 2002.
- [42] G. Jin and M. Braza. A nonreflecting boundary condition for incompressible unsteady Navier-Stokes calculations. *Journal of Computational Physics*, 107:239–253, 1993.
- [43] F.X. Keller, J. Li, A. Vallet, and S. Zaleski. Direct Navier-Stokes simulations on interface breakup and atomization. In *Proceedings of the ICLASS-94*, pages 56–62, Rouen, France, July 1994.
- [44] J.B. Keller, S.I. Rubinow, and Y.O. Tu. Spatial instability of a jet. *Physics of Fluids*, 16:2052–2055, 1973.

- [45] Dongjoo Kim and Haechon Choi. A second-order time-accurate finite volume method for unsteady incompressible flow on hybrid unstructured grids. *Journal of Computational Physics*, 162:411–428, 2000.
- [46] I. Kim and W.A. Sirignano. Three-dimensional wave distortion and disintegration of thin planar liquid sheets. *J. Fluid Mech.*, 410:147–183, 2000.
- [47] D.B. Kothe, M.W. Williams, K.L. Lam, D.R. Korzekwa, P.K. Tubesing, and E.G. Puckett. A second-order accurate, linearity-preserving volume tracking algorithm for free surface flows on 3-D unstructured meshes. In *Proceedings of the 3rd ASME/JSME Joint Fluid Engineering Conference*, San Fransisco, California, USA, July 18–22 1999.
- [48] Matthias Krömer. Numerical simulation of cavitation. In Seung-Deog Yoo, editor, *Fluid Mechanics Seminar 1997-1998*, pages 18–31. Technische Universität Hamburg-Harburg Arbeitsbereiche Schiffbau, 1999.
- [49] B. Lafaurie, T. Mantel, and S. Zaleski. Direct Navier-Stokes simulations of the near nozzle region. In *ILASS-Europe '98*, pages 54–59, Manchester, UK, July 6–8 1998.
- [50] B. Lafaurie, C. Nardone, R. Scardovelli, S. Zaleski, and G. Zanetti. Modelling merging and fragmentation in multiphase flows with SURFER*. *J. Comput. Phys.*, 113:134–147, 1994.
- [51] P. Lafrance. Nonlinear breakup of a laminar liquid jet. *The Physics of Fluids*, 18(4):428–432, 1975.
- [52] L. Landau and E. Lifchitz. *Theoretical Physics*, volume 6, Fluid Mechanics. MIR editions, 2nd edition, 1989.
- [53] A. Leboissetier and S. Zaleski. Direct numerical simulation of the atomisation of a liquid jet. In *Proceedings of the 17th ILASS-Europe*, Zurich, Switzerland, September 2–6 2001.
- [54] S.J. Leib and M.E. Goldstein. The generation of capillary instabilities on a liquid jet. *J. Fluid Mech.*, 168:479–500, 1986.
- [55] B.P. Leonard. A stable and accurate convection modelling procedure based on quadratic interpolation. *Comp. Meth. Appl. Mech. Eng.*, 19:59–98, 1979.
- [56] B.P. Leonard. Simple high-accuracy resolution program for convective modeling of discontinuities. *Int. J. Numer. Meth. Eng.*, 8:1291–1318, 1988.
- [57] Jie Li. Calcul d'interface affine par morceaux. *C.R. Acad. Sci. Paris*, 320(II b):391–396, 1995.
- [58] P.Y. Liang and R.J. Ungewitter. *Recent Advances in Spray Combustion: Spray Atomization and Drop Burning Phenomena*, chapter Modeling of Atomization and Secondary Breakup from First Principles, pages 481–504. American Institute of Aeronautics and Astronautics Inc., Reston, Virginia, 1995.
- [59] Ž. Lilek. *Ein Finite-Volumen Verfahren zur Berechnung von inkompressiblen und kompressiblen Strömungen in komplexen Geometrien mit beweglichen Gittern und freien Oberflächen*. PhD thesis, University of Hamburg, Germany, 1995.

- [60] S.P. Lin. *Recent Advances in Spray Combustion: Spray Atomization and Drop Burning Phenomena*, chapter 5 Regimes of Jet Breakup and Breakup Mechanisms (Mathematical Aspects), pages 137–160. American Institute of Aeronautics and Astronautics Inc., Reston, Virginia, 1995.
- [61] S.P. Lin. Roles played by the interface shear in the instability mechanism of a viscous liquid jet surrounded by a viscous gas in a pipe. In *Proceedings of the 17th ILASS-Europe*, Zurich, Switzerland, September 2–6 2001.
- [62] S.P. Lin and Z.W. Lian. Absolute instability of a liquid jet in a gas. *Physics of Fluids*, 32:490–499, 1989.
- [63] S.P. Lin and Z.W. Lian. Mechanism of the breakup of a liquid jet. *AIAA Journal*, 28:120–126, 1990.
- [64] S.P. Lin, Z.W. Lian, and B.J. Creighton. Absolute and convective instability of a liquid sheet. *J. Fluid Mech.*, 220:673–679, 1990.
- [65] S.P. Lin and D.Z. Reitz. Drop and spray formation from a liquid jet. *Annu. Rev. Fluid Mech.*, 30:85–105, 1998.
- [66] LMS International, Leuven, Belgium. *SYSNOISE User's Guide*, 2001.
- [67] A Mansour and N. Chigier. Satellite formation in capillary jet breakup. *Phys. Fluids A*, 2(7):1141–1144, 1990.
- [68] A Mansour and N. Chigier. Dynamic behavior of liquid sheets. *Phys. Fluids A*, 3(12):2971–2980, 1991.
- [69] F. Mayashek and N. Ashgriz. A height-flux method for simulating free surface flows and interfaces. *Internat. J. for Numer. Methods in Fluids*, 17:1035–1052, 1993.
- [70] C. Mehring and W.A. Sirignano. Nonlinear capillary wave distortion and disintegration of thin planar sheets. *J. Fluid Mech.*, 388:69–114, 1999.
- [71] C. Mehring and W.A. Sirignano. Axisymmetric capillary waves on thin annular liquid sheets. I. temporal stability. *Physics of Fluids*, 12(6):1417–1439, 2000.
- [72] C. Mehring and W.A. Sirignano. Axisymmetric capillary waves on thin annular liquid sheets. II. spatial development. *Physics of Fluids*, 12(6):1440–1460, 2000.
- [73] M. Meier. *Numerical and experimental study of large steam-air bubbles injected in a water pool*. PhD thesis, ETHZ, Zürich, 1999.
- [74] C.C. Miesse. Correlation of experimental data on the disintegration of liquid jets. *Industrial and Engineering Chemistry*, 47(9):1690–1701, 1955.
- [75] Toshio Miyaushi, Mamoru Tanahashi, and Motohiro Suzuki. Inflow and outflow boundary conditions for direct numerical simulations. *JSME International Journal*, 39(2):305–314, 1996.

- [76] S. Muzaferija and M. Perić. Computation of free surface flows using interface-tracking and interface-capturing methods. In O. Mahrenholtz and M. Markiewicz, editors, *Non-linear Water Wave Interaction*, chapter 3. Computational Mechanics Publications, 1998.
- [77] S. Muzaferija, M. Perić, P.C. Sames, and T.E. Schellin. A two-fluid Navier-Stokes solver to simulate water entry. In *Proceedings of the 22nd Symposium on Naval Hydrodynamics*, Washington, D.C., August 9–14 1998.
- [78] M. Oevermann, R. Klein, M. Berger, and J. Goodman. A projection method for two-phase compressible flow with surface tension and sharp interface resolution. Technical Report Report 00-17, ZIB, May 2000.
- [79] S. Osher and J.A. Stanley. Fronts propagating with curvature-dependent speed: Algorithms based on Hamilton-Jacobi formulations. *J. Comput. Phys.*, 79:12–49, 1988.
- [80] Laura L. Pauley, Moin Parviz, and William C. Reynolds. The structure of two-dimensional separation. *Journal of Fluid Mechanics*, 220:397–411, 1990.
- [81] S. Popinet and S. Zaleski. A front-tracking algorithm for accurate representation of surface tension. *Int. J. Numer. Meth. Fluids*, 1999.
- [82] R.H. Rangel and W.A. Sirigano. Nonlinear growth of Kelvin-Helmholtz instability: Effect of surface tension and density ratio. *Phys. Fluids*, 31:1845–1855, 1988.
- [83] R.H. Rangel and W.A. Sirigano. The linear and non-linear instability of a fluid sheet. *Phys. Fluids A*, 3:2392–2400, 1991.
- [84] Lord Rayleigh. *The theory of sound*, volume II, pages 360–376. New-York Dover, 1945.
- [85] R.D. Reitz and F.V. Bracco. Mechanism of disintegration of a liquid jet. *Physics of Fluids*, 25:1730–1742, 1982.
- [86] C.M. Rhie and W.L. Chow. Numerical study of the turbulent flow past an airfoil with trailing edge. *AIAA Journal*, 21(11):1525–1532, 1983.
- [87] W.J. Rider and D.B. Kothe. Reconstructing volume tracking. *Journal of Computational Physics*, 141:112–152, 1998.
- [88] M. Rudman. A volume tracking method for incompressible multifluid flows with large density variations. *Int. J. Numer. Meth. Fluid*, 28:357–378, 1998.
- [89] D.F. Rutland and G.J. Jameson. Theoretical prediction of the sizes of drops formed in the breakup of capillary-jets. *Chemical Engineering Science*, 25:1689–1698, 1970.
- [90] D.F. Rutland and G.J. Jameson. A non-linear effect in the capillary instability of liquid jets. *Journal of Fluid Mechanics*, 46:267–271, 1971.
- [91] R. Scardovelli and S. Zaleski. Direct numerical simulation of free-surface and interfacial flow. *Ann. Rev. Fluid Mech.*, 31:567–603, 1999.
- [92] F. Schmelz, S. Schneider, and P. Walzel. Production of monosized droplets in pneumatic extension nozzles. In *Proceedings of the 16th ILASS-Europe*, Darmstadt, Germany, September 11–13 2000.

- [93] E. Schreck. *Entwicklung und Anwendung einer Finite-Volumen-Mehrgittermethode zur Strömungssimulation auf Parallelrechnern*. PhD thesis, University of Hamburg, Germany, 1996. (in german).
- [94] E. Schreck and M. Perić. Computation of fluid flow with a parallel multigrid solver. *Int. J. Numer. Methods in Fluids*, 16:303–327, 1993.
- [95] T. Seidel, H. Chaves, and F. Obermeier. Grundlagenuntersuchungen an einer Einstoffdüse bei hochfrequenter Strahlanregung und stroboskopischer Betrachtung. In *Spray '99*, University of Bremen, Bremen, Germany, October 5–6 1999.
- [96] V. Seidl. *Entwicklung und Anwendung eines parallelen Finite-Volumen-Verfahren zur Strömungssimulation auf unstrukturierten Gittern mit lokaler Verfeinerung*. PhD thesis, Institut für Schiffbau der Universität Hamburg, November 1997. (in german).
- [97] W.A. Sirignano and C. Mehring. Conical and annular free liquid film instabilities. In *Proceedings of the 16th ILASS-Europe*, Darmstadt, Germany, September 11–13 2000.
- [98] Numerical Recipes Software, editor. *Numerical Recipes in C: The art of scientific computing*. Cambridge University Press, 1992.
- [99] A. Sohankar, C. Norber, and L. Davidson. Low-Reynolds-number flow around a square cylinder at incidence: study of blockage, onset of vortex shedding and outlet boundary condition. *International Journal for Numerical Methods in Fluids*, 26:39–56, 1998.
- [100] A. Sohankar, C. Norber, and L. Davidson. Numerical simulation of flow past a circular cylinder. In *Proceedings of FEDSM99, 3rd ASME/JSME Joint Fluids Engineering Conference*, San Francisco, California, USA, July, 18 – 23 1999. Article number FEDSM99-7172.
- [101] M.C. Stirling and C.A. Schleicher. The instability of capillary jets. *Journal of Fluid Mechanics*, 68:477–495, 1975.
- [102] M. Sussman, P. Smereka, and S. Osher. A level set approach for computing solutions to incompressible two-phase flow. *J. Comput. Phys.*, 114:146–159, 1994.
- [103] J.L. Thé, G.D. Raithby, and G.D. Stubble. Surface-adaptive finite-volume method for solving free surface flows. *Numer. Heat Transfer, Part B*, 26:367–380, 1994.
- [104] G. Tryggvarson, B. Bunner, A. Esmaceli, D. Juric, N. Al Rawahi, W. Tauber, J. Han, S. Nas, and Y.-J. Jan. A front-tracking method for the computations of multiphase flow. *Journal of Computational Physics*, 169:708 – 759, 2001.
- [105] O. Ubbink. *Numerical prediction of two fluid systems with sharp interfaces*. PhD thesis, University of London, 1997.
- [106] O. Ubbink and R.I. Issa. A method for capturing sharp fluid interfaces on arbitrary meshes. *J. Comput. Phys.*, 153:26–50, 1999.
- [107] C.Z. Weber. Zum Zerfall eines Flüssigkeitsstrahles. *Z. angew. Math. Mech.*, 11:136–154, 1931.

- [108] A.A. Wheeler and G.B. McFadden. On the notion of a ξ -vector and a stress tensor for a general class of anisotropic diffuse interface models. *Proc. Roy. Soc. Lond. A*, pages 1611–1639, 1997.
- [109] Prof. Dr. G. Wittum. Effiziente numerische Methoden zur Berechnung von Mehrphasenströmungen. Ergebnisbericht 96-98, SFB 4-12, Stuttgart, 1998.
- [110] XmGrace. <http://plasma-gate.weizmann.ac.il/Grace/>, 2002.
- [111] S. Zaleski, J. Li, and S. Succi. Two-dimensional Navier-Stokes simulation of deformation and breakup of liquid patches. *Phys. Rev. Letters*, 75(2):244–247, 1995.
- [112] A.Z. Zinchenko, M.A. Rother, and R.H. Davis. Cusping, capture and breakup of interacting drops by a curvatureless boundary-integral algorithm. *J. Fluid. Mech.*, 391:249–292, 1999.

Appendix A: An equivalent formulation of the minimization problem

Let's define a functional $\mathcal{F}(v)$ on the set \mathcal{M} of the locally continuous, linear functions defined on the bounded domain Ω :

$$\mathcal{F}(v) = \iiint_{\Omega} (\nabla v - \mathbf{Q})^2 dV. \quad (\text{A.1})$$

\mathbf{Q} is a vector field defined on Ω for which one desires to get an estimate through the gradient ∇v . \mathcal{M} is a subset of $C^2(\Omega)$, the set of functions whose square value is integrable over Ω :

$$\mathcal{M} \subset \mathcal{H} = \left\{ f \in C^2(\Omega) / \left[\iiint_{\Omega} |f|^2 dV \right]^{\frac{1}{2}} < +\infty \right\}. \quad (\text{A.2})$$

A function \hat{v} is to be found in the set \mathcal{M} that minimizes the functional $\mathcal{F}(v)$. If \hat{v} corresponds to a local minimum of the functional $\mathcal{F}(v)$, one can write for all v in the neighborhood $\mathcal{N}(\hat{v})$:

$$\forall v \in \mathcal{N}(\hat{v}), \quad \mathcal{F}(v) \geq \mathcal{F}(\hat{v}) \quad (\text{A.3})$$

In this neighborhood, the Gateaux-differential vanishes from the location \hat{v} in every direction η [31]; the Gateaux-differential being defined for a given direction η by:

$$\delta\mathcal{F}(\hat{v}, \eta) = \lim_{\alpha \rightarrow 0} \frac{\mathcal{F}(\hat{v} + \alpha\eta) - \mathcal{F}(\hat{v})}{\alpha} \quad \alpha \in \mathfrak{R}, \eta \in \mathcal{N}(\hat{v}). \quad (\text{A.4})$$

One takes a subset \mathcal{T} from \mathcal{M} satisfying:

$$\mathcal{T} = \{ f \in C^2(\Omega) / f = 0 \text{ on } \partial\Omega \} \quad (\text{A.5})$$

On takes also a chosen direction η from \mathcal{T} , that is contained in $\mathcal{N}(\hat{v})$. The Gateaux-differential

in the direction η is then given through the following relation:

$$\begin{aligned}
 \delta\mathcal{F}(\hat{v}, \eta) &= \lim_{\alpha \rightarrow 0} \frac{1}{\alpha} \iiint_{\Omega} ([\nabla(\hat{v} + \alpha\eta) - \mathbf{Q}]^2 - [\nabla\hat{v} - \mathbf{Q}]^2) dV \\
 &= \lim_{\alpha \rightarrow 0} \frac{1}{\alpha} \iiint_{\Omega} [2 \langle (\nabla\hat{v} - \mathbf{Q}), \alpha\nabla\eta \rangle + \alpha^2(\nabla\eta)^2] dV \\
 &= 2 \iiint_{\Omega} \langle (\nabla\hat{v} - \mathbf{Q}), \nabla\eta \rangle dV \\
 &= 2 \iiint_{\Omega} \eta \langle \nabla, (\nabla\hat{v} - \mathbf{Q}) \rangle dV - 2 \iint_{\partial\Omega} \eta \langle (\nabla\hat{v} - \mathbf{Q}), \mathbf{n} \rangle dS. \quad (\text{A.6})
 \end{aligned}$$

Since η lies the set \mathcal{T} , the last surface integral vanishes and the condition that \hat{v} has to satisfy in order to minimize the functional \mathcal{F} corresponds to:

$$\forall \eta \in \mathcal{T}, \iiint_{\Omega} \eta \langle \nabla, (\nabla\hat{v} - \mathbf{Q}) \rangle dV = 0. \quad (\text{A.7})$$

Since the set \mathcal{T} is dense in \mathcal{H} , the function \hat{v} must satisfy the following condition to minimize the functional \mathcal{F} :

$$\langle \nabla, (\nabla\hat{v} - \mathbf{Q}) \rangle = 0. \quad (\text{A.8})$$

Curriculum Vitae

Geboren am 23. Juni 1972 in Besançon, Frankreich

1990: Naturwissenschaftliches Abitur in Poitiers, Frankreich. Note: „Gut“.

1990–1992: Besuch der Vorbereitungsklassen zu den Grandes Ecoles in Poitiers, Frankreich.

1992–1995: Studium an der Ingenieurhochschule ENSMA (Nationale Hochschule für Mechanik und Luftfahrttechnik). Maschinenbaustudium mit den Fachrichtungen Allgemeine Mechanik, Wärmelehre, Strömungsmechanik und Gasdynamik. Abschluß als Diplom-Ingenieur.

1995–1996: Aufbaustudium an der Ecole Centrale de Nantes (ECN). Vorbereitung des DEA-Diploms für die Zulassung zur Promotion an der ECN. Fachrichtung Turbulenzmodellierung und theoretische Schiffshydrodynamik. Abschluss als Diplom-Ingenieur (Note: „sehr gut“) und Erhaltung des DEA-Diploms (Note: „sehr gut“). Bester Student des Jahrgangs.

1996–1997: Assistent an der Militärakademie der Französischen Marine (Ecole Navale) im Rahmen des Militärdienstes.

1997–1998: DAAD-Stipendiat. Durchführung eines Forschungsvorhaben zur Entwicklung von Festigkeitsmodellen mit der Methode der Finiten-Volumina unter der Leitung von Prof. Perić.

1998–2002: Wissenschaftlicher Mitarbeiter am Arbeitsbereich Fluidodynamik und Schiffstheorie der Technischen Universität Hamburg-Harburg. Durchführung von Projektarbeiten mit der Thematik Simulation von Zweiphasenströmungen mit freier Oberfläche und Oberflächenspannungseffekten im Rahmen des DFG-Forschungsschwerpunktes „Fluidzerstäubung und Sprühvorgänge“.

2002–2004: Angestellter der Firma CD adapco. Arbeitsverhältnis als Support-Ingenieur für die von der Firma vertriebene Software, u.a. die Strömungssimulationpakete *comet* und STAR-CD.

2004–2005: Angestellter des America's Cup Syndikats BMW Oracle. Arbeitsverhältnis als Berechnungs- und Simulationsingenieur.